TRACING GALAXY ASSEMBLY: A STUDY OF MERGING AND EMISSION–LINE GALAXIES

by

Amber N. Straughn

A Dissertation Presented in Partial Fulfillment
of the Requirements for the Degree
Doctor of Philosophy

ARIZONA STATE UNIVERSITY

August 2008

TRACING GALAXY ASSEMBLY: A STUDY OF MERGING AND

EMISSION–LINE GALAXIES

by

Amber N. Straughn

has been approved

July 2008

Graduate Supervisory Committee:

Rogier A. Windhorst, Chair
Sangeeta Malhotra
James Rhoads
Rolf A. Jansen
Richard Lebed

ACCEPTED BY THE GRADUATE COLLEGE

TRACING GALAXY ASSEMBLY: A STUDY OF MERGING AND

EMISSION–LINE GALAXIES

by

Amber N. Straughn

has been approved

July 2008

APPROVED:

_____, Chair

_____

_____

_____

_____

Supervisory Committee

ACCEPTED:

_____

Department Chair

_____

Dean, Graduate College

ABSTRACT

One astrophysical problem that remains largely unsolved is that of galaxy formation and evolution. These outstanding questions can be probed through investigation of galaxy mergers and physical processes induced by merging events. The Hubble Space Telescope (HST) has revolutionized our view of the universe since the early 1990's, and deep imaging over the past decade has allowed a much more detailed view of galaxies that existed when the universe was only a fraction of its current age. Through a study of early–stage mergers ("tadpole" galaxies), observational support is found for recent numerical simulations which predict that Active Galactic Nuclei (AGN) activity will only be detectable well after the galaxies are in a morphologically–recognizable merger stage. Additionally, the percentage of galaxies that appear in the tadpole phase is roughly constant at $\sim$6% for the redshift range probed here, implying that galaxy assembly generally kept up with the supply of available field galaxies over cosmic time. Merging is known to induce episodes of active star formation, which can be probed through spectral emission lines. The HST Probing Evolution And Reionization Spectroscopically (PEARS) grism survey data is used to investigate emission–line galaxies (ELGs) in the widely–studied CDF-S field. Three ELG detection methods are investigated in detail; a 2–dimensional method is efficient at detecting individual star–forming galaxy knots out to redshifts $\sim$1.5. Many of the emission lines detected have very high equivalent widths (EW), and potential evolution of [O II] EW with redshift is detected—suggesting substantial evolution of galaxies' star–forming properties since redshift$\sim$1.5. The total sample includes 230

star–forming knots in 203 individual ELGs. One hundred eighteen of these galaxies previously had no spectroscopic redshift; the line identifications now provide secure grism–spectroscopic redshifts for these objects. By adjusting the fitting procedure to include the H–beta line (which is blended with [O III]), estimates of excitation are obtained and thus AGN candidates are selected. Additionally, the radial distribution of giant star–forming knots in PEARS galaxies up to redshift $\sim$0.5 tend to peak near the half–light radii—similar to that of giant HII regions in local galaxies.

To Matt, my husband and best friend, who has been a constant and patient supporter and encourager.

ACKNOWLEDGMENTS

It is with a spirit of sincere gratitude that I wish to acknowledge here people who have been instrumental in the completion of this dissertation.

I would like to thank first my advisor, Rogier Windhorst, for his ongoing guidance, patience, and support the past six years. His genuine concern and tireless dedication to his graduate students is truly appreciated. I would like to thank Rogier especially for the effort he has made at introducing and promoting my research at meetings and talks around the country (and world) and for introducing me to many people along the way who have helped me with my work and helped to open doors for future career opportunities. Dissertations do not get completed without the help of an excellent advisor, and Rogier is one.

I also thank the rest of my graduate committee: Sangeeta Malhotra, James Rhoads, Rolf Jansen, and Rich Lebed, for their support and supervision of this work. Addditionally I would like to thank my NASA Jenkins Mentor, Jon Gardner, for his guidance especially during my summer internships at Goddard Space Flight Center. I have had the privalege to meet and work with many other astronomers during my graduate studies; in particular I want to acknowledge Gerhardt Meurer and Nor Pirzkal for their assistance with major components of this dissertation.

The general support and friendship of the cosmology student group at ASU has been extremely important to me throughout the course of this work. In particular, I am endebted to Seth Cohen for his friendship, humor, and ceaseless help and advice on programming and research in general. Even in the midst of seemingly endless code-

debugging, Seth could always make me laugh, and for that I am grateful. Thanks to Nimish Hathi, who always seemed to be the most calm and organized person in our group, and who always had answers to any questions I could think up. Other students in our group who I would like to acknowledge for their friendship, in no particular order, are Russell Ryan, Hwiyun Kim, Kazuyuki Tamura, Steve Finkelstein, and Katie Kaleida. Additionally I would like to thank Allison Loll and Keely Snider; these two girls have been wonderful friends since our first day at graduate school.

I have received financial support from a number of sources the past six years. In particular, I want to acknowledge the Graduate Assistance in Areas of National Need (GAANN) Fellowship, ASU's Department of Physics Teaching Assistantships and the Wally Stoelzel Physics Scholarship, the NASA Space Grant Fellowship, and especially the NASA/UNCFSP Harriett G. Jenkins Predoctoral Fellowship. The Jenkins program has provided me with three years of financial support and invaluable opportunities to network with other scientists across the country.

Long before graduate school even began, my family began cheering me on in my pursuits of the stars. My mom, Carolyn (Holley) Wetherelt, has always believed in my dreams and has been a constant, loving supporter of all my endeavors, and for that I thank her with my whole heart. My dad, Donald Holley (1946-1997), taught me by example the importance of hard work. I thank my siblings Shane and Ashley. Most of all, I thank my husband, Matt. Your constant encouragement, patience, support and love have quite literally sustained me through this process. Matt, I thank you and love you with all that I am. Isaiah 26:12

TABLE OF CONTENTS

Page

Page

Page

LIST OF TABLES

LIST OF FIGURES

Figure Page

1. INTRODUCTION

1.1. The process of Hierarchical Galaxy Formation

One astrophysical problem that remains largely unsolved to this day is that of galaxy formation and evolution. In the nearby universe, we observe galaxies that are neatly classified in the familiar Hubble types, yet as we look into the higher redshift universe—particularly at $\gtrsim$1–2—we observe a much more peculiar universe filled with numerous irregularly–shaped galaxies that do not resemble many of the large, organized ones seen nearby (Driver et al. 1998, Glazebrook et al. 1995).

Similarly, the process of supermassive black hole formation is currently not well understood. WMAP results suggest that massive Population III stars existed at z$\sim$20 with masses $\sim$200–300 $M_\odot$ which likely resulted in black holes with masses $\sim$100–150 $M_\odot$ (Fryer, Woosely, & Heger 2001; Madau & Rees 2001). We observe supermassive black holes in nearby galaxies with masses of $\sim 10^9$ $M_\odot$ (Kormendy & Richstone 1995; Kormendy & Gebhardt 2001). It is crucial to understand how this transition from $\sim$150 $M_\odot$ black holes at z$\sim$20 to $\sim 10^9$ $M_\odot$ at z$\sim$0 occurred. One well-supported theory is that the process by which this transition takes place is through hierarchical galaxy merging and the subsequent merging and feeding of the central supermassive black holes, which are observable as AGN in certain phases.

This process of galaxy merging triggers several specific physical processes, including not only supermassive black hole growth, but also enhanced star formation (e.g. Larson & Tinsley 1978; Kennicutt et al. 1987; Hopkins et al. 2005; Li et al. 2008; see reviews by Keel 1991 and Struck 1999). Investigating galaxies' star formation activity is thus important in understanding the consequences of galaxy interactions.

An efficient way to probe galaxies that are actively forming stars is through investigation of their spectral emission lines. These emission-line galaxies (ELGs) yield insight into the mechanism by which galaxies are believed to have built up over cosmic time. Since ELGs by definition have strong emission in lines, they provide a straight–forward way to detect faint actively star-forming galaxies in the intermediate– to high–redshift universe.

1.2. Surveys of Hierarchical Galaxy Assembly

Any investigation that focuses on studying the evolution of galaxies' physical properties over time of course requires a sample of galaxies that spans many billions of years of lookback time—and thus great distance. More distant objects appear fainter—due not only to the inverse–square law, but also to cosmological surface–brightness dimming and the K–correction. Because of this, many optical surveys over the past ten to fifteen years have focused on deep imaging in order to find fainter objects which are common at higher redshifts. The Hubble Deep Fields (HDF; Williams et al. 1996), the Great Observatories Origins Deep Survey (GOODS; Giavalisco et al. 2004), the Cosmological Evolution Survey (COSMOS; Scoville et al. 2007) have been instrumental in broadening our view of the universe via faint optical imaging. The Hubble Ultra Deep Field (HUDF; Beckwith et al. 2006) is the deepest optical image as of this writing, and has provided a wealth of objects for these studies. In addition to imaging, spectroscopic surveys have also greatly added to our knowledge of both nearby and distant galaxies. The Sloan Digital Sky Survey (SDSS; Stoughton et al. 2002 and later releases), the Kitt Peak National Observera-

tory International Spectrscopic Survey (KISS; Salzer et al. 2000), the Canada–France Redshift Survey (CFRS; Lilly et al. 1995, Hammer et al. 1997), and the DEEP1 and DEEP2 projects (Davis et al. 2003) are examples of such surveys. Space-based grism spectroscopy has also been used in the study of distant galaxies through projects such as the STIS Parallel Survey (Gardner et al. 1998; Teplitz et al. 2003), the NICMOS Grism Parallel Survey (McCarthy et al. 1999; Yan et al. 1999), the ACS Grism Parallel Survey (Drozdovsky et al. 2005), the GRism ACS Program for Extragalactic Science (GRAPES; Pirzkal et al. 2004, Malhotra et al. 2005), and the Probing Evolution And Reionization Spectrscopically project (PEARS; Malhotra et al. 2008, in preparation; Straughn et al. 2008). Surveys such as these are optimal starting points for studies of merging and emission–line galaxies. The following two sections outline brief histories of these objects and our study of them in this dissertation.

1.3. Mergers as Tracers of Galaxy Assembly

In order to trace the formation history of the universe, we must discover the mechanism by which galaxies transition from the small, clumpy irregular galaxies that appear to be dominant at high–redshift (Driver et al. 1998; Glazebrook et al. 1995) to the large, structured ones common in the present–day, nearby universe. A casual look at the numerous high–redshift objects (as well as some nearby) suggests that they have been disturbed in some way. Early speculations about irregular and/or peculiar galaxies included the idea that galaxy collisions or mergers could be the cause of these peculiar morphologies (e.g., Holmberg 1941, Baade & Minkowski 1954). The pioneering numerical simulations of Toomre & Toomre (1972) set the stage for

decades of detailed comparison between observation and theory, and for studies of galaxy interactions in general. These ideas have evolved into the theory of hierarchical galaxy assembly that is widely accepted in the astronomical community today.

The general hierarchical scenario goes as follows. Within the cold dark matter (CDM) paradigm, small CDM overdensities collapse first, producing dark matter "halos" and causing the associated (baryonic) gas to collapse as well (White & Rees 1978; Navarro et al. 1997). The resulting collapsed gas forms stars, and the first spheroids in the universe. This collapse of small (i.e. ∼galaxy– and sub–galaxy size) CDM overdensities occurs before large (cluster–size) ones, and thus provides a "bottom-up" picture of structure formation in the universe. Gas settles onto these first galaxies in disks, and mergers occur between the galaxies. Depending on many factors such as mass ratio, gas content, rotation dynamics, and feedback mechanisms, major mergers between disk galaxies may result in disorganized structures, and eventually relax into elliptical galaxies. Numerical simulations generally support this hierarchical scenario of forming ellipticals via major mergers of disk galaxies (Hernquist 1993, Bender 1996, di Matteo et al. 2005, Springel et al. 2005a, 2005b; Hopkins et al. 2006, Hopkins et al. 2008).

Though the overall picture seems simple enough, the details of hierarchical galaxy assembly are still not completely understood. This is due in part to the computational difficulty in modeling multiple and diverse merger scenarios, as well as reconciling results to (often seemingly contradictory) observational findings. Much effort has gone into modeling the numerous physical processes that are thought to

occur in galaxy mergers, as well as the vast array of initial dynamical conditions that exist in nature. In a recent study di Matteo et al. (2007) present a suite of numerical simulations of major galaxy interactions, including variations of galaxy morphological type, bulge–to–disk ratios, gas mass fractions, and orbital orientation (direct vs. retrograde) in order to investigate star formation efficiency in a wide range of scenarios. Earlier studies performed similar simulations (Mihos et al. 1992; Mihos & Hernquist 1996; see also the review by Barnes & Hernquist 1992) and many studies have also taken into account the effect of minor mergers on galaxies' properties (Mihos & Hernquist 1994; Hernquist & Mihos 1995; Okamoto & Nagashima 2004; Bournaud et al. 2007). While details among these various studies differ, the general consensus remains that galaxy interaction causes some degree of enhanced star formation and can result in the destruction of galaxy disks and thus formation of spheroids.

Connecting theory to observation is a crucial step. Currently, many observations support the hierarchical scenario, in that galaxies are often observed to be in a dynamically disturbed state—indicative of a recent interaction. The prevalence of peculiar galaxies is particularly striking at higher redshift. Additionally, the largest, most luminous galaxies in the universe are cD galaxies (Matthews et al. 1964; Leir & Van den Bergh 1982; review by Tonry 1987). These galaxies reside in the centers of galaxy clusters and are observed to have extensive stellar envelopes and multiple cores, suggestive of formation through merging (Jordan et al. 2004; Bender 1996). Despite the observational evidence for a hierarchical description of galaxy evolution, one major puzzle remains: the presence of large ellipticals already in place at high

redshift (Glazebrook et al. 2004; Treu et al. 2005; however, see Bower et al. 2006). These is clearly still much to be learned in our understanding of galaxy evolution, and observational studies that focus on galaxies that are in this transitional phase are crucial to enhance our understanding on this topic. Such investigations have relied mainly on two methods of identifying merging galaxies: pair studies and morphological studies. The former detects two pre-merger stage galaxies that are some defined spatial distance apart on the image, and the latter relies on morphological signatures of galaxy interactions such as asymmetries and tidal tails. While each method has its advantages and pitfalls, both provide some degree of insight into the complicated problem of galaxy assembly.

1.4. Tadpole Galaxies as Tracers of Galaxy Assembly

Since astronomical observations only catch a snapshot of any one galaxy at one particular stage in its evolutionary history, statistical studies of large samples of galaxies—and thus a large overall timeframe—are required to gain insights into the overall evolutionary processes. In particular, deep imaging is necessary to probe the faintest galaxies at high redshift. The release of the HUDF in early 2004 was eagerly anticipated by those who study galaxy formation and evolution. It has motivated many new projects exploiting the unprecedented depth to which this field reaches. One particular phenomenon evident in the HUDF is the abundance of galaxies that appear to be dynamically unrelaxed. These galaxies present morphologies characterized by a bright unresolved knot, plus an extended, dimmer "tail" to one side, reminiscent of tadpoles. In particular, their morphologies suggest that they are merging

systems described above. Thus the tadpole galaxies allow us to view a crucial early time in galaxy evolution—this very process by which small, irregular galaxies build up into large, dynamically relaxed ones. In Chapter 2 of this dissertation we investigate this "tadpole" or early–stage merger phase of galaxy assembly, detailing the sample selection method and discussing the redshift distribution and the relation to active galactic nuclei (AGN). We demonstrate how our observations fall in line with the numerical simulations discussed above.

1.5. ELGs: Clues to Active Star Formation Across Cosmic Time

Galaxies that are actively forming stars have long been regarded as important probes to galaxy evolution. Episodes of extreme star formation in galaxies are clues that the galaxy is undergoing some type of event that is causing the physical change of gas to stellar mass. Many times the event is an interaction, in which galaxies' gas is funnelled to the nuclear region where gravitational instabilities cause rapid formation of new stars. During interactions and mergers, the dynamics of the event can also cause bursts of star formation in tidal tails and bridges (Hibbard et al. 2005; Knierman et al. 2003; Smith et al. 1997)—giving rise to a whole array of disturbed morphological types such as chains, clump-clusters, and tadpoles as described above (Cowie et al. 1995 & 1996; Conselice et al. 2004; Elmegreen et al. 2004a; van den Bergh 2002; Straughn et al. 2006). Much physical information can be attained about the specifics of the star formation in galaxies through study of their spectra.

Space–based grism spectroscopy is an efficient method by which to gain spectra of many faint objects at once. Fields that already have deep broadband imaging—

such as the HUDF and GOODS fields described above—are often targets of such grism surveys. The HST PEARS project provides low-resolution slitless spectra of ∼13,000 galaxies in the GOODS North and South fields (Ryan et al. 2007; Cohen et al. 2008 in preparation). One important subset of objects in these data are ELGs that are actively forming stars, many of which display disturbed morphologies indicative of merging activity. Early investigations have highlighted the importance of starbursts in interacting galaxies in general (Larson & Tinsley 1978), and subsequent studies have made use of emission-line fluxes to estimate star-formation rates (SFRs; Kennicutt 1998). In particular, Hα emission has been used to derive SFRs and those results have been interpreted in the overall framework of galaxy evolution (Kennicutt 1983). Several studies have highlighted the importance of constraining the current SFR-density in the local universe using ELGs (Gallego et al. 1995, 2002; Lilly et al. 1995), while others have investigated the evolution of the SFR with redshift (Madau et al. 1998; Cowie et al. 1999). In the context of hierarchical merging, active star formation has long been regarded as a strong indicator of merging activity, and the more recent studies mentioned above (di Matteo et al. 2005, Hopkins et al. 2005, Straughn et al. 2006, Cohen et al. 2006) have emphasized the evolutionary importance of merging galaxies and their role in AGN growth over cosmic time. Prior to PEARS, slitless spectroscopy has been used often over the past several years to detect ELGs. In particular, HST's NICMOS and STIS instruments have produced several surveys in which ELGs have been utilized to estimate the Hα line luminosity functions and SFRs (e.g., Yan et al. 1999; HST NICMOS with the G141 grism),

as well as the [O II] luminosity function and star formation densities at intermediate redshifts (e.g., Teplitz et al. 2003; HST STIS with the G750L grism). In Chapter 3 of this dissertation we describe a new 2D detection method designed to systematically select ELGs from the PEARS grism data, and Chapter 4 expands the study to include more fields, a catalog of new grism redshifts for the GOODS South Field, and an investigation of the individual star-forming regions in intermediate redshift galaxies that is enabled by our unique detection method.

1.7. Outline of This Dissertation

The outline of this dissertation is as follows. Chapter 2 describes the tadpole galaxies and has been published as Straughn et al. 2006, ApJ, 639, 724 (© and published by the American Astronomical Society in the March 2006 issue of the Astrophysical Journal). Chapter 3 details the 2D detection method of ELGs in the PEARS HUDF grism data and has been published as Straughn et al. 2008, AJ, 135, 1624 ((© and published by the American Astronomical Society in the April 2008 issue of the Astronomical Journal). Chapter 4 extends the ELGs study to four more ACS fields and will be submitted to the Astronomical Journal, and will appear as Straughn et al. 2008 (© and to be published by the American Astronomical Society in the Astronomical Journal). Chapter 5 summarizes the results of this study and briefly outlines future work on the subject.

2. TADPOLE GALAXIES IN THE HUBBLE ULTRA DEEP FIELD

In the Hubble Ultra Deep Field (HUDF) an abundance of galaxies is seen with a knot at one end plus an extended tail, resembling a tadpole. These "tadpole galaxies" appear dynamically unrelaxed — presumably in an early merging stage — where tidal interactions likely created the distorted knot-plus-tail morphology. Here we systematically select tadpole galaxies from the HUDF and study their properties as a function of their photometric redshifts. In a companion HUDF variability study presented in this issue, Cohen et al. (2005) revealed a total of 45 variable objects believed to be Active Galactic Nuclei (AGN). Here we show that this faint AGN sample has no overlap with the tadpole galaxy sample, as predicted by recent theoretical work. The tadpole morphology — combined with the lack of overlap with the variable objects — supports the idea that these galaxies are in the process of an early-stage merger event, i.e., at a stage that likely precedes the "turn-on" of any AGN component and the onset of any point-source variability. We show that the redshift distribution of tadpole galaxies follows that of the general field galaxy population, indicating that — if most of the tadpole galaxies are indeed dynamically young — the process of galaxy assembly generally kept up with the reservoir of available field galaxies as a function of cosmic epoch. These new observational results highlight the importance of merger-driven processes throughout cosmic history, and are consistent with a variety of theoretical and numerical predictions.

2.1. Introduction: Tadpole Galaxies in the HUDF

The origin of disk galaxies has long been thought to occur through the process of dissipational collapse in a Cold Dark Matter (CDM) universe (White & Rees, 1978). Within this paradigm, hierarchical clustering (Navarro, Frenk, & White 1997) produces dark matter halos in which dissipational collapse of the residual gas oc-

curs. The resulting disks retain the kinematic information of their host dark matter potential wells (Blumenthal et al. 1986). Recent numerical simulations have resolved some long-standing discrepancies in the standard dissipational collapse scenario by including previously-neglected energetic feedback from central supermassive black holes during galaxy merging events (e.g. Robertson et al. 2005). In particular, they emphasize the relationship between the central black hole mass and the stellar velocity dispersion, which confirms the link between the growth of black holes and their host galaxies (di Matteo, Springel, & Hernquist 2005; Springel, di Matteo, & Hernquist 2005ab). These theoretical predictions place merger-driven scenarios on the forefront, suggesting that galaxy merger activity is a crucial element in a cosmological description of the Universe. The present study provides observational support for many of these theoretical predictions.

A large abundance of galaxies in the Hubble Ultra Deep Field (HUDF; Beckwith et al. 2005) appear dynamically unrelaxed, which suggests they must play an important role in the overall picture of galaxy evolution. In particular, we notice many galaxies with a knot-plus-tail morphology. This particular morphology constitutes a large, well-defined subset of the irregular and peculiar objects in the HUDF that is uniquely measurable as described in Section 3. The selection of this specific morphology also ties closely to the numerical simulations described above (di Matteo, Springel, & Hernquist 2005; Springel, di Matteo, & Hernquist 2005ab), which predict a stage of merger-driven galaxy evolution that closely resembles these tadpole galaxies in a distinct phase that does not yet show AGN activity (as discussed fur-

ther in Section 7). In particular, this morphology appears to represent an *early* stage in the merging of 2 nearly-equal mass galaxies. We systematically selected galaxies displaying this knot-plus-tail morphology from the HUDF; a representative sample of tadpoles is shown in Fig. 1 (details of sample selection are given in Section 3). All the selected tadpole galaxies contain the asymmetric, pointlike source with a diffuse tail morphology, some with multiple knots; all of which we believe are undergoing recent interactions. They are mostly linear structures, some resembling the "chain" galaxies first reported by Cowie, Hu, & Songaila (1995). When more than two clumps come together, these objects may be more akin to the luminous diffuse objects and clump clusters (Conselice et al. 2004; Elmegreen, Elmegreen, & Sheets 2004; Elemegreen, Elmegreen, & Hirst 2004), or other types of irregular objects (van den Bergh 2002). Elmegreen et al. (2005) visually classify 97 HUDF galaxies (down to 10 pixels in size) as "tadpoles" and 126 as "double-clump." Some of the galaxies classified by Elmegreen et al. as "double-clump" were identified as tadpoles by our code, due either to the unresolved nature of one clump (which would have been detected as a "tail" in our analysis) or to the diffuse nature of one end of the object. Since our goal in selecting these tadpoles was to sample galaxies that had *recently* undergone interaction, inclusion of some of these "double-clumps" is warranted. One high redshift object in our sample has been studied in detail by Rhoads et al. (2005). A few objects with multiple knots are detected by our selection software, but the majority have a single prominant knot with an extended tail.

In this paper, we present the photometric redshift distribution of tadpole galaxies, and compare it with the redshift distribution of the general field galaxy population. This paper is organized as follows. In §2, we describe the HUDF data, and in §3 the tadpole sample selection. In §4, we discuss why the majority of tadpole galaxies are likely *not* chance alignments, but instead mostly dynamically young objects. In §5, we discuss their redshift distribution, in §6 their relation to galaxy assembly, and in §7 their possible relation to AGN growth.

2.2. Hubble Ultra Deep Field Data

The Hubble Ultra Deep Field is a 400 orbit survey in four filters carried out using the Advanced Camera for Surveys (ACS) aboard the *Hubble Space Telescope* (*HST*) of a single field centered on RA(J2000)=$03^{\rm h}32^{\rm m}39\overset{\rm s}{.}0$, Dec(J2000)=$-27^\circ47'29\overset{''}{.}1$. The 144-orbit F775W ($i'$) image is deepest, followed by F850LP (z'; 144 orbits), F606W (V; 56 orbits), and F435W (B; 56 orbits). The HUDF reaches $\sim$1.0 mag deeper in B and V and $\sim$1.5 mag deeper in i' than the equivalent filters in the Hubble Deep Field (Williams et al. 1996). From the $\sim$10,000 objects detected in the HUDF (Koekemoer 2004), we will select the sample of tadpole galaxies and analyze their properties using the i'-band image, because it provides the highest sensitivity of the four filters. Yan & Windhorst (2004b) discuss how this results in a bias against objects at $z \gtrsim 5.5$. This bias is small, and only concerns the high redshift tail of the redshift distribution. Note, however, that tadpole galaxies at $z \simeq 5.5$ *do* exist (e.g., Rhoads et al. 2005).

2.3. Tadpole Sample Selection

The first step in this analysis is to systematically select the galaxies that have the characteristic tadpole shape. We selected sources in the F775W (i') band to $i'_{AB} = 28.0$ mag using `SExtractor` (Bertin & Arnouts 1996). The objects of interest all have a bright "knot" at one end with an extended "tail" at the other. `SExtractor` selects objects from an image based on different input parameters, and adjusting them results in the desired selection of sources. The crucial parameter at this stage is DEBLEND_MINCONT, which governs the manner in which nearby peaks in flux are considered part of a single object and thus are counted as one source. With the deblending parameter set to a high value, `SExtractor` will separate nearby flux maxima into separate sources. In contrast, when the deblending is set to a low value, the program will count the nearby maxima largely as one source. Two different source catalogs are thus generated: the highly deblended catalog will contain many point-like sources, including the knots of potential tadpole galaxies. The catalog with low-deblending will contain extended sources, including the tadpole galaxies' tails. The catalogs contain many more sources than the desired ones, and the correctly shaped objects must be selected from these two initial catalogs. The desired tadpole galaxies have a nearly unresolved knot or concentration, and an extended tail, so these types of sources must be selected from the initial catalog, and related spatially such that they represent real objects. All of the following procedures were performed using IDL.

Both input `SExtractor` catalogs, described above, contain the following information about the selected sources: x and y pixel locations, length of the semi-major

and semi-minor axis (a and b) of `SExtractor` ellipses, and the angle (θ) of the semi-major axis from north through east. The following input parameters were calibrated using a training set of tadpole galaxies that were manually selected by visual inspection of portions of the HUDF. First, the knots of the tadpole galaxies were selected by setting an axis-ratio limit. A "knot" was defined to be a source from the highly deblended catalog with an axis ratio greater (i.e., rounder) than some critical value (in our case, $b/a > 0.70$). In the same way, the "tails" needed to be elongated objects, so a similar procedure was performed on the objects from the catalog with low-deblending, but with the criterion that their $b/a < 0.43$. The two new lists of correctly shaped objects had to be related physically on the image, thus, a new set of objects was defined where a knot was within a certain distance of the geometrical center of a tail. This distance was taken to be $< 4a$ (in semi-major axis units of the tail). We also required that the knot be at least $> 0.1a$ from the tail's geometrical center, since we are searching for asymmetric objects, and want to eliminate upfront as many of the true edge-on mid-type spiral disks as possible. The objects also must have the knot near one end of the tail, and this was accomplished by selecting only those tails and knots that had a relative angle θ — measured with respect to the semi-major axis of the tail — that was $\leq 20°$. This step prevented including knots and tails that were close together on the image, but not physically part of the same galaxy.

These selection criteria provided a list of the tadpole-shaped galaxies. The final number of tadpoles selected depended on the selection program's input parameters

for the limiting axis-ratios, the distance at which the knots and tails were considered related, and the angle difference between the knot and the semi-major axis of the tail. The values of these parameters are given in Table 1. With these values, the tadpole galaxy selection program detected 154 sources total. This sample was then refined as follows.

A large majority of the 154 tadpole galaxy candidates selected had the characteristic elongated knot-plus-tail morphology, although there were some anomalies. In total, 14 (9%) obvious mis-detections were visually rejected because they were very faint, on the edge of the image, or in the outskirts of large face-on spiral galaxies, where both knotty and diffuse regions are common and spatially close together. A visual examination of the field also produced 25 more tadpole galaxies not found by the selector program due to the inability of `SExtractor` to correctly separate particular point-like sources within these galaxies. These extra selected tadpole objects visually obeyed the morphological criteria that were used to define the main sample. Our total final sample thus contains 165 tadpole galaxies, a subset of which is shown in Fig. 1. In our final sample, less than 10% of the selected tadpoles appear as normal edge-on disk galaxies; the vast majority have the highly asymmetric morphology. In terms of visual vs. automatic selection, we find our sample to be about 91% (140/154) reliable and about 86% (154/179) complete. The final set of 165 tadpoles galaxies will now be studied as a separate class of dynamically unrelaxed objects and compared to the general field galaxy population in the HUDF.

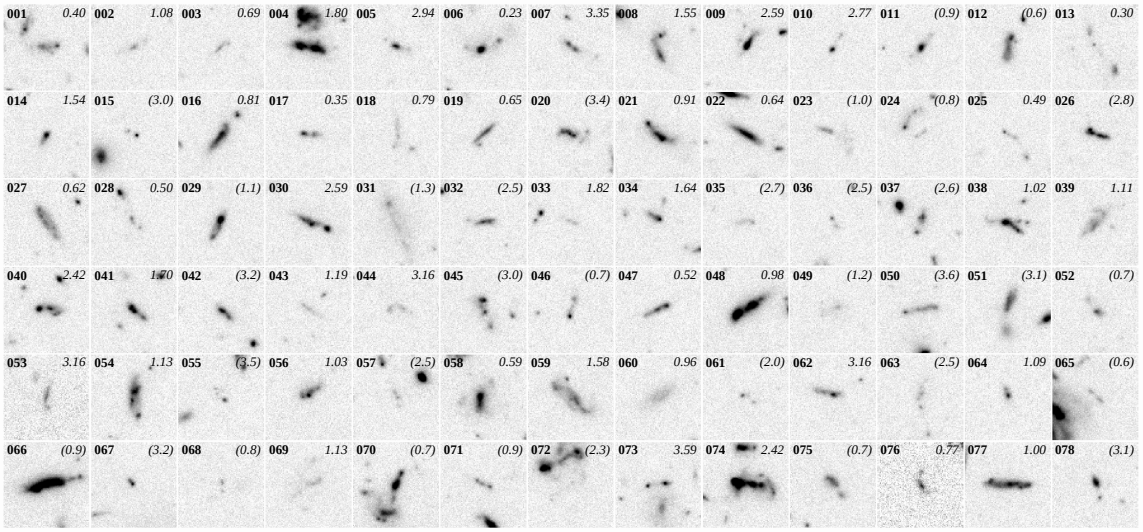

FIG. 1 F775W (i') band mosaic of a subset of the tadpole galaxy sample in the HUDF. Stamps retain the orientation of the HUDF; north is toward the top of the page and east is to the left. Index numbers are displayed in the upper-left corner of the stamps; photometric redshifts are given in upper-right corners. Parentheses indicate photometric redshifts with errors >1 based on HyperZ calculations. Stamps are 3 arcsec on a side. A table of coordinates for the entire tadpole sample is given in Section 3; the entire sample of 165 tadpoles appears in color in the online supplement. The vast majority of our tadpole sample contains the distinctive knot-plus-tail morphology, while sample contamination by normal (non-interacting) edge-on disk galaxies is less than 10%.

TABLE 1 Galaxy Selector Input Parameters

Parameter	Value
b/a limit: knots	>0.70
b/a limit: tails	<0.43
Distance to center (in a-axis units)	<4
Angle difference θ (tail-knot)	$\leq 20^{\circ}$
Total number of tadpoles automatically selected	154
DEBLEND_MINCONT (knots)	0.000005
DEBLEND_MINCONT (tails)	0.1

2.4. Why Tadpole Galaxies are Not Chance Alignments

In this section we demonstrate that these tadpole galaxies are likely not chance alignnments of tails and unrelated knots. We first select *all* elongated diffuse structures ("tails") in the HUDF, and then measure the angle θ of the nearest off-centered knot within a radius $r \leq 4a$ ($\leq 2''$). Chance alignments of unrelated tails and knots would show a random distribution of angles; however, Fig. 2 shows that there clearly is an excess of knots near $|\theta| \simeq 0^{\circ}$. The excess peak contains 154 knots, while the average number of knots with $|\theta| \geq 10^{\circ}$ is $\sim$15 per $5^{\circ}\theta$-bin. Figure 2 thus shows a significant overabundance of knots near the end of elongated diffuse structures as compared to randomly distributed knots. Hence, this physically meaningful result suggests that the majority of tadpole galaxies are not just chance alignments of unrelated knots. Instead, we believe they are mostly linear structures which are undergoing interactions. When compared to models of galaxy mergers (di Matteo, Springel, & Hernquist 2005; Springel, di Matteo, & Hernquist 2005; Robertson et al. 2005, Hopkins et al. 2005), these objects strongly resemble dynamically young objects in the

early stages of merging.

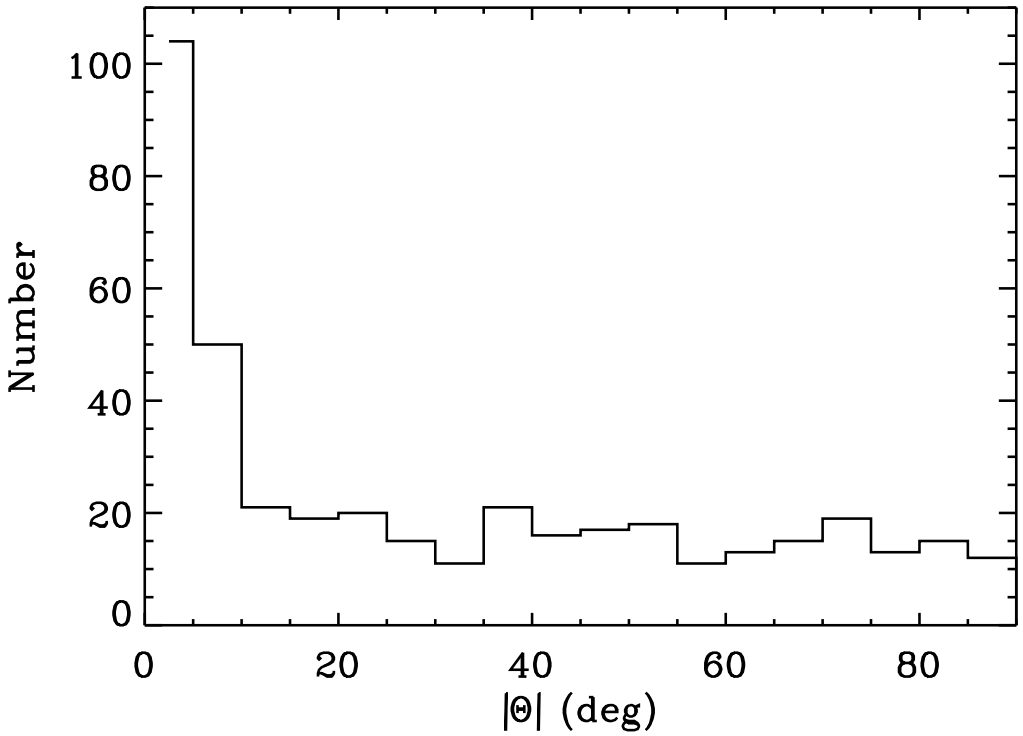

FIG. 2 Distribution of (the absolute value of) angles (θ) of all off-centered knots found within a radius $r \leq 4a$ ($\leq 2''$) from the center of each elongated diffuse structure in the HUDF, showing a clear excess of knots near $|\theta| \simeq 0°$.

2.5. The Redshift Distribution of Tadpole Galaxies

To investigate the occurrence of tadpole galaxies throughout the history of the universe, we calculate photometric redshifts of all HUDF galaxies to $i'_{AB} = 28.0$ mag. All photometric redshifts were calculated from the HUDF $BViz(+JH)$ photometry using HyperZ (Bolzonella et al. 2000). In order to investigate associated redshift errors, we compared our photometric redshifts to published spectroscopic redshifts for CDFS 70 objects. We find an rms scatter of 0.15 for the fractional photometric

redshift error δ=(photoz-specz)/(1+specz) if all 70 objects are included, and 0.10 when we reject a few of the most obvious outliers. This result is fully consistent with prior claims of photometric redshift accuracy in the literature (Lanzetta et al. 1997, Mobasher et al. 2004). The accuracy of our photometric redshift estimates depends on the accuracy of the measured magnitudes in each of the available filters. It also is largely independent of the shape of an object (although magnitude errors for more extended, lower surface brightness objects tend to be somewhat larger than those for more concentrated, higher surface brightness objects of the same total magnitude).

The redshift distribution of all galaxies in the HUDF (solid line in Fig. 3) is as expected, with the primary peak at $0.5 \leq z \leq 1.0$ and a generally declining tail at $z \simeq 4$–5. These trends were also seen in the general HDF redshift distribution of faint field galaxies (Driver et al. 1998). Also apparent is a lack of objects at $z \simeq 1$–2 due to unavailable UV spectral features crossing the $BViz(+JH)$ filters. This occurs because the HUDF does not have deep enough F300W or U-band (ultra-violet) data, unlike the situation in the HDF (Williams et al. 1996). This redshift bias, however, is the *same* for both the tadpole and the general field galaxy populations. In Fig. 3, the tadpole galaxy distribution is multiplied by a factor of 16 for best comparison with that of the field galaxies. Within the available statistics, the redshift distribution shape of the tadpole galaxies follows that of the general field galaxies quite closely. This suggests that if tadpole galaxies are indeed dynamically young objects related to early-stage mergers, they may occur in the same proportion to the field galaxy population at all redshifts. Tadpole galaxies may therefore be good tracers of the galaxy assembly

process. The ratio of the two redshift distributions N(z) was calculated as well, and the resulting percentage of tadpole galaxies is plotted in Fig. 4 as a function of redshift together with the statistical errors. Overall, the percentage of tadpole galaxies is roughly constant at ∼6% with redshift to within the statistical errors for the redshift range probed in our study ($0.1 \leq z \leq 4.5$).

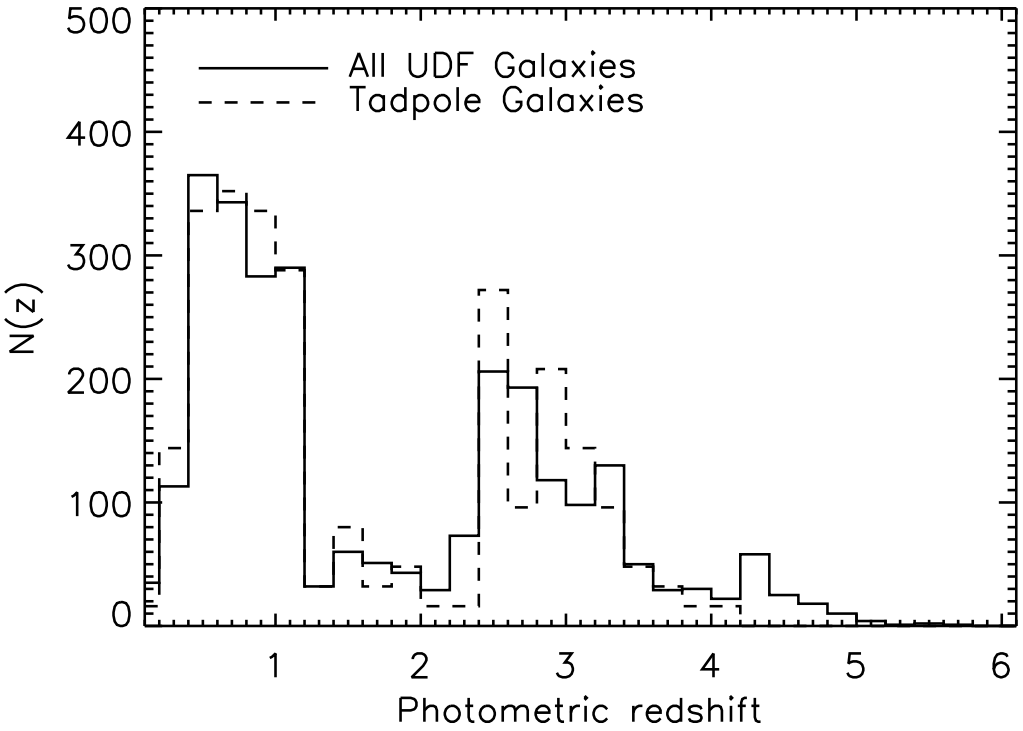

FIG. 3 Photometric redshift distribution of galaxies in the HUDF. The solid black histogram shows the redshift distribution of all HUDF field galaxies to $i'_{AB} = 28.0$, while the dashed histogram shows the redshift distribution of the tadpole galaxies. The latter was multiplied by 16× for best comparison of its shape with the redshift distribution of the field galaxies.

TABLE 2: Global Properties of Tadpole Galaxies

ID	RA J2000	DEC J2000	i'_{AB} mag[a]	Photometric redshift
1	03:32:30.118	-27:47:17.61	24.86	0.40
2	03:32:30.162	-27:47:36.22	27.28	1.08
3	03:32:30.266	-27:47:50.45	27.45	0.69
4	03:32:30.674	-27:47:42.30	24.14	1.80
5	03:32:30.995	-27:48:03.88	26.38	2.94
6	03:32:31.108	-27:47:58.64	25.01	0.23
7	03:32:31.190	-27:48:01.19	26.33	3.35
8	03:32:31.399	-27:47:13.45	25.35	1.55
9	03:32:31.530	-27:47:58.40	(25.5)	2.59
10	03:32:31.853	-27:47:42.06	26.78	2.77
11	03:32:31.883	-27:47:39.00	25.93	0.87
12	03:32:32.125	-27:47:27.94	25.29	0.62
13	03:32:32.218	-27:46:50.67	26.23	0.30
14	03:32:32.500	-27:47:02.00	(26.5)	1.54
15	03:32:32.601	-27:47:11.24	27.43	2.96
16	03:32:32.704	-27:48:14.77	24.85	0.81
17	03:32:32.739	-27:46:40.70	26.34	0.35
18	03:32:32.959	-27:47:02.08	27.12	0.79
19	03:32:33.004	-27:48:18.71	25.97	0.65
20	03:32:33.067	-27:47:43.96	25.50	3.37
21	03:32:33.086	-27:48:13.01	24.79	0.91
22	03:32:33.112	-27:48:23.05	24.82	0.64
23	03:32:33.212	-27:47:11.07	26.51	0.97
24	03:32:33.228	-27:47:25.27	27.97	0.82
25	03:32:33.541	-27:46:40.55	27.64	0.49
26	03:32:33.706	-27:47:56.64	25.49	2.77
27	03:32:33.911	-27:46:17.05	25.28	0.62
28	03:32:34.047	-27:46:42.73	26.39	0.50
29	03:32:34.180	-27:48:03.20	(25.7)	1.11
30	03:32:34.295	-27:46:47.67	25.05	2.59
31	03:32:34.438	-27:46:59.48	25.11	1.33
32	03:32:34.673	-27:47:25.27	26.16	2.51
33	03:32:34.704	-27:47:59.83	27.80	1.82
34	03:32:34.790	-27:47:24.30	(26.5)	1.64

Continued on next page...

TABLE 2 – Continued

ID	RA J2000	DEC J2000	i'_{AB} mag[a]	Photometric redshift
35	03:32:34.909	-27:48:06.77	27.53	2.74
36	03:32:34.981	-27:47:03.03	27.78	2.51
37	03:32:35.253	-27:47:14.14	26.00	2.58
38	03:32:35.260	-27:46:54.30	(25.7)	1.02
39	03:32:35.280	-27:48:57.25	25.84	1.11
40	03:32:35.353	-27:48:54.56	25.29	2.42
41	03:32:35.520	-27:47:53.80	(25.9)	1.70
42	03:32:35.670	-27:46:47.70	(26.2)	3.16
43	03:32:35.878	-27:49:01.58	27.48	1.19
44	03:32:35.881	-27:45:57.00	27.17	3.16
45	03:32:35.988	-27:47:25.53	25.38	2.96
46	03:32:36.169	-27:48:17.30	26.53	0.73
47	03:32:36.193	-27:46:08.88	25.89	0.52
48	03:32:36.267	-27:48:34.18	23.86	0.98
49	03:32:36.272	-27:47:09.55	27.13	1.19
50	03:32:36.290	-27:47:53.48	26.11	3.63
51	03:32:36.301	-27:47:22.40	25.19	3.10
52	03:32:36.462	-27:48:32.06	26.56	0.67
53	03:32:36.567	-27:49:17.54	26.35	3.16
54	03:32:36.613	-27:48:01.42	24.79	1.13
55	03:32:36.661	-27:48:03.11	27.28	3.54
56	03:32:36.680	-27:45:39.20	(26.0)	1.03
57	03:32:36.683	-27:47:38.53	27.25	2.51
58	03:32:36.860	-27:46:04.00	(26.0)	0.59
59	03:32:36.920	-27:46:34.79	24.85	1.58
60	03:32:37.138	-27:46:25.94	26.01	0.96
61	03:32:37.240	-27:48:54.80	27.43	2.03
62	03:32:37.340	-27:45:49.80	(26.5)	3.16
63	03:32:37.347	-27:47:39.45	26.89	2.51
64	03:32:37.350	-27:45:37.90	(26.7)	1.09
65	03:32:37.352	-27:48:38.22	26.92	0.61
66	03:32:37.409	-27:47:41.65	23.52	0.90
67	03:32:37.460	-27:47:23.30	(26.8)	3.18
68	03:32:37.546	-27:46:36.98	27.85	0.78
69	03:32:37.570	-27:49:11.50	26.38	1.13

Continued on next page...

TABLE 2 – Continued

ID	RA J2000	DEC J2000	i'_{AB} mag[a]	Photometric redshift
70	03:32:37.591	-27:47:39.49	24.22	0.67
71	03:32:37.735	-27:48:30.27	26.71	0.93
72	03:32:37.813	-27:47:57.34	26.85	2.29
73	03:32:37.832	-27:45:52.97	25.77	3.59
74	03:32:37.881	-27:48:53.11	23.59	2.42
75	03:32:37.949	-27:47:33.16	25.79	0.70
76	03:32:38.020	-27:45:09.30	26.13	0.77
77	03:32:38.096	-27:45:26.83	24.61	1.00
78	03:32:38.312	-27:47:28.11	26.05	3.14
79	03:32:38.376	-27:49:15.24	27.19	0.46
80	03:32:38.430	-27:46:34.80	(24.4)	2.58
81	03:32:38.541	-27:46:16.10	27.26	0.76
82	03:32:38.559	-27:47:30.25	24.66	2.96
83	03:32:38.608	-27:48:04.05	26.11	3.37
84	03:32:38.659	-27:49:18.86	23.78	0.61
85	03:32:38.816	-27:45:24.50	27.08	1.06
86	03:32:38.930	-27:48:56.80	(25.9)	2.81
87	03:32:39.194	-27:48:54.93	27.57	0.53
88	03:32:39.233	-27:48:49.83	25.53	2.94
89	03:32:39.325	-27:45:55.16	24.85	0.57
90	03:32:39.350	-27:45:55.40	(26.4)	0.57
91	03:32:39.404	-27:49:06.49	25.06	0.98
92	03:32:39.405	-27:46:22.41	25.69	3.28
93	03:32:39.485	-27:47:34.63	25.90	0.90
94	03:32:39.490	-27:49:23.24	26.32	0.50
95	03:32:39.530	-27:47:39.70	(25.9)	0.52
96	03:32:39.533	-27:49:31.24	25.69	0.72
97	03:32:39.540	-27:46:04.90	(26.3)	0.70
98	03:32:39.580	-27:49:12.83	25.44	1.07
99	03:32:39.600	-27:45:54.60	(24.3)	0.39
100	03:32:39.656	-27:45:29.97	25.29	0.35
101	03:32:39.723	-27:45:46.98	24.86	0.92
102	03:32:39.775	-27:46:18.16	27.65	3.86
103	03:32:39.829	-27:45:31.74	25.89	0.90
104	03:32:39.909	-27:46:56.06	27.81	2.88

Continued on next page...

TABLE 2 – Continued

ID	RA J2000	DEC J2000	i'_{AB} mag[a]	Photometric redshift
105	03:32:39.920	-27:48:58.90	(26.4)	0.90
106	03:32:40.200	-27:46:02.90	(26.1)	0.98
107	03:32:40.391	-27:48:29.47	25.18	2.59
108	03:32:40.562	-27:46:28.56	27.25	2.51
109	03:32:40.670	-27:46:41.49	26.48	2.51
110	03:32:40.761	-27:48:36.62	25.74	2.90
111	03:32:40.820	-27:49:04.40	(24.4)	0.98
112	03:32:40.920	-27:48:23.90	(25.2)	1.11
113	03:32:40.929	-27:46:33.76	26.90	1.17
114	03:32:41.000	-27:45:44.10	26.69	3.77
115	03:32:41.118	-27:47:34.59	24.17	0.73
116	03:32:41.126	-27:45:58.71	27.28	1.29
117	03:32:41.354	-27:48:49.53	26.04	0.32
118	03:32:41.374	-27:47:38.12	25.45	2.94
119	03:32:41.480	-27:46:42.40	(26.9)	1.19
120	03:32:41.487	-27:45:56.28	27.58	0.78
121	03:32:41.507	-27:46:53.52	27.59	0.60
122	03:32:41.560	-27:49:23.35	25.19	3.37
123	03:32:41.583	-27:46:39.94	24.86	0.86
124	03:32:41.595	-27:49:01.80	24.94	0.91
125	03:32:41.596	-27:48:49.85	26.55	0.39
126	03:32:41.598	-27:48:08.09	25.48	0.99
127	03:32:41.724	-27:46:56.50	26.53	1.19
128	03:32:41.762	-27:47:27.67	25.51	2.85
129	03:32:41.791	-27:47:38.69	26.28	2.41
130	03:32:41.805	-27:47:23.88	27.03	2.94
131	03:32:41.960	-27:45:48.82	26.94	3.59
132	03:32:42.476	-27:47:44.63	25.79	3.28
133	03:32:42.510	-27:47:03.10	(26.2)	2.49
134	03:32:42.788	-27:48:56.89	25.66	2.96
135	03:32:42.910	-27:47:01.77	26.92	2.94
136	03:32:42.930	-27:48:19.22	26.82	1.53
137	03:32:43.086	-27:46:46.12	25.91	0.60
138	03:32:43.108	-27:46:14.10	26.05	3.18
139	03:32:43.302	-27:46:43.46	27.08	0.55

Continued on next page...

TABLE 2 – Continued

ID	RA J2000	DEC J2000	i'_{AB} mag[a]	Photometric redshift
140	03:32:43.395	-27:47:14.41	23.79	0.95
141	03:32:43.948	-27:47:13.69	24.34	0.48
142	03:32:43.953	-27:46:45.38	27.82	0.41
143	03:32:43.985	-27:46:33.06	23.24	0.06
144	03:32:44.560	-27:46:23.53	25.82	0.58
145	03:32:44.645	-27:47:02.36	25.67	2.61
146	03:32:44.772	-27:47:08.89	26.04	0.73
147	03:32:44.910	-27:47:58.10	(27.2)	1.89
148	03:32:44.999	-27:46:29.53	25.82	0.23
149	03:32:45.237	-27:46:39.19	26.43	3.14
150	03:32:45.246	-27:46:43.93	25.61	0.40
151	03:32:45.919	-27:47:30.18	26.02	2.44
152	03:32:45.945	-27:47:20.42	24.88	2.58
153	03:32:45.975	-27:46:57.60	23.58	1.43
154	03:32:46.016	-27:47:06.38	25.70	2.77
155	03:32:46.103	-27:47:08.05	27.03	1.16
156	03:32:46.384	-27:48:11.19	25.68	0.41
157	03:32:46.482	-27:47:44.45	26.16	0.50
158	03:32:47.247	-27:47:57.83	25.23	0.90
159	03:32:47.386	-27:47:26.02	25.34	4.06
160	03:32:48.340	-27:47:28.44	26.64	0.79
161	03:32:37.734	-27:47:06.96	23.33	0.60
162	03:32:41.865	-27:46:51.10	23.52	0.71
163	03:32:42.993	-27:47:09.73	23.78	2.74
164	03:32:41.077	-27:48:52.98	20.58	0.28
165	03:32:33.257	-27:47:24.69	(27.3)	5.4[b]

[a] Parentheses indicate estimated aperture magnitudes for visually selected objects.

[b] Redshift from Rhoads et al. 2005.

2.6. Tadpole Galaxies as Tracers of Galaxy Assembly

The fact that about 6% of all field galaxies are seen in the tadpole stage is a measurement with potentially important consequences. In light of simulations by

Springel et al. (2005) that predict a tadpole-like stage $\simeq$0.7 Gyr after a major merger begins, we suggest that this particular tadpole morphology represents an early-merger stage of two galaxies with comparable mass. If this 6% indicates the fraction of time that an average galaxy in the HUDF spends in an early-merger stage during its lifetime, and if most of these low-luminosity objects started forming the bulk of their stars at the end of the reionization epoch at z$\simeq 6-7$ (e.g. Yan & Windhorst 2004a, 2004b), then each galaxy would spend about 6% of 12.9 Gyr (i.e. 0.8 Gyr) since z$\simeq$ 7 in a distinctly recognizable merger or tadpole stage. At the median redshift at which the tadpoles are seen ($z_{med} \simeq 1.6$; see Fig. 3), each object is then seen at an age of about 4 Gyr if born at z$\simeq$7. Each tadpole is $\simeq$ 1" (or $\simeq$ 8 kpc) across (Fig. 1), and given the fluxes measured, each clump in a tadpole has roughly $M \simeq 10^8 - -10^9$ $M_\odot$ in stars (see, e.g., Papovich, Dickinson, & Ferguson 2001 who estimated stellar masses of lyman break galaxies). For these rough estimates of their physical parameters, the freefall timescale for each tadpole is roughly $\tau \lesssim$(few $\times$ 10^7)–10^8 years, or $\simeq$6% of the galaxy lifetime at that redshift. Hence, if every galaxy is seen in a tadpole stage for $\simeq$0.8 Gyr of its lifetime, then it may have undergone $\sim$10-30 mergers during its lifetime. During the early stage of each merger, it would be temporarily seen as a tadpole. More complex mergers may lead to irregular/peculiar and train-wreck type objects and the luminous diffuse objects or clump clusters, which are among the type of objects that dominate the galaxy counts at faint magnitudes (Driver et al. 1998). In this paper, we limit the sample selection to two clumps passing by each other, which we believe leads to the more uniquely classifiable tadpole morphology. Given that

tadpoles only trace a certain type and stage of merging galaxies, the above statistics are likely a lower limit on the number of all mergers. In summary, each galaxy seen today may have had of order one- to two- dozen mergers since most of its Population II stars were born at z$\simeq$7, and given the small masses and short merger timescales involved, would then be seen as tadpole galaxies for about 6% of their life-time.

Figure 4 suggests that tadpole galaxies — if indeed dynamically young objects — appear to occur in the same proportion to the field galaxy population at all redshifts probed in this study. Tadpole galaxies may therefore be good tracers of the process of galaxy assembly. This implies that the process of galaxy assembly — as traced by tadpole galaxies — keeps up with the reservoir of available galaxies as a function of redshift for 0.1$\leq$z$\leq$4.5. Our result is in excellent agreement with the predictions of Robertson et al. (2005) that describe a merger-driven scenario to build up disk galaxies, and is consistent with Rhoads et al. (2005) who conclude that their z=5.4 galaxy (tadpole # 165 in Table 2) is strongly indicative of a galaxy in assembly.

In a companion paper in this issue, Cohen et al. (2005) present a study of the variable objects in the HUDF which have a point source component with a measurably variable flux on timescales of 0.4–3.5 months, which roughly corresponds to 0.5–5.5 weeks in the rest-frame at the median redshift of the sample ($z_{med} \simeq 1.5 - 2$). In particular, they found 45 plausibly variable objects among 4644 galaxies to $i'_{AB} = 28.0$ mag. They argue that these objects are most likely variable because they host weak AGN. Sometimes these AGN are in the galaxy center, but often they occur off-center in a dynamically unrelaxed system. This prompts the question: What fraction

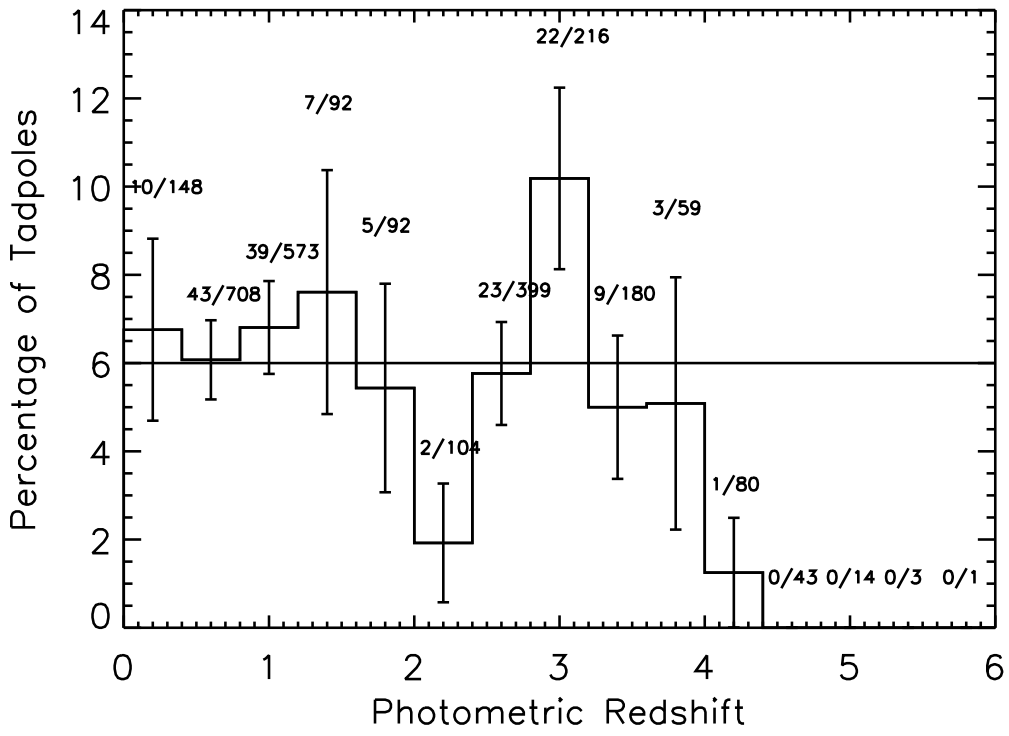

FIG. 4 Percentage of total galaxies that are tadpoles is plotted as a function of photometric redshift. Within the statistical errors, on average about 6% of all galaxies are seen as tadpoles at all redshifts.

of tadpole galaxies contains a variable weak AGN in its knots? This is a critical issue, because it is widely believed that the process of merging in galaxies can also disturb the inner accretion disk around the supermassive black hole (SMBH) and switch on the AGN. Among our 165 tadpole galaxies, none coincide with the sample of 45 variable objects or with the x-ray sources in the Chandra Deep Field South (Alexander, D.M. et al. 2005). Recent state-of-the-art hydrodynamical models (di Matteo, Springel, & Hernquist 2005; Springel, di Matteo, & Hernquist 2005; Hopkins et al. 2005) suggest that during (major) mergers, the black hole accretion rate peaks considerably after the merger started, and after the star formation rate (SFR) has peaked. Specifically, their models suggest that, for massive galaxies, a tadpole stage is seen typically about 0.7 Gyr after the merger started, but $\sim$0.9 Gyr before the SMBH accretes most of its mass, which is when the galaxy displays strong AGN activity. Since the lifetimes of QSO's and radio-galaxies are known to be $\lesssim$(few$\times$ 10^7)–10^8 years (Martini, P. 2004, Grazian et al. 2004), these hydrodynamical models thus imply that the AGN stage is expected to occur considerably *after* (i.e., $\geq$1 Gyr) the early-merger event during which the galaxy is seen in the tadpole stage. The observed lack of overlap between the tadpole galaxies and the AGN sample in the HUDF provide direct observational support for this prediction. Recent studies by Grogin et al. (2005) find asymmetry (A) values that are similar between AGN and non-AGN samples; this result is consistent with our study in light of the theoretical models mentioned above, which indicate that AGN activity is seen only well *after* the merger has taken place and the galaxy has settled into a more dynamically relaxed state.

In addition, Hopkins et al. (2005) have quantified the timescales that quasars will be visible during merging events, noting that for a large fraction of the accretion time, the quasar is heavily obscured. In particular, their simulations show that during an early merging phase — our observed tadpole phase — the intrinsic quasar luminosity peaks, but is completely obscured. Only after feedback from the central quasar clears out the gas will the object become visible as an AGN. This should be observable by the Spitzer Space Telescope in the mid-infrared (IR) as a correspondingly larger fraction of IR-selected obscured faint QSO's.

In conclusion, tadpole galaxies are a class of easily-identifiable, dynamically young objects that exist throughout the history of the Universe and are good tracers of galaxy assembly. They provide strong observational support for the validity of recent numerical simulations, and highlight the importance of mergers to the process of galaxy assembly and AGN growth.

We thank the STScI staff, and in particular Steve Beckwith, Ray Lucas, and Massimo Stiavelli, for their persistent efforts to implement the Hubble Ultra Deep Field in the best possible way. This research was partially funded by NASA grants GO-9793.08-A and AR-10298.01-A, awarded by STScI, which is operated by AURA for NASA under contract NAS 5-26555; as well as by the NASA Space Grant program at ASU, and the Harriet G. Jenkins Predoctoral Fellowship Program.

3. HUDF ELGs: A 2D DETECTION METHOD & FIRST RESULTS

The Hubble Space Telescope (HST) Advanced Camera for Surveys (ACS) grism PEARS (Probing Evolution And Reionization Spectroscopically) survey provides a large dataset of low-resolution spectra from thousands of galaxies in the GOODS North and South fields. One important subset of objects in these data are emission-line galaxies (ELGs), and we have investigated several different methods aimed at systematically selecting these galaxies. Here we present a new methodology and results of a search for these ELGs in the PEARS observations of the Hubble Ultra Deep Field (HUDF) using a 2D detection method that utilizes the observation that many emission lines originate from clumpy knots within galaxies. This 2D line-finding method proves to be useful in detecting emission lines from compact knots within galaxies that might not otherwise be detected using more traditional 1D line-finding techniques. We find in total 96 emission lines in the HUDF, originating from 81 distinct "knots" within 63 individual galaxies. We find in general that [O III] emitters are the most common, comprising 44% of the sample, and on average have high equivalent widths (70% of [O III] emitters having rest-frame EW$>$ 100Å). There are 12 galaxies with multiple emitting knots–with different knots exhibiting varying flux values, suggesting that the differing star formation properties across a single galaxy can in general be probed at redshifts $\gtrsim$0.2-0.4. The most prevalent morphologies are large face-on spirals and clumpy interacting systems, many being unique detections owing to the 2D method described here, thus highlighting the strength of this technique.

3.1. Introduction: A 2D Detection Method for ELGs

It has long been known that galaxies display properties of their star formation through emission lines, and because of this, systematic studies of emission-line galaxies is an ongoing effort in order to investigate galaxies' star formation–and thus evolution–throughout the history of the universe. Projects such as the KPNO International Spectroscopic Survey (KISS; Salzer et al. 2000) have investigated low-redshift emission-line galaxies' properties (Salzer et al. 2001 & 2002). Spectroscopic studies of faint, intermediate-to-high redshift emission line galaxies have utilized large projects such as the CFRS (Lilly et al. 1995, Hammer et al. 1997), COSMOS (Capak et al. 2007, Lilly et al. 2007), and the DEEP1 and DEEP2 projects (Koo 1998, 2003; Willmer et al. 2006; Kirby et al. 2007). With the advantage of slitless grism spectroscopy from the Hubble Space Telescope's (HST) Advanced Camera for Surveys (ACS), larger samples of faint objects — reaching to $i'_{AB} \sim 27.0$ mag — are now possible.

Many detailed studies have arisen from projects such as these. Earlier investigations have highlighted the importance of star formation bursts in interacting galaxies in general (Larson & Tinsley 1978), and subsequent studies have made use of emission-line fluxes to arrive at star formation rates (SFRs; Kennicutt 1998). In particular, Hα emission has been used to derive SFRs and those results have been interpreted in the overall framework of galaxy evolution (Kennicutt 1983). Several studies have highlighted the importance of constraining the current SFR-density in the local universe using emission-line galaxies (Gallego et al. 1995, 2002; Lilly et al. 1995), while others have investigated the evolution of the SFR with redshift (Madau et al.

1998; Cowie et al. 1999). In the context of hierarchical merging, active star formation has long been regarded as a strong indicator of merging activity (Larson & Tinsley 1978), and recent studies have emphasized the evolutionary importance of merging galaxies and their role in AGN growth over cosmic time, both theoretically (di Matteo et al. 2005, Hopkins et al. 2005), as well as observationally (Straughn et al. 2006, Cohen et al. 2006). Studies of these types can be greatly enhanced by larger samples of faint star forming or emission- line galaxies at high redshift.

Slitless spectroscopy has been used often over the past several years to detect emission-line galaxies. In particular, HST's Near Infrared Camera and Multi-Object Spectrometer (NICMOS) and Space Telescope Imaging Spectrograph (STIS) instruments have produced several surveys in which emission-line galaxies have been utilized to arrive at the Hα line luminosity function and SFRs (e.g., Yan et al. 1999; HST NICMOS with the G141 grism), as well as the [O II] luminosity function and star formation densities at intermediate redshifts (e.g., Teplitz et al. 2003; HST STIS with the G750L grism). The ACS G800L grism has also yielded very rich datasets, and the field of slitless spectroscopy with HST has culminated the past few years with the HUDF GRAPES (GRism ACS Program for Extragalactic Science; Pirzkal et al. 2004, Malhotra et al. 2005) project, and more recently with the PEARS (Probing Evolution And Reionization Spectroscopically) survey (Malhotra et al. 2007, in prep., Cohen et al. 2007, in prep.), which combined have yielded thousands of spectra over roughly half the area of the GOODS North and South fields including the HUDF to continuum fluxes of $i'_{AB} \lesssim 27$ mag. From the GRAPES data, studies of emission-line galaxies

have been performed and a catalog has been compiled by Xu et al. (2007) using a 1D detection method described briefly below. Pirzkal et al. (2006) have performed analysis of GRAPES emission-line galaxies' morphologies and evolution, highlighting the importance of studying these objects at $z \gtrsim 1$. A key advantage of this project over similar ground-based studies is that the HST i'-band sky brightness is $\sim$3 magnitudes darker than that from ground-based studies (Windhorst et al. 1994). With all the PEARS data analyzed, we anticipate increasing the sample of faint emission-line objects by a factor of 8–10 compared to the previous GRAPES project. In this methods-oriented paper we describe in detail several techniques aimed at detecting emission-line sources in the PEARS grism data and present our data and results for emission-line galaxies detected in the HUDF using a unique 2D line-finding method, which is shown to detect roughly twice the number of sources as 1D methods on the same data. A subsequent paper will contain the complete catalog of emission-line galaxies detected in the eight remaining PEARS fields, along with more detailed analysis of their properties, including quantitative morphological studies, star-formation rates, and line luminosity functions.

3.2. Data

The PEARS ACS grism survey data consist of eight ACS fields with three HST roll angles each (with limiting AB magnitude $i'_{AB} \lesssim 26.5$ mag; 20 HST orbits per field), plus the HUDF field with four roll angles (limiting AB magnitude $i'_{AB} \lesssim 27.5$ mag; 40 HST orbits total) taken with the ACS WFC G800L grism. The G800L grism yields low-resolution ($R \sim 100$) optical spectroscopy between 6000-9500Å. Four PEARS

fields were observed in the GOODS-N and five fields (including the HUDF) in the GOODS-S. A forthcoming data paper (Malhotra et al. 2007) will describe the PEARS project and data in detail. A description of the related GRAPES project can be found in Pirzkal et al. (2004): both the PEARS and GRAPES projects contain grism spectroscopy from the HUDF. Roll angles for the PEARS HUDF are 71°, 85°, 95°, and 200°. This paper will focus on emission-line galaxies detected in the HUDF, using the optimal of several methods described in Section 3. Preliminary source extraction produced a large catalog of PEARS objects in all nine fields with identifying numbers (Malhotra et al. 2007, in prep.). These PEARS IDs will be used in this paper.

3.3. Methods

This paper focuses on our efforts at identifying an efficient and robust method of detecting emission-line objects in the HST ACS PEARS grism data, particularly in objects with knotty morphologies and in continuum-dominated regions where lines might normally be missed. To this end, we have performed two separate, but related detections of PEARS HUDF emission-line galaxies that both rely on a unique 2D detection method, motivated by the observation that many emission lines originate from clumpy knots within galaxies (Meurer et al. 2007, Straughn et al. 2006b). Our results from these two 2D methods (hereafter "2D-A" and "2D-B", described in detail below) will be compared to a separate method of detecting emission-line objects which relies on searching for lines in 1D extracted spectra from the HUDF PEARS data, as was also done for the GRAPES HUDF data (Xu et al. 2007).

The 2D detection procedure begins with pre-processing of the grism data, as

described in detail in Meurer et al. (2007); here we give a brief description. Each image (both the grism and the direct i'-band (F606W) image) was first "sharpened" by subtracting a 13x3 median smoothed version of the image from itself in order to remove most of the continuum from the grism spectra, leaving mostly compact features in the grism image. In this step, the long axis of the smoothing kernal is aligned with the dispersion axis of the grism. These are primarily emission lines in individual object spectra, as well as some residual image defects. This method was designed to detect lines in objects where continuum dominates and lines would otherwise be washed out. After this unsharp-masking stage, the next step is to mask out the images of the zero-order in the grism images. This is accomplished by matching compact sources found with the SExtractor program (Bertin & Arnouts 1996) in both the sharpened grism and direct images. This defines a linear transformation matrix which can be used to transform pixel coordinates from the direct to the grism frame, as well as scaling factor between the count rate in the direct image to that in the zero-order grism image (as described by Meurer et al. 2007). The geometric transformation is also used to derive a precise calibration of the row-offset between direct image sources and sources in first-order spectra. We determined that the transformation and row-offset are stable with HST pointing and roll-angle, and hence adopted the same values for all pointings. The mask is made by using the count-rate scaling to locate all the pixels in the direct image expected to be brighter than the noise floor in their zero order grism image. These are transformed to the grism coordinates, grown in size by three pixels to encompass the zero-order detection, and the resultant

pixels are set to zero. Finally, SExtractor is used to catalog the masked filtered grism images in order to arrive at a list of emission-line source candidates, which is the input to both 2D emission-line source selection methods.

3.3.1. Method 2D-A: Cross-Correlation

The first of the 2D methods ("2D-A") is a blind selection that relies on cross-correlation between the direct and grism sources, and is partially interactive (Meurer et al. 2007). Because of the interactive step, it is desirable to limit the amount of known contaminants that go into the algorithm. Since stellar sources often display a very strong continuum, sources with high SExtractor elongation parameters (ELONGATION$>$ 2.5) in the dispersed grism image were filtered from the catalogs to decrease the number of stellar sources. Sources that are very large or very small in the sharpened grism image are filtered out by only selecting sources with SExtractor parameter "FWHM" in the range of 1 to 10 pixels. This filtering reduces the number of sources that go into the 2D-A code approximately by half. Using these filtered catalogs, candidate emission lines are examined first in the grism image, and then the corresponding direct sources are located in the detection image. This is a semi-automated process in which lines in the grism image are displayed automatically, and the validity of each source is subsequently determined by eye. These potential emission-line sources are flagged as either: (1) a star; (2) a grism- or detection-image blemish (in which two cases the source is skipped); or (3) real, in which case the following is performed. For each "real" grism emission-line candidate, 5-pixel wide ribbons are extracted from both the grism and direct images, centered on the y-position (ver-

tical in Figure 5) of the source. The grism image ribbon is then collapsed down to a 1D spectrum. This spectrum is then cross-correlated with the direct image, and peaks are produced in the cross-correlation when knots within the direct image are detected that correspond to the grism image emission line. Typically only one peak is found in the cross-correlation yeilding a unique correspondence between line and emitting source. However, multiple peaks can occur due to the presence of multiple knots within galaxies or separate galaxies in the direct image ribbon. In those cases the corresponding source is selected manually. The correct choice is usually obvious from the location of the knot in the cross-dispersion direction (centered in the ribbon) or from the shape of the knot compared to the emission line in the filtered direct and grism images (Figure 5; also cf. Figure 1 of Meurer et al. 2007).

The 2D-A line-finding software produces an output list for each position angle with the detected emssion lines. In many instances, multiple knots with emission lines are detected in a single object. Catalogs are then matched to determine which emission-line sources are detected in multiple position angles. The final catalog for the 2D-A method was created by selecting sources which appear in at least two position angles (PAs).

3.3.2. Method 2D-B: Triangulation

The second 2D technique ("2B-D") uses triangulation. It starts with the same input catalog as above, but without any prior filtering and omission of sources based on their elongation and FWHM (however known M stars are removed from the catalogs beforehand). This method works because each source, and hence emission line,

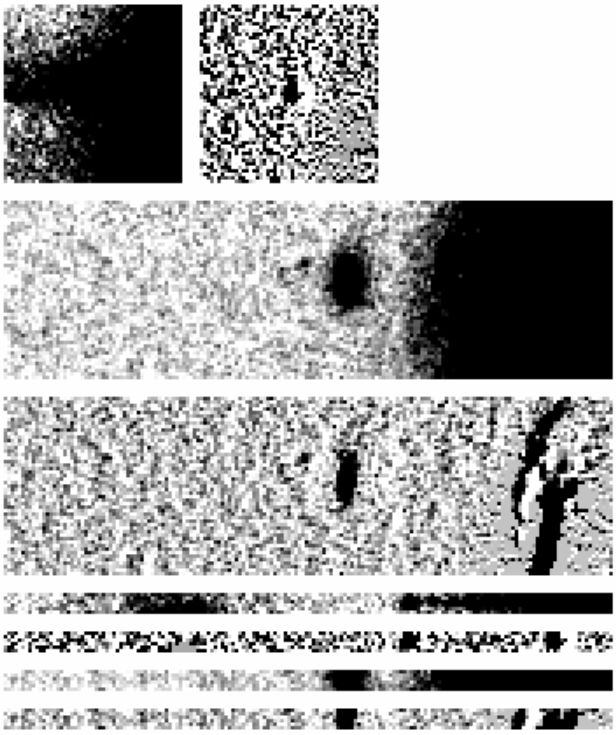

FIG. 5 Example of an object selected using Method 2D-A. Top panels show unfiltered grism image spectrum (left) and the same spectrum after median filtering (right). Middle two panels show direct image source both before and after the same median filtering. Bottom four panels show the 5-pixel wide "ribbons" (top two: grism; bottom two: direct) used in the correlation step to determine which direct image source the emission line originates from.

was observed at more than one PA on the sky, as is the case for our dataset. The ACS grism and ACS distortion are calibrated well enough so that one can map the position of emission-line sources detected in a distortion corrected grism image back onto the original distorted grism images, as well as onto true sky coordinates of RA and Dec (instead of simply using the detector x,y coordinates). When this is done for more than one PA, as shown in Figure 6, one can infer the location of the source of the emission line, which must necessarily lay somewhere along the direction of the grism dispersion. Once the source of the emission line has been inferred on the sky, we compute the wavelength of the detected emission line independently and along all PA dispersion directions (i.e. in all grism images where the line was detected). A true emission line source results in the same wavelength being derived (within an

error that we set to 40Å, roughly one pixel), while a spurious detection leads to inconsistent results where the computed wavelength of a line is different when computed in different PAs. Since we have more than 2 observations taken in more than 2 PAs for this field, we actually used the method described above several times, using different pairs of PAs (i.e. 71° vs 85°, 71° vs 095°, etc..), as illustrated in Figure 6, looking for emission-line sources that produce consistent results for as many PA pairs as possible.

3.3.3. Redshifts and line identifications

Three separate catalogs were used to obtain redshifts for the selected emission-line objects. First, photometric and spectroscopic redshift catalogs are from the GOODS-MUSIC sample (Grazian et al. 2006 and references therein). Spectro-photometric redshifts from Cohen et al. (2007) were used to supplement the MUSIC catalog when no MUSIC photometric redshift was available; this was the case for 16 objects. We also use Bayesian photometric redshifts (BPZs) from Coe et al. (2006) for the two objects (PEARS Objects 75753 & 79283) that had no spectroscopic redshifts, or MUSIC/Cohen photometric redshifts. Sixteen sources have 2 emission lines, allowing an immediate redshift determination using the ratio of line wavelengths which is invariant with redshift (note that given the grism resolution of $R \sim 100$, Hβ and the [O III] doublet are usually blended). About a third of the sample ($\sim$32%) has spectroscopic redshifts and 95% have photometric redshifts. In total, three objects do not have any published redshift. Of these three, two (78237 Knot 1 & 89209) have 2 lines each, and thus a redshift was determined based on the wavelength ratios. The redshifts are used to help identify the emission lines in the grism spectra. Spectra with two

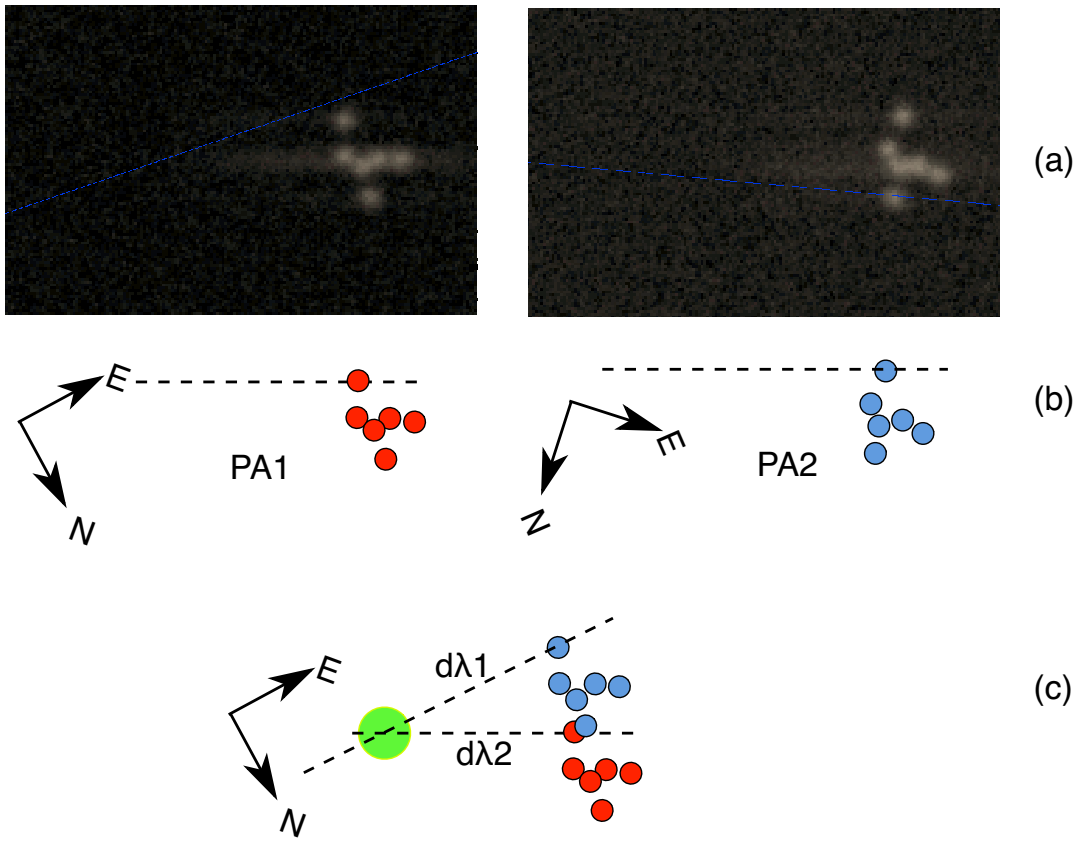

FIG. 6 The top two panels (a) show a series of emission lines observed at two different position angles (PA1 on the left, PA2 on the right). In both cases, the dispersion direction of the grism is nearly horizontal, as shown in (b), where we noted the true direction of North and East. Finally, the bottom diagram in (c) shows the remapping of the grism dispersion (dashed lines) onto the true sky (e.g. RA and Dec). As shown in (c), once remapped onto the sky, the two dispersion solutions intersect at a unique location (shown using the large circle). The latter is the inferred location of the source of the emission on the sky. We can then compute the expected wavelength of the emission line following the PA1 dispersion relation (dλ1) and following the PA2 dispersion relation PA2 (dλ2), and the two should agree (within the expected uncertainty).

distinct lines are in the minority (16 of 81 galaxy "knots"); most spectra have a single emission-line detection.

For objects with only one emission line, line identification then proceeds as follows. For the given object's redshift (spectroscopic when available; photometric otherwise), potential wavelengths are calculated for Hα, [O II], [O III], Lyα, [MgII], C III], and C IV. An average spectro-photometric redshift error of $<\delta z>=0.04\times(1+z)$ (Ryan et al. 2007, Cohen et al. 2007, in prep., Coe et al. 2006) is used to calculate the likelihood of an identification as follows. Using the 4% photometric redshift error, a valid wavelength range for each potential line is calculated. Here, we also include the estimated 20Å wavelength calibration uncertainty (Pirzkal et al. 2004) intrinsic to the grism data. If the detected emission line candidate falls within the calculated wavelength range for any of the lines listed above, it is included in our final catalog. Once a confident line identification is made, we use the wavelength to recalculate the redshift; these new redshifts are given in Table 1. In comparing grism redshifts to spectroscopic redshifts, Meurer et al. (2007) arrive at a dispersion about unity of 0.007 for the 2D-detection method described here for secure line IDs (i.e., sources with two lines, or Hα or [O II] emitters, as these are typically the only plausible lines in the wavelength-range for that redshift). Line fluxes, rest-frame equivalent widths, and errors are then calculated by fitting gaussian profiles to the spectra using a non-linear least-squares fit to the given spectrum from five free parameters: the gaussian amplitude, central line wavelength, gaussian sigma, continuum flux level, and a linear term. Here we include a linear term in the fit to account for instances where the

continuum is not flat. Line fluxes are averaged when the line is detected in two or more roll angles.

3.4. Results

The primary goal of this work is arrival at a robust and efficient technique to identify emission-line sources from the PEARS grism data that is as automated as possible. To this end, we have investigated in detail two versions of a 2D detection method as described in the previous section. Methods 2D-A and 2D-B produced 75 and 96 lines respectively, originating from multiple knots within galaxies. This is compared to 43 lines detected with the 1D method on the same data. Details of the results of these comparisons are discussed here, as well as a comparison to a catalog of emission-line galaxies generated from the related GRAPES grism data (Xu et al. 2007) using the 1D detection method.

3.4.1. ELG detections from three different methods

We summarize here in more detail detections resulting from three different methods outlined above. Note here the terminology used resulting from our 2D method: "lines" (sources detected in the grism image and hence distinct in position and wavelength), "sources" (which refer to individual clumps or knots within a galaxy), and "galaxies" (for example, one galaxy can contain three sources which each have two lines). The 1D line-finding method (as described in detail by Xu et al. 2007 for the GRAPES data) involves selection of emission lines from the 1D spectra generated by aXe [1] with visual confirmation. For the PEARS HUDF, 62 candidate lines were detected, 19 of which were flagged with a quality code indicating a contami-

[1] http:/stecf.org/instruments/ACSgrism/axe

nant or M-dwarf, resulting in a catalog of 43 PEARS galaxies. These remaining 43 galaxies are then compared to the catalogs generated by the two versions of our 2D line-finding method. Method 2D-A, the cross-correlation technique (§ 3.1), produced a final catalog of 75 lines, all of which originate from valid faint emission-line sources, since contaminants are thrown out in the user-interactive phase of the process described above. Individual PAs had 78, 114, 106, 77 detections in PAs 71°, 85°, 95°, and 200° respectively; 75 of these were detected in at least 2 PAs. Method 2D-B, the triangulation technique (§ 3.2), produced a total of 96 lines. Method 2D-B also requires that an emission line be in more than one PA; in the final sample of 96 lines obtained with this Method, 12 were in two PAs, 38 were in three PAs, and 46 were in all four PAs.

Method 2D-A, described in detail in the previous section, requires some explanation of the results obtained since the software that produces the catalog is partially user-interactive. For PA085, two of the authors (ANS and GRM) ran the blind emission line-finding software on the data and compared results for completeness. It was found that there was a large (90%) overlap in final sources obtained between both users, suggesting that the method is robust in detecting secure emission-line sources, and user dependancies introduce relatively little bias. An investigation of the sources that were selected by one user and not the other shows several cases of multiple emission lines in knotty galaxies that often were offset from the other user's detection by only a very small amount. There are a few cases of isolated galaxies where only one user detects a line. In general, the differences appear to be legitimate operator

differences, and account for $< 10\%$ of the detections. Those operator errors that are false detections are effectively weeded out by the requirement that the sources match in multiple PAs.

As described above, Method 2D-B (which uses traces in the grism image to determine the direct image emitting source) detects the most real lines in the PEARS data and discards spurious detections automatically. Because of this, it appears to be the most efficient and robust technique to detect emission-line sources in the grism data, and below we compare this method to the other two methods described here (Method 1D and Method 2D-A).

3.4.2. Comparison of Method 2D-B to Method 1D

First, we compare to the 1D method used on the same PEARS data. Here we find that Method 2D-B detects 1.9× as many sources for this field. Overall, the overlap between the two methods is 72%, with the 1D method detecting 12 unique sources and the 2D method detecting 50 unique sources. We note here that the input to the 1D method is the SExtractor catalog of entire galaxies, in contrast to our SExtractor catalog of individual galaxy knots. Thus in regard to the 1D method, the emission lines are diluted by the continuum and the equivalent width goes down below the detection limit. An inspection of the initial 2D-generated input files in comparison to these 12 1D-detected but 2D-undetected sources shows several aspects of interest. First, the majority of these 12 1D-detected sources are clustered along the edges of the field, with only 3 of them extending inwards more than 700 pixels (or 1/5 the width of the image). This suggests—and was confirmed on more detailed

inspection—that many times the object in question is undetected in at least one PA (sometimes up to three PAs), and would thus not make it into the final catalog produced by the 2D-B method. Second, we notice that only in a very few cases are there any SExtractor detections located along the dispersion direction for any given 1D-only detected object. This shows that these sources were not in the input SExtractor catalogs because they were below our 2D-detection limit, thus explaining the absence from our final 2D-B ELG catalog. Figure 8 shows an estimate of signal-to-noise for these 1D-detected objects, and indicates that the 1D-detected objects that were missed by the 2D method were in general lower S/N and likely below our detection limit imposed in the initial grism emission-line catalog selection.

Figures 9–11 show some examples of 2D-detected galaxies with several emitting knots. These composite images were created using the HUDF F435W (B), F606W (V), F775W(i'), and F850LP (z') data. Objects 70314 and 78491 were not detected using the 1D technique. This is likely due to continuum flux dominating the spectrum, an effect which was mitigated in our technique by the sharpening process (see Section 4.6 for a full discussion of these objects). Therefore, in general, it is shown that the overlap between Method 1D and Method 2D-B is large, and the 1D objects missed by the 2D-B Method are due to our imposed detection threshhold. In total, the 2D Method finds almost twice as many sources.

3.4.3. Comparison of Method 2D-B to Method 2D-A

Given that Method 2D-B was developed in conjunction with Method 2D-A, a comparison between these two methods is warranted as well. As described above, both

methods have identical input catalogs for each PA, with the exception that the input to method 2D-A was pared down to avoid selection of undesired objects (i.e. stars) in the user-interaction phase of the analysis. Comparison of Method 2D-B to Method 2D-A shows that all but 2 sources detected by Method 2D-A were also detected by Method 2D-B, an overlap of 96%. Additionally, the level of human interaction is greatly reduced in Method 2D-B, making it both more efficient and reliable.

3.4.4. Comparison of Method 2D-B to GRAPES catalog

Although the GRAPES project (Pirzkal et al. 2004, Malhotra et al. 2005) involves a different dataset than the one used for the present work, a comparison of our results to the previous GRAPES ELG catalog in Xu et al. (2007) is explored here since the data are for approximately the same field. Figure 7 gives a graphical comparison of the PEARS and GRAPES fields centered on the HUDF. The process used to arrive at the GRAPES ELG catalog is the same as "Method 1D" described above, with some manual additions (approximately 10%) of objects after visual examination of all the individual spectra as described in that paper. The first difference in the two datasets is that the Xu et al. (2007) ELG catalog utilized the GRAPES data (40 HST orbits) plus one epoch of preexisting ACS grism HUDF data, increasing the observed grism exposure time by about one-fifth (Pirzkal et al. 2004) and also increasing the overall combined area observed. Second, since the fields are not exactly overlapping, there are some GRAPES ELG objects that are not in the PEARS fields and vice versa. Given these factors, the comparison is not as straightforward as, e.g., the comparison to the 1D Method applied to the identical PEARS data, as described above.

However, when doing the comparison, we find that 61% of the 2D-B detected sources are in the GRAPES catalog, with 37 unique lines appearing in the 2D-B catalog only. Of the 39% of GRAPES sources unique to the GRAPES catalog, many are found to exist outside of the PEARS observing area. Specifically, 44%, 34%, 34%, and 27% of the 2D-B-undetected GRAPES sources fall outside the four PEARS roll angles 71°, 85°, 95°, and 200° respectively. In total, there are 35, 41, 41, 45 sources in the four respective PEARS PAs that are not detected with Method 2D-B. The sources that were detected with the 1D Method from GRAPES but were missed by 2D-B in general were missed for the same reason as with Method 1D used on the PEARS data (as described in Sec. 4.2): those missed were below our S/N threshhold required for Method 2D-B (Figure 8). In particular, the missed objects generally have S/N$\sim$2$-$3, while most of our objects detected in GRAPES generally have higher S/N values. We thus conclude that this is the same effect as was seen when comparing to Method 1D for the PEARS data. This is expected given our detection limit which serves to greatly increase the reliability of our 2D detection method.

3.4.5. ELG catalog and statistics

Our final catalog of PEARS HUDF emission-line objects, derived from the most efficient method investigated here—Method 2D-B—is given in Table 1. In total, 96 distinct lines were detected in 81 galaxy sources or "knots" in 63 PEARS galaxies. Examples of galaxies with several emitting knots are shown in Figures 9–11, demonstrating the strength of the 2D Method as compared to the 1D Method. In addition, Figure 12 shows how the 2D Method is able to detect lines in galaxies that were

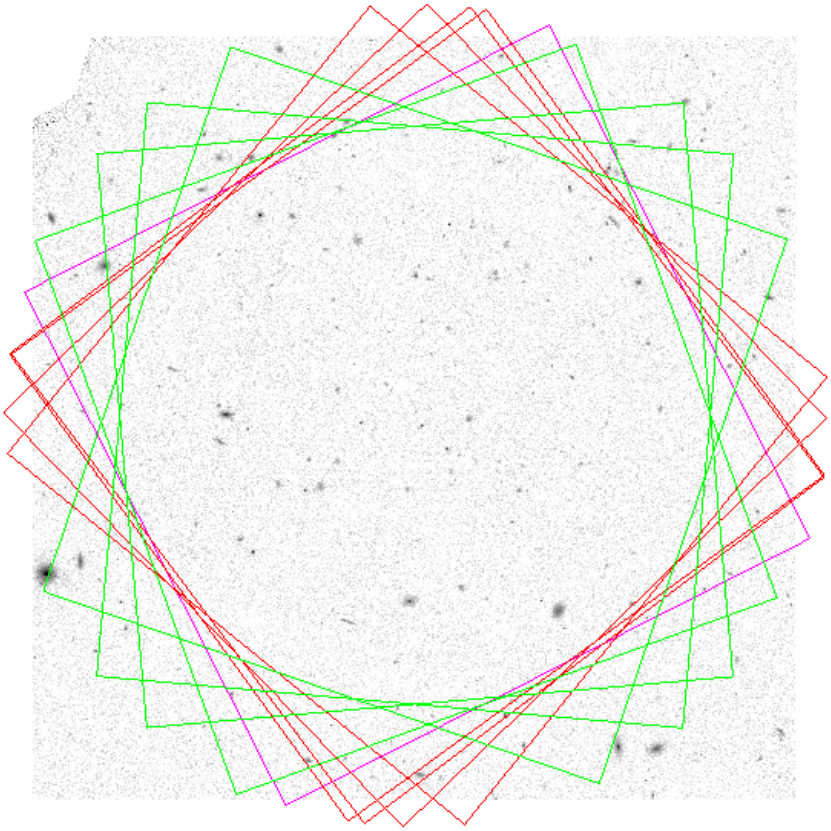

FIG. 7 The four PEARS HUDF pointings are shown in green, as well as the four GRAPES shown in red (plus one archival ACS grism field uses in the GRAPES study shown in magenta; see Sec. 2). All PEARS and GRAPES fields are centered on the HUDF. Eight additional PEARS fields will be analyzed in a future study: four fields in the GOODS-N and four more in the GOODS-S.

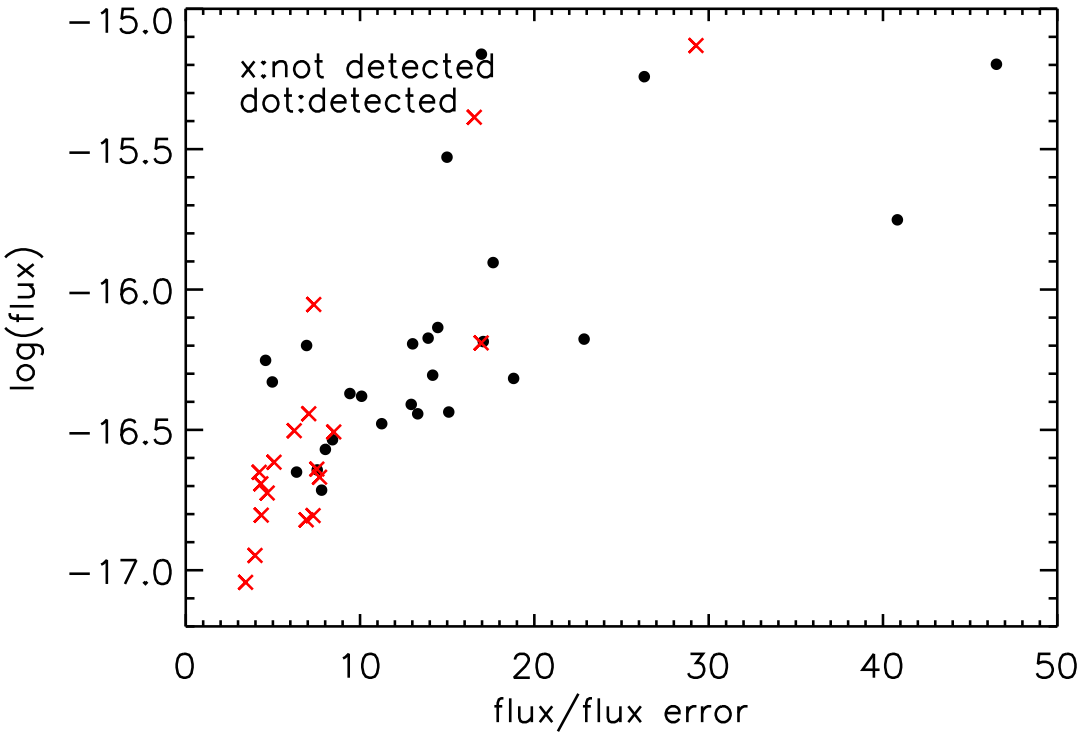

FIG. 8 Signal to noise estimates of PEARS objects detected with the 1D Method. Black dots are 1D-detected objects that are also detected with our 2D-B Method; red x's are 1D-detected objects that are missed by the 2D-B Method. Fluxes are from Xu et al.. In general, objects missed by Method 2D-B are lower S/N, clustered below S/N$\sim 8-10$.

undetected by the 1D Method due to strong continuum overwhelming the emission lines. The percentages of identified lines are as follows: 34% are Hα , 14% are [O II], and 44% are [O III], with 3% accounting for other less common lines (MgII, C III], and C IV). Our catalog includes 39 new spectroscopic redshifts for galaxies that are on average fainter than the standard magnitude limited redshift survey (z'_{AB} = 23.5 mag for ground-based GOODS spectroscopic redshifts; Elbaz et al. 2007). The faintest ELG has a continuum i'_{AB} = 27.4 mag, and the average continuum magnitudes of Hα , [O II], and [O III] emitting galaxies are i'_{AB} = 21.9, 24.1, and 23.6 mag respectively. The magnitude distribution of the sample is given in Figure 13.

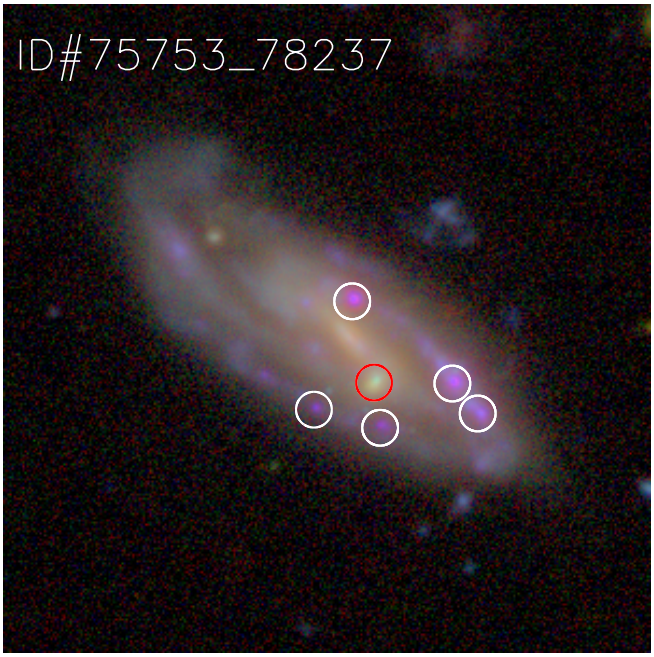

FIG. 9 PEARS Objects 75753 & 78237. Stamp is 9" across; this galaxy has a redshift z = 0.339. These were extracted as two sources but are part of the same galaxy. The knot indicated by the red circle is likely an interloper with an undetermined redshift. The other five knots all contain Hα and/or [O III] emission; flux values are given in Table 1.

The faintest line flux is 5.0×10^{-18} ergs cm^{-2}s^{-1}, with the average line flux being 3.9×10^{-17} ergs cm^{-2}s^{-1}. The [O III] emitters have on average high equivalent widths, with 70% of them having $EW > 100$Å. The line flux distribution for all sources is

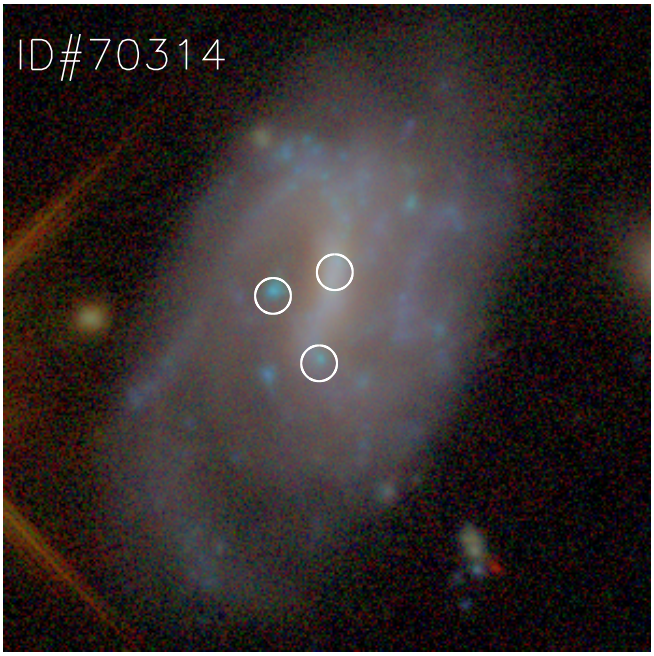

FIG. 10 PEARS Object 70314. Stamp is 9" across; this galaxy has a redshift $z = 0.144$. All three knots have Hα emission. The line from the nuclear region of the galaxy has an equivalent width $\sim$4$\times$ smaller than that from the other two knots. This result highlights the strength of the 2-D Method utilized here: this galaxy has no detected lines using the 1-D Method in either the PEARS or GRAPES data, presumably because the line flux was overwhelmed by continuum flux when light from the entire galaxy was extracted. However, narrowing in on individual knots allows us to see the line emission.

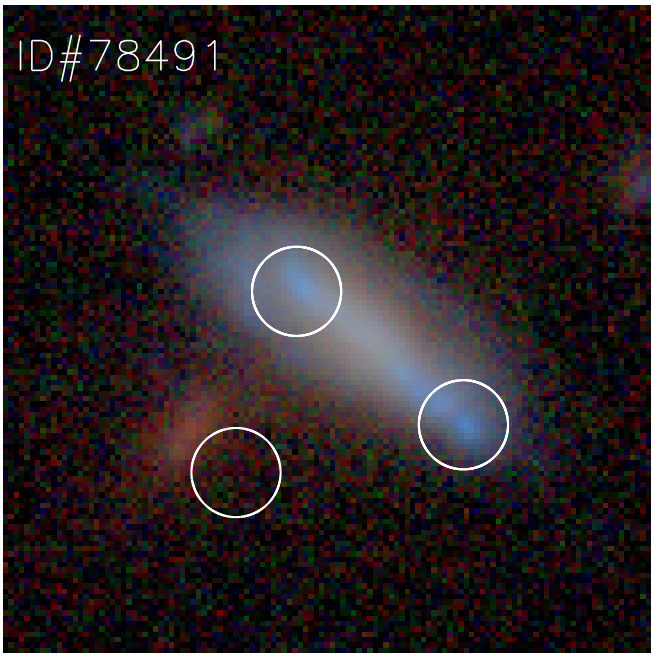

FIG. 11 PEARS Object 78491. Stamp is 3.6" across; this galaxy has a redshift $z = 0.234$. The two blue knots on the ends of the galaxy each have Hα and [O III] emission; the knot on the left-hand side of the galaxy has stronger [O III] flux by a factor of ~ 2 and the right-hand side knot has slightly stronger Hα flux. The third circled "knot" is clearly not part of this PEARS galaxy, although it is emitting a very strong line ($EW = 237.0$Å) at $\lambda = 7143$Å. No redshift is available for this object, however, so line identification is not possible.

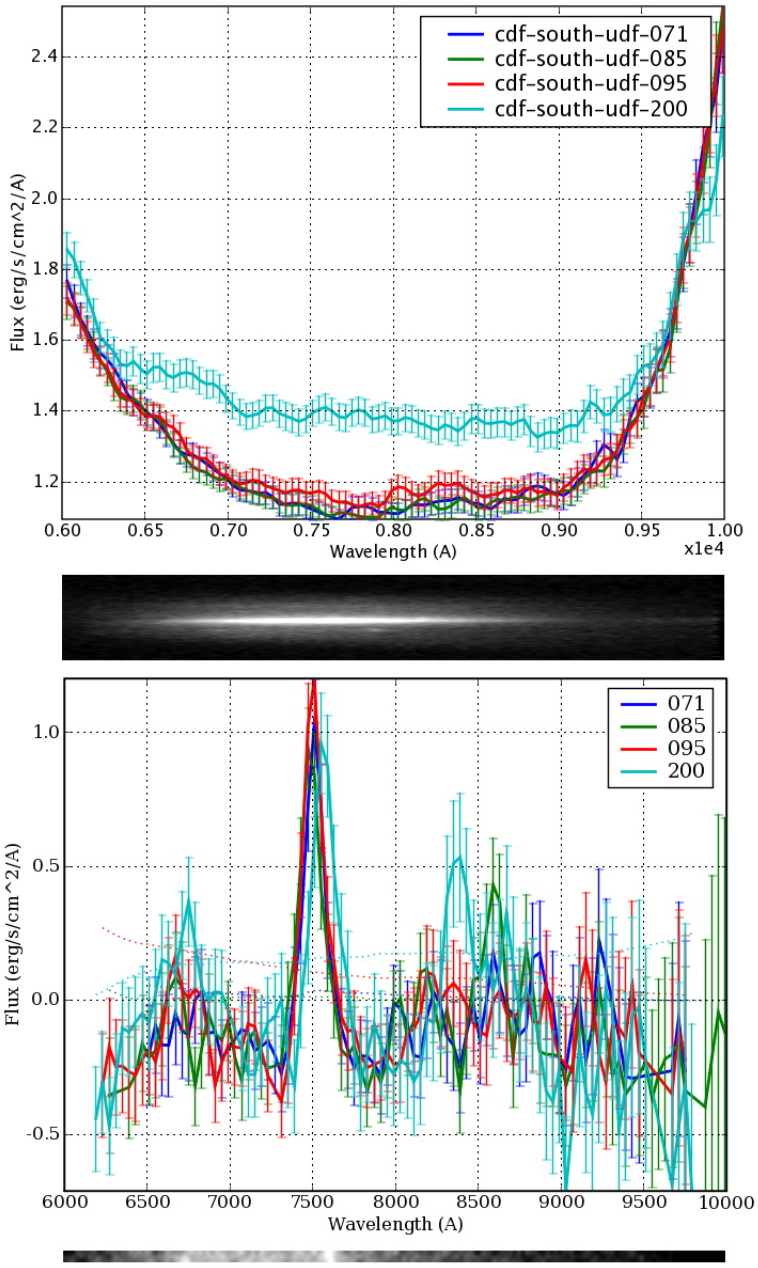

Fig. 12 (a): 1D extraction of PEARS Object 70314 (entire galaxy; see also Figure 10). Top panel shows the 1D spectrum from 1D extraction; bottom panel shows the 2D spectrum of this object. Top-right inset gives labels for the four HST roll angles used in this dataset (71°, 85°, 95°, and 200°). Scale of y-axis is in units of 10^{-17} (b): 2D extraction of Knot # 2 in the same galaxy. Panels and inset are the same as in (a). Here the y-axis scales in 10^{-19}. This is an example of the success of the 2D extraction method: no lines are detected when the 1D extraction of the entire galaxy is performed. However, the 2D extraction of three separate emitting knots in this galaxy reveals strong emission lines in the spectra of all three knots.

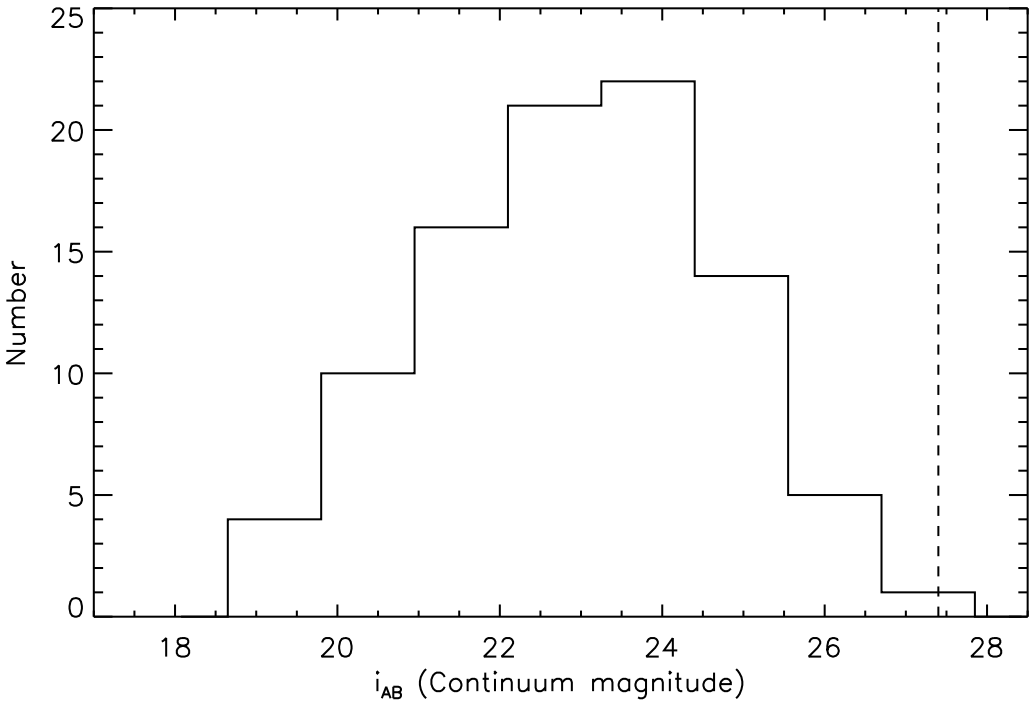

FIG. 13 Histogram of i'-band magnitudes of all PEARS HUDF emission-line objects, showing a peak in the distribution around $i'_{AB} \simeq 24$ mag. The PEARS HUDF continuum detection limit is $i'_{AB} = 27.4$ mag (Malhotra et al. 2007, in prep.).

given in Figure 14, while Figure 15 gives the line flux distributions for the individual lines.

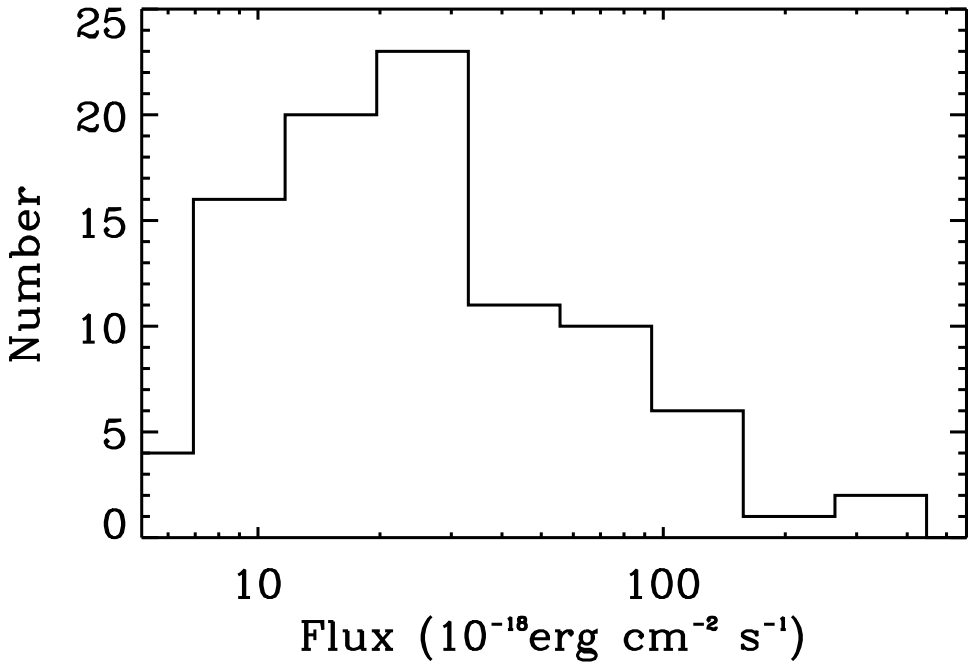

FIG. 14 Line flux distribution of all lines detected with Method 2D-B, in units of $10^{-18} ergscm^{-2}s^{-1}$.

An interesting potential trend appears in Figure 16, which shows the equivalent width of PEARS HUDF [O II] lines as a function of redshift as compared to nearby galaxies from Jansen et al. (2000) and intermediate redshift galaxies from the CFRS sample (Hammer et al. 1997). It is clear that the EW of the PEARS [O II] sources are extremely high compared to local samples–especially above $z \sim 1.1$. Here we note that grism selection of [O II] emitting regions systematically selects higher-EW objects in the [O II] redshift range probed by the grism (which could be due to the smaller HST PSF including less continuum from the surrounding area of the knot,

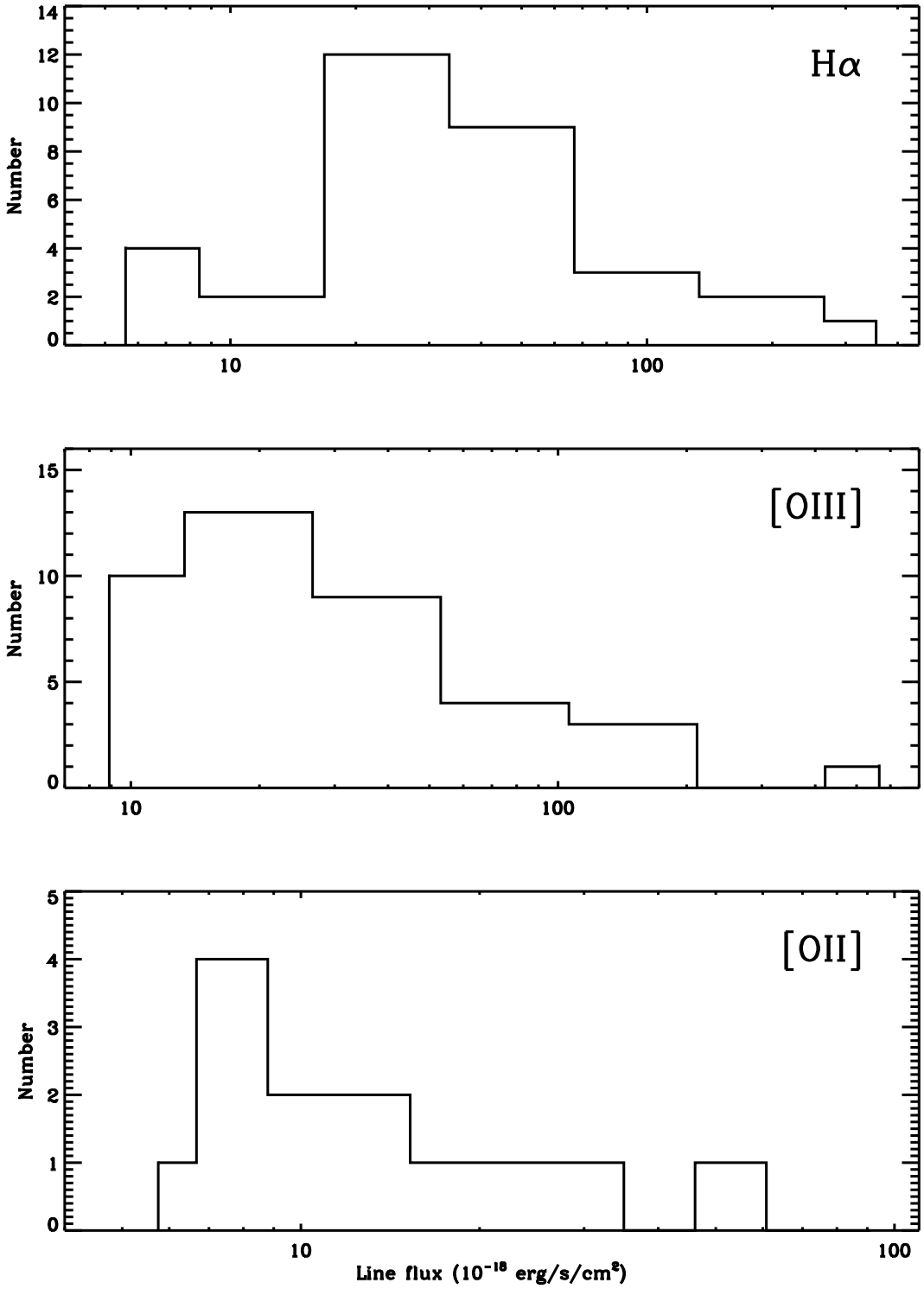

FIG. 15 Individual flux distributions of Hα, [O III], and [O II] lines. The distributions peak at $\sim 2.5 \times 10^{-17}$ ergs cm^{-2}s^{-1} for Hα and [O III], and near 5.0×10^{-18} ergs cm^{-2}s^{-1} for [O II].

thus raising the observed EW; see the sensitivity limit plotted in Figure 16). Hence the fact that the average EW is higher than local galaxies is not surprising. However, the discovery of [O II] emitters with EW$>$ 100Å is interesting. These are exceedingly rare in the local universe (Jansen et al. 2000), and here we only see them at the highest redshifts ($z > 1.1$). As shown in Figure 16 they are also known from previous ground-based surveys (CFRS; Hammer et al. 1997), and appear to be more common with increasing z (Cowie et al. 1996). Sources with similar (and higher) EW([O II]) were also reported in previously published HST slitless observations (Meurer et al. 2007; Teplitz et al. 2003). Teplitz et al. (2003), in particular, find a high incidence of EW $\gtrsim$100Å [O II] emitters at z$\lesssim$0.5, while noting that at high redshifts, lower EW lines might have been missed in comparative surveys. While statistics are low presently, and thus no definite statement can be made concerning this trend, several possible explanations of its origin exist. For example, strong evolution of galaxies' star formation properties with redshift would cause this occurance of very high [O II] EW at high redshift. Additionally, lower extinction between the sources of ionizing radiation and the gas would produce higher EW values. However, this phenomenon could also be caused by cosmic variance; the comoving volume of the PEARS HUDF is clearly much less than the local sample and the 0.2 $\lesssim$z $\lesssim$1.0 sample, and this effect could influence results presented here. As an example of this effect, Takahashi et al. (2007) found that [O II] emitting star-forming galaxies in the COSMOS field show clustering tendencies at redshifts z$\gtrsim$1.2. We anticipate a better study of this phenomenon when the other eight PEARS fields are analyzed and simulations of the data are available

to aid in sorting out various selection effects.

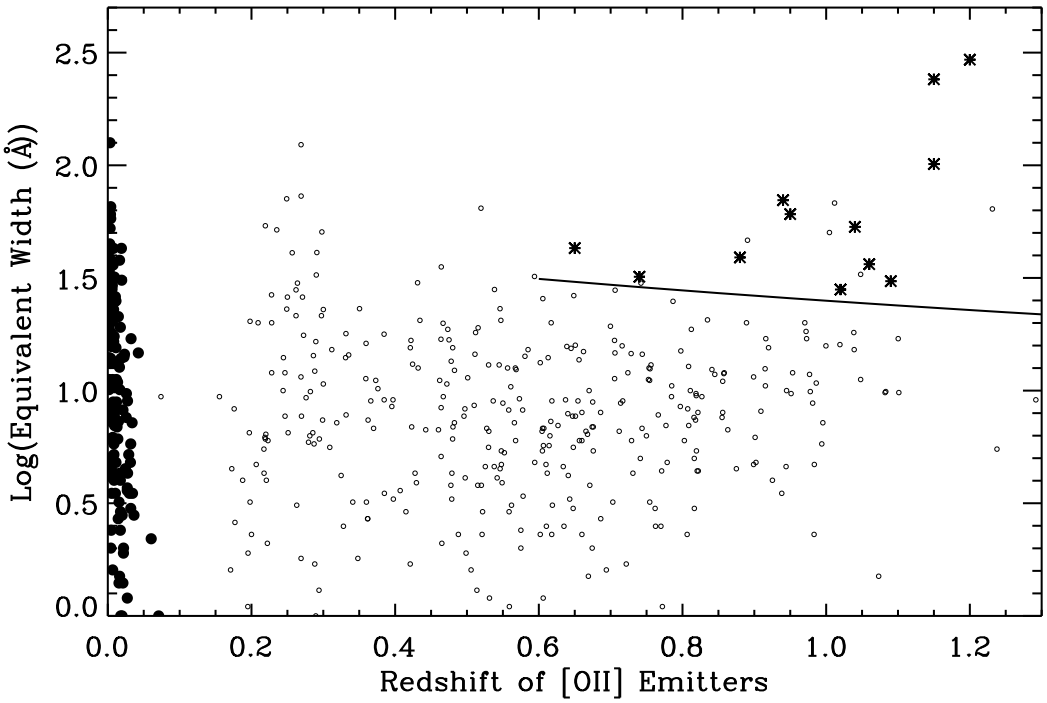

FIG. 16 Rest-frame equivalent width as a function of redshift for [OII] emitters. Stars are PEARS HUDF [O II] emitters, filled dots are from Jansen et al. (2000) and small dots are from the Canada-France Redshift Survey (Hammer et al. 1997). For our sample, [O II] can be detected in the redshift range $0.6 \lesssim z \lesssim 1.5$ given the grism range 6000-9500Å. Approximate PEARS selection limit is given by solid line.

The redshift distribution of these ELGs is shown in Figure 17, with the majority of redshifts lying between $z = 0$ and $z = 1.5$ and the peak occuring around $z \sim 0.5$. Since the identified lines—which are only observable at the redshifts in the plot—are generally the strongest lines in star-forming galaxies, this explains why the emission-line N(z) peaks at a lower z_{max} than the field galaxy photometric redshift distribution which peaks at $z \sim 1-1.5$. This is thus in part an artifact of the ACS grism selection function (see Malhotra et al. 2005).

Redshift distribution for PEARS ELGs showing peak of distribution around z$\sim$0.5. Given the grism properties (sensitive from 6000Å to 9500Å), the Hα line is observable from 0 $\lesssim$z $\lesssim$0.4; [O III] from 0.1 $\lesssim$z $\lesssim$1.1, and [O II] from 0.4 $\lesssim$z $\lesssim$1.5. The one object at higher redshift in this figure is the AGN (C IV C III] emitter) at $z = 3.17$. Because the identified lines are only available at these particular redshifts (and are generally the strongest lines in star-forming galaxies), the emission-line N(z) peaks at a lower z_{max} than the field galaxy photometric redshift distribution which peaks at z$\sim$1–1.5 (Ryan et al. 2007, Cohen et al. 2008, in prep.).

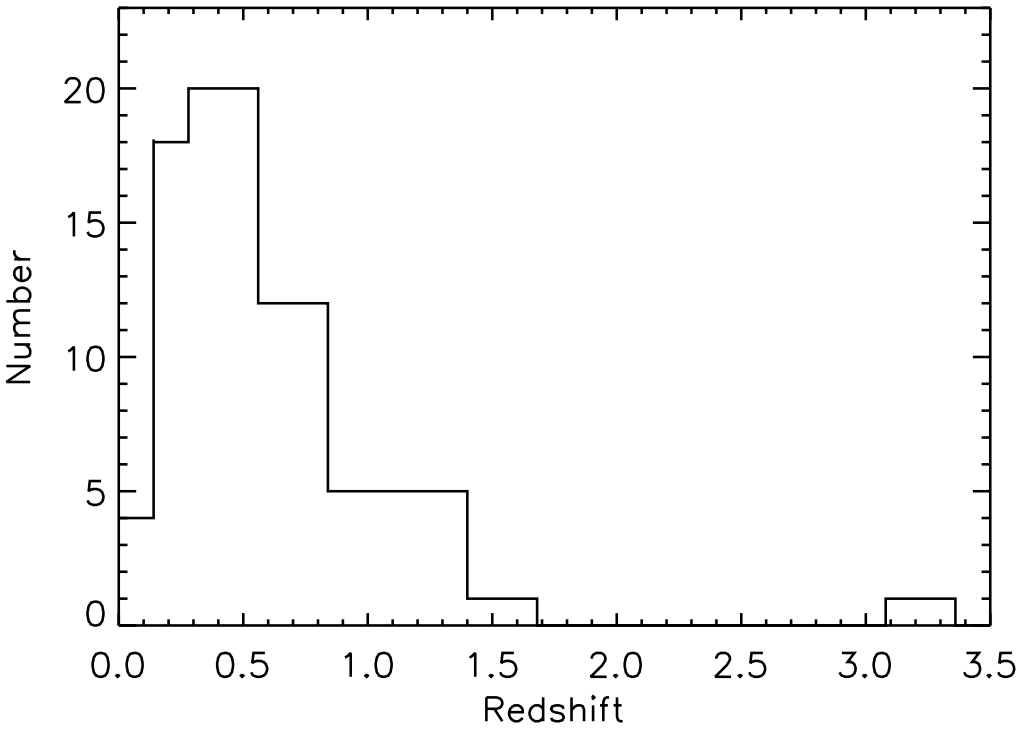

FIG. 17 Redshift distribution for PEARS ELGs showing peak of distribution around z∼0.5. Given the grism properties (sensitive from 6000Å to 9500Å), the Hα line is observable from 0 $\lesssim$z $\lesssim$0.4; [O III] from 0.1 $\lesssim$z $\lesssim$1.1, and [O II] from 0.4 $\lesssim$z $\lesssim$1.5. The one object at higher redshift in this figure is the AGN (C IV C III] emitter) at $z = 3.17$. Because the identified lines are only available at these particular redshifts (and are generally the strongest lines in star-forming galaxies), the emission-line N(z) peaks at a lower z_{max} than the field galaxy photometric redshift distribution which peaks at z∼1–1.5 (Ryan et al. 2007, Cohen et al. 2008, in prep.).

A qualitative look at the morphologies of the emission-line galaxies (in B, V, i', z'; see Figure 9–11) suggests that the majority of these objects are clumpy, knotty galaxies that have distinct emitting regions of presumably active star formation. In particular, we find many face-on knotty spirals, as well as clumpy interacting systems with regions of enhanced star formation that were missed with the 1D Method. A subsequent paper will investigate the emission-line galaxies' morphologies in a quantitative manner, including the results of the selection for the entire PEARS dataset in addition to these HUDF ELGs.

3.4.6. Line luminosities of PEARS galaxies: Comparison to nearby galaxies

From our sample, there are 33 Hα and 13 [O II] emission regions from galaxies at average redshifts of $z \sim 0.26$ and $z \sim 1.05$ respectively. Here we discuss the properties of these objects in terms of their line luminosities in comparison to local samples from Kennicutt et al. (1989) and Zaritsky et al. (1994). Figure 18 gives the luminosity histogram of PEARS HUDF Hα emitters (solid line) with the slope of the local HII region Hα distribution from Kennicutt et al. (1989) as a dot-dashed line. We have also plotted the best fit line of the bright end of our distribution with a dashed line. Here we see that the grism observations do not detect some of the fainter emission, as is expected; however, we do detect brighter sources, lending to the shallower slope. We note here that this effect is not due to spatial resolution: at $z \sim 0.3$, each pixel is ~ 130 parsecs, and Kennicutt et al. (1989) show that there is almost no difference in the luminosity histograms when degrading the spatial resolution from 30 to 300 parsecs.

When we investigate line luminosites of individual knots from the nearby Zaritsky et al. (1994) sample (Figure 19), we see two distinct distributions, with the high redshift PEARS [O II] emitters having systematically higher luminosities. A selection effect exists here, as we can only detect the brightest sources at high redshift (detection limit of $log(L([O\,ii])\mathrm{L}_{\odot}) \sim 6.3$ in Figure 15). The fact that we miss the lower luminosity [O II] emitters in this dataset does not negate the fact that we *do* see very high luminosity sources at this redshift in the grism data (see also discussion of high-EW [O II]sources in previous section).

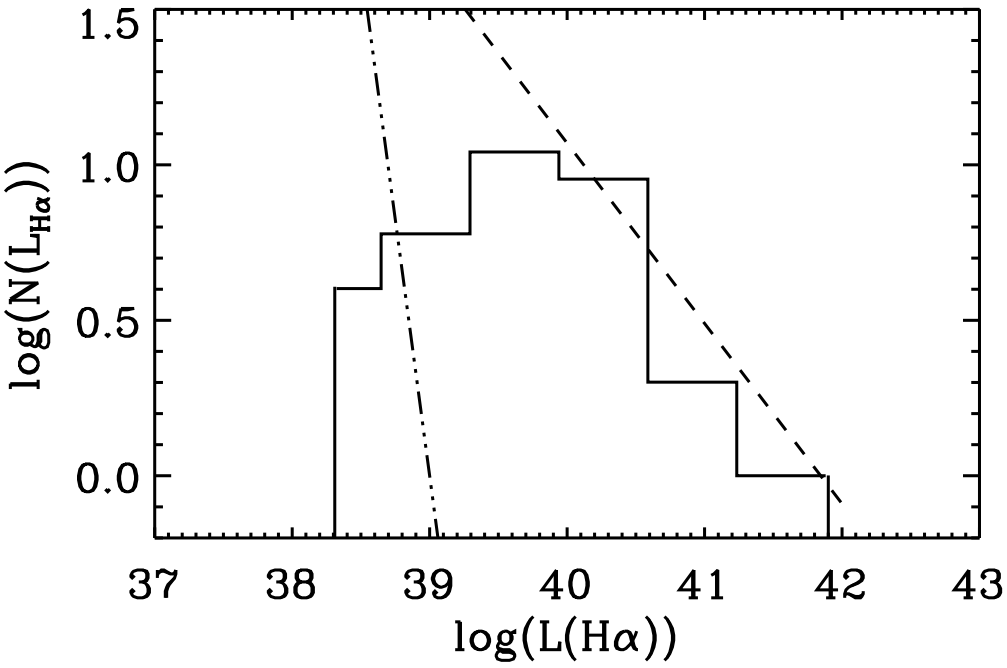

FIG. 18 Distribution of Hα line luminosities of the PEARS galaxies (median redshift of z$\sim$0.26), with the local Kennicutt et al. (1989) sample's bright-end slope plotted as a power-law (dot-dashed line; a=-3.3). The PEARS sample slope differs from the local one (a=-0.58); we detect more bright Hα emitting regions in the grism data.

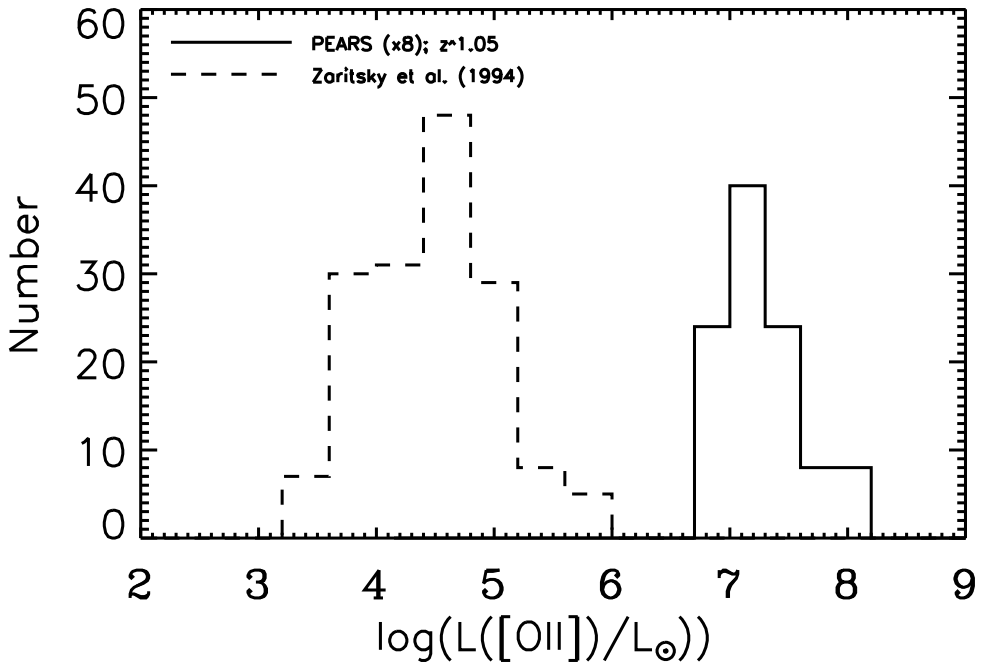

FIG. 19 Distribution of [O II] line luminosities of the PEARS galaxies (solid line multiplied by a factor of 8; median redshift of $< z > \sim 1.05$) and of HII regions within nearby galaxies from Zaritsky et al. (1994; dashed line). The grism observations are well-suited to detect high-redshift sources with very high [O II] luminosities. Note here our detection limit (shown in Figure 12).

3.4.7. Galaxies with multiple emitting knots

Individual HII regions in nearby galaxies have been studied for some time (Shields 1974; McCall, Rybski, & Shields 1985, Zaritsky, Kennicutt, & Huchra 1994, etc.), and it is well known that star formation properties vary in local galaxies from one star forming region to another. For example, Kennicutt, Edgar, & Hodge (1989) find that the luminosity function of HII regions in spiral arms and interarm regions differ greatly. Zaritsky, Kennicutt, & Huchra (1994) also find measurable differences in line luminosities of indivdidual star forming regions in nearby galaxies. Gordon et al. (2004) investigate in detail the variations of Hα (as well as UV and infrared) star formation rates in the many star-forming regions of M81. Additionally, star-forming clumps in the interacting system IC2163 & NGC2207 are studied by Elmegreen et al. (2006). However, investigation of individual emitting regions in high-redshift galaxies has not been explored as extensively. Studies of this kind focus on physical processes occuring within the galaxy, and comparisons of the high redshift sample to local galaxies help to sort out possible evolutionary effects. As noted above, 12 of our 63 2D-selected emission-line galaxies ($\sim$20%) have multiple emitting knots, many of which display multiple lines. These galaxies lie in the redshift range of $0.12 \lesssim z \lesssim 0.44$, the faintest of which has a continuum magnitude of $i'_{AB} = 23.64$ mag. Here we focus on several of these PEARS galaxies that have spatially distinct emitting knots.

PEARS Object # 75753/78237 (SExtractor extracted this object as two separate objects, but visual inspection shows that the two selected regions are part of the same galaxy) has six separate emitting regions, four of which have both Hα and

[O III] emission (one knot containing only [O III] emission). This object is shown in Figure 9. In the three knots (which are in 75753) that have both lines, the [O III] flux is approximately 2× the Hα flux (which indicates high excitation, which often means low metallicity). The other knot (in 78237) that has both lines has roughly equal flux in both Hα and [O III]. The Hα flux differs by a factor of up to ∼3.5, suggesting a variation in star formation rate across the complex structure of this galaxy. The knot indicated by the red circle in Figure 11 has an unidentified line with a wavelength inconsistent with the others present in this source and with no viable alternative line at this redshift (λ_{obs}=7872Å ;λ_{RF}=5875Å if the line originated from this galaxy). We also note that this object has a slightly different color than the rest of the nuclear region of the galaxy. Given these factors, we conclude that the "knot" within the red circle is an interloper at an undetermined redshift, whose emission line is present in the spectrum of Object 75753/78237.

PEARS Objects 70314 and 78491 each have three emitting knots (Figures 10 and 11 respectively). Object # 70314's three knots all have Hα emission, with two knots having roughly equal Hα flux and equivalent widths, and the other knot having lower flux and equivalent width values by a factor of ∼4. This galaxy is a good example of the success of the 2D line-finding method: the lines in this galaxy—with its multiple blue star-forming regions—were not detected with the 1D method in either the PEARS or GRAPES data, because the line flux was washed out by the continuum flux from the galaxy's core (see also Figure 12). Following this same line of reasoning, the weakest line of the three is the one originating from the nucleus

of the galaxy # 70314 (Figure 9). The lines stand out more when extracted solely from the emitting knots instead of the entire galaxy. All of the lines associated with Object # 78491 have equivalent widths $\gtrsim$100 Å (Table 1). Two of the knots contain both Hα and [O III], and originate from blue star-forming regions on the ends of the galaxy disk (Figure 11). The third "knot" associated with this PEARS ID appears to be another object and has a strong line ($EW = 237.0$ Å) that remains unidentified due to lack of redshift for this particular object (λ_{obs}=7143Å ;λ_{RF}=5788 for z=0.234, the redshift of Object # 78491) .

PEARS Objects 63307, 70407, 75547, 77558, 79283, 79483, 81944, and 88580 all have two emitting knots. The properties of these galaxies are given in Table 1. Object # 81944 has strong Hα and [O III] emission from one of its knots and a relatively weak Hα line in the other (with an equivalent width of $\sim$4.5 times lower). There are other cases (IDs 79283 and 88580, for example; $z = 0.23$ and $z = 0.269$ respectively) where line flux differs by a factor of 2 or more across a single galaxy. This indicates that the star formation properties of these objects differ across the galaxy itself, and that this effect in general can be probed at redshifts $z \gtrsim 0.2$.

We also note here that five of the twelve galaxies with multiple emitting knots did not have detected lines in the deeper GRAPES+1 ACS field data (described above; Sec. 4.4). Among the galaxies that were detected in GRAPES, the PEARS-detected lines' equivalent widths were higher in every case by on average a factor of$\sim 4\times$. This again underscores the strength of the 2D method, which serves to isolate line emission from individual knots, such that continuum emission from the rest of the galaxy does

not dominate the spectrum.

Given the subset of PEARS HUDF galaxies that exhibit multiple emitting knots, we expect to have a statistically significant sample of these objects once analysis of the entire PEARS dataset is completed. This should allow an in-depth study of localized star formation at galaxies up to $z \sim 0.4-0.5$.

3.5. Summary and Future Work

In summary, it is clear that although each method has some unique detections, Method 2D-B (triangulation) in general is quite efficient at detecting emission-line sources in the PEARS grism data, especially for objects with knotty structures or strong continuum that remain undetected with the 1D method. The reason for this advantage is that the 1D method gives line flux integrated over the whole galaxy, while the 2D method gives line flux from the emitting region only (i.e. galaxy knots). Triangulation requires observations obtained at multiple roll angle, and hence may not be suitable to all grism datasets. Method 2D-A (cross-correlation) can be used with ACS grism data obtained at one PA (Meurer et al. 2007), but is not fully automated and may produce false identification of emitting sources in confused regions such as in extended galaxies. The triangulation method will be utilized in future studies of the remaining eight PEARS fields. Given the sample of 81 distinct emitting regions, we expect a total sample of $\sim 600-700$ ELGs to continuum $i'_{AB} \lesssim 26.5$ mag from the combined depth and area of the PEARS North and South fields. From this larger statistical sample, two primary investigations will follow. First, we will derive line luminosities, which should allow us to constrain the luminosity function for Hα, [O II],

and [O III], going fainter and to higher redshifts than previous studies. Secondly, we will use the luminosities and equivalent widths to estimate the change in the cosmic star formation rate, again utilizing the depth and quantity of the PEARS data. In order to account for dust attenuation, we plan to estimate an average correction for the different redshift bins in the survey following previous authors. For example, Davoodi et al. (2007) calculated estimates for a sample of 1113 SDSS galaxies in the SWIRE survey (using the extinction law from Calzetti et al. (1994)). Kewly et al. (2004) used the redding curve of Cardelli, Clayton, & Mathis (1989). Additionally, Thompson et al. (2006) give examples of extinction and surface brightness dimming corrections to star formation rates for HUDF galaxies with redshifts 1-6. Pixel-to-pixel SED decompositions of HUDF galaxies are currently being performed by Ryan et al. (2008, in prep.) and will also provide estimates for the effects of dust over a large redshift range. In addition to these two primary goals, we will also investigate in further detail the possible evolution of [O II] equivalent width and luminosity with redshift (Figs. 16 & 19). The $z = 0 - 1.5$ range is where the SFR density shows its strongest evolution. Use of the grism to isolate the strongest EW sources in this redshift range, combined with deep HST imaging, will prove to be an excellent way to select galaxies that are most evolving over this important redshift range. We will then perform a detailed quantitative study of the morphologies of these objects, so as to diagnose what is causing the evolution. Simulations of the PEARS data (which are currently being performed) will allow us to gain a better insight into various selection effects and limits, and will aid in conclusions drawn from the dataset. These future studies should

provide a more detailed look at the overall nature of these line-emitting galaxies, thus revealing mechanisms of star forming activity over $z = 0 - 1.5$.

4. ELGS FROM THE HST PEARS GRISM SURVEY I: THE SOUTH FIELDS

We present results of a search for emission-line galaxies in the South Fields of the Hubble Space Telescope PEARS (Probing Evolution And Reionization Spectroscopically) grism survey. The PEARS South Fields consist of five ACS pointings (including the Hubble Ultra Deep Field) with the G800L grism for a total of 120 orbits, thus revealing thousands of faint object spectra in the GOODS-South region of the sky, many being emission-line galaxies (ELGs). Using a 2-dimensional detection and extraction procedure, we find 320 emission lines orginating from 230 galaxy "knots" within 203 individual galaxies. Line identification results in 118 new spectroscopic redshifts for galaxies in the GOODS-South Field. Including the Hβ emission line (which is blended with [O III] in our data) in our line fits provides a means by which to estimate excitation, and we find that the PEARS ELGs which have both lines identified are generally high–excitation, high–luminosity sources as compared to, e.g., SDSS AGN samples. The star-formation rates of ELGs are presented, and we show that we can detect differences in star formation in distinct HII regions at z$\sim$0.1-0.5 across individual galaxies. We find that the radial distances of PEARS spiral galaxies' HII regions at redshifts z$\sim$0.1-0.5 in general reside near the galaxies' half–light radii, similar to those of giant HII regions in local galaxies.

4.1. Introduction: ELGs in the PEARS South Fields

The Probing Evolution And Reionization Spectroscopically (PEARS [2] grism survey provides a 200 HST orbit dataset from which to investigate many different aspects of galaxy evolution: from high-redshift objects (Lyα, Lyman break galaxies and AGN (Rhoads et al. 2008, submitted; and Grogin et al. 2008, in prep. respec-

[2] http://archive.stsci.edu/prepds/pears

tively)) to spiral bulges (Hathi et al. 2008) and ellipticals, to emission-line galaxies (ELGs; Straughn et al. 2008). Additionally, studies of objects in the nearby universe are also possible (Pirzkal et al. 2008, submitted, investigates stars in the PEARS Fields). A similar deep grism program was carried out in the GRAPES project (Pirzkal et al. 2004, Xu et al. 2007, Rhoads et al. 2008). Here we discuss results of a search for ELGs in the PEARS South Fields; in particular, we present new grism spectroscopic redshifts for 118 galaxies in the GOODS South Field as well as discuss ELG line luminosities, star-formation rates, and AGN candidates among the sample.

For many years, galaxies that are actively forming stars have been regarded as important sources to study in the context of galaxy evolution. In particular, the Hα, [O III], and [O II] lines have been used extensively to determine SFRs (Kennicutt 1983; Gallego et al. 1995; Gallego et al. 2002; Brinchmann et al. 2004; Villar et al. 2007; Westra & Jones 2007; Kewley et al. 2004; Glazebrook et al. 2004; Hanish et al. 2006). Many projects have specifically utilized slitless spectroscopy in order to study ELGs. Ground-based slitless spectroscopy has been used by Kurk et al. (2004) to identify ELGs. Yan et al. (1999) derived the Hα luminosity function and SFR using the HST NICMOS G141L grism (from the NICMOS Grism Parallel Survey; McCarthy et al. (1999)). Teplitz et al. (2003) studied ELGs using the STIS Parallel Survey (Gardner et al. 1998). Drozdovsky et al. (2005) present ELGs from the HST ACS Grism Parallel Survey. Shim et al. (2008) have also studied the luminosity function and evolution of the SFR density for ELGs using Hα, also with the NICMOS Grism Parallel Survey data. The GRism ACS Program for Extragalactic

Science (GRAPES; Pirzkal et al. 2004, Malhotra et al. 2005) has also yielded slitless spectroscopy for galaxies in the Hubble Ultra Deep Field (HUDF), including a large sample of ELGs (Pirzkal et al. 2006; Xu et al. 2007). PEARS is a follow-up grism survey to GRAPES, and provides an even larger spectroscopic dataset of ELGs owing to its 8× greater area. In Straughn et al. (2008) we investigated in detail several methods aimed at detecting these ELGs in the PEARS HUDF pointing. Here we utilize the most efficient method and extend that study to include the remaining four PEARS South ACS Fields. In Section 2 we discuss the PEARS dataset used here; Section 3 outlines the methods used to detect the ELGs; in Section 4 we present results of the search, including a table of South Field ELGs detected along with new spectroscopic redshifts and a discussion of line luminosities, star-formation rates, AGN candidates, and radial distribution of galaxy knots; in Section 5 we summarize our findings and discuss future prospects.

4.2. Data

The HST PEARS grism survey consists of nine ACS Fields observed with the G800L grism. The G800L grism yields low-resolution ($R \sim 100$) optical spectroscopy between 6000-9500Å. Five fields were observed in the GOODS South region (including the Hubble Ultra Deep Field) and four in GOODS North. Here we present properties of ELGs detected in the PEARS South fields. The PEARS HUDF was observed for 40 orbits (four roll angles; limiting AB magnitude $i'_{AB} \lesssim 27.5$ mag); the other four South PEARS fields for 20 orbits each (three roll angles per field; limiting AB magnitude $i'_{AB} \lesssim 26.5$ mag). Multiple roll angles are observed in each field in order to

reduce the contamination of overlapping spectra in crowded regions. These multiple roll angles are also utilized in detecting viable emission-line sources, as described in the following section. Malhotra et al. (2008, in prep.) will describe the grism observations in detail. Pirzkal et al. (2004) gives a detailed description of the closely-related GRAPES project.

4.3. Methods

Here we briefly outline the procedures used to detect ELGs in the PEARS grism data, using a 2D detection method that takes advantage of the observation that emission lines typically originate from clumpy knots of star formation within galaxies. For a detailed description and comparison of several different extraction methods, see Straughn et al. (2008).

4.3.1. Data Pre-Processing

The first step required involves pre-processing of the grism data. Each grism image is median filtered and smoothed using a 13 x 3 smoothing kernel along the direction of the dispersion axis (i.e. unsharp-masked; see also Meurer et al. (2007) for a full description of this method of pre-processing ACS grism data in general). This step is performed in order to essentially remove continuum flux from the dispersed image, leaving behind mostly compact emission line features; as well as occasional residual image defects, which are unique to each roll angle and thus excluded in the next steps as described below. In doing this, we isolate the actual emission line which would ordinarily be washed out in the continuum, and therefore missed in more traditional 1D detection methods (see Figure 20). After the images are pre-processed

in this manner, they are catalogued with SExtractor (Bertin & Arnouts 1996), giving a list of compact sources.

4.3.2. Emission Line Detection by Triangulation

The basis of this method of emission-line detection and wavelength calibration relies on each source being observed in more than one roll angle. The emitting source is mapped back along the dispersion direction for each roll angle, and intersections of these mappings result in obtaining the real sky coordinates in RA, Dec, as well as the wavelength solution for that emitting source. In this way, image defects are excluded from the selection as they would not ordinarily appear at the same physical location on the grism images and map onto a "source" as described here. This procedure is applied to roll angle pairs, such that each source (that has three position angles observed, for example) has three calculations made (i.e. PA1-PA2, PA1-PA3, PA2-PA3; the HUDF, which has four position angles observed, thus has eight calculations per source). This procedure produces the master catalog of ELG sources, which are then visually checked. In the visual confirmation step, there are occasional instances where a line candidate was present in all three roll angles, and thus was included in the master catalog, but is not a genuine emission line. Such is the case for some bright galaxies that, despite the unsharp-masking, do not have sufficient continuum flux removed and thus have continuum "bumps" that appear in the grism image as compact sources: i.e., line candidates. When examining the collapsed 1D spectra (from the individual sources), it is clear which sources are genuine emission lines and which are not; the real lines are retained for each field. Here we distinguish

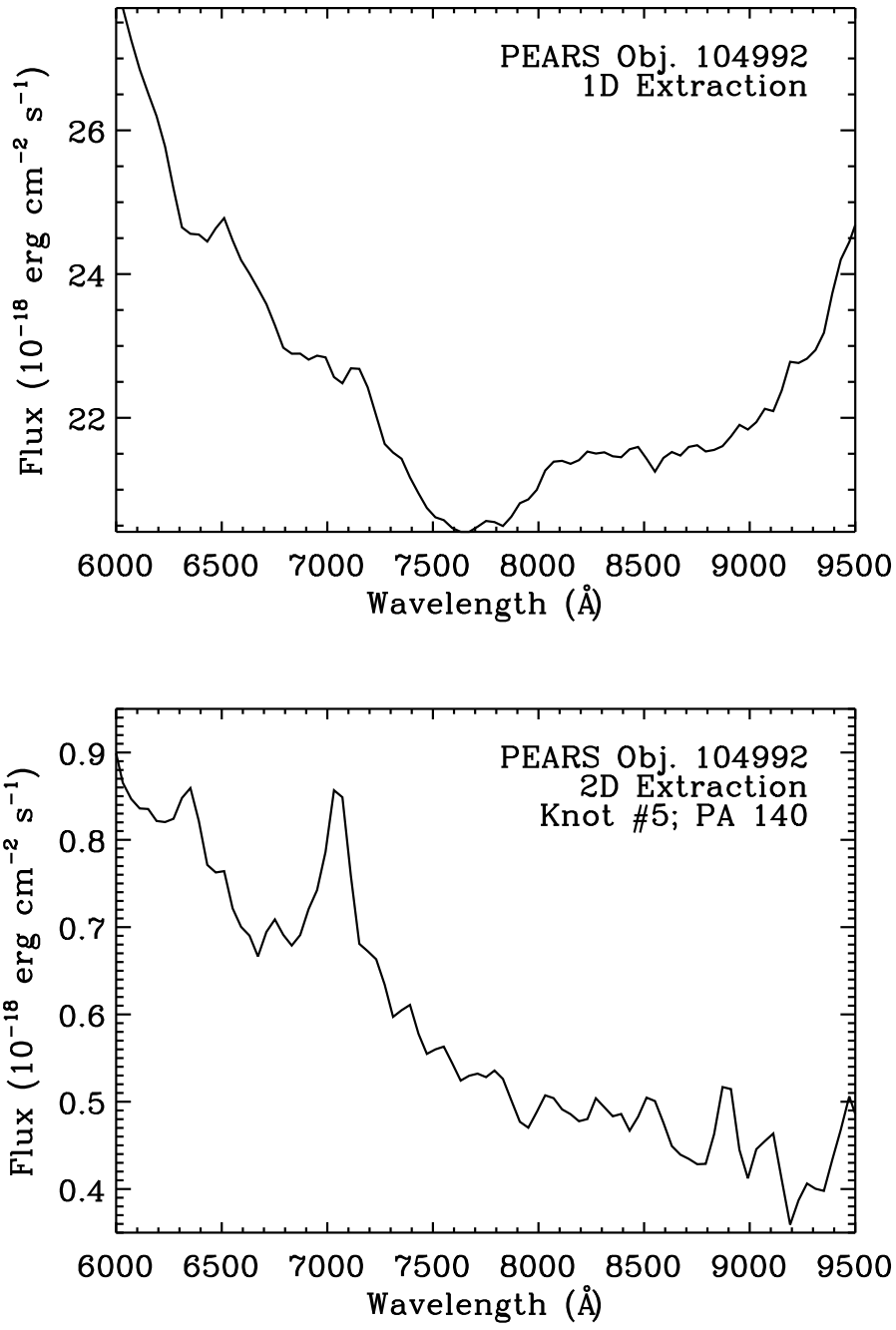

FIG. 20 Here we demonstrate the advantage of the 2D detection method outlined here (and described in detail in Straughn et al. 2008) for PEARS Object 104992 (see Figure). The emission line at (observed-frame) 7000Å is clearly seen when extraction of an individual knot is performed; however, continuum flux overwhelms the line when the spectrum of the entire galaxy is extracted (as would be detected in 1D methods; see Xu et al. 2007). See Figure for an image of this object.

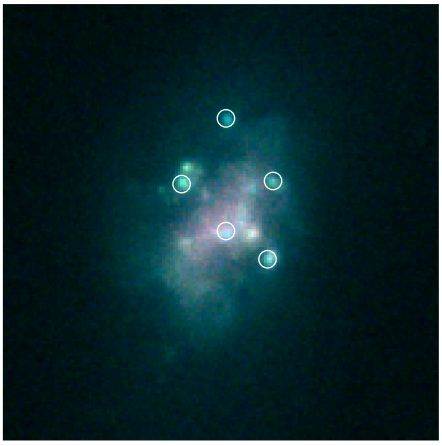

FIG. 21 PEARS Object 104992, displaying multiple knots where emission was above our detection threshold. 26 of the 203 galaxies in our sample have multiple emitting knots, many of which would not have been identified using 1D-detection techniques (see, e.g., Figure 20).

terminology, since extractions were performed on individual galaxy "knots"; therefore, a galaxy can have several knots, each of which can have more than one line. This method produced a total of 320 lines originating from 230 galaxy knots, within 203 individual galaxies in the five total PEARS South Fields.

4.3.3. Redshifts and Line Fluxes of ELGs

For ELGs with only one emission line (which is the case for 73% of our sample), a first-guess redshift is essential for line identification. Here we utilize the spectroscopic and photometric redshifts from the GOODS-MUSIC catalog (Grazian et al. 2006 and references therein). 30.7% of ELGs detected in the PEARS South Fields have spectroscopic redshifts and 80.5% have photometric redshifts (there is almost complete overlap between the two catalogs: less than 1% of sources have spectroscopic redshifts but no photometric redshifts). Where no spectroscopic or photometric redshift exists for a particular source, we match our sources against the table of spectro-photometric redshifts of Cohen et al. (2008, in prep.). Spectra with

strong lines, however, are often assigned artificially high spectro-photometric redshifts due to the presence of such lines that are absent from the template SEDs used. In total, there were 21 galaxies that had only a spectro-photometric redshift (some of which had double lines); of these, 6 had redshifts in concordance with the observed line and were used to deduce final identification. For the 30 objects where either the photometric or spectro-photometric redshifts do not agree with any of the likely line identifications, no redshift was assigned.

For galaxy knots that have two lines, the ratio of the observed line wavelengths is computed to obtain direct identification (i.e., without need of a first-guess redshift). For galaxy knots with only a single line, in order of preference, we used spectroscopic, photometric, or spectr-photometric redshifts for our first–guess redshifts (as described above) to arrive at line identifications within the redshift and instrinsic grism errors. Redshifts based on these identifications are subsequently recalculated.

Line fluxes are derived using standard Gaussian fitting techniques. Since the [O III] line—which is usually the strongest of the lines we detect—is blended with Hβ due to the grism resolution, we fitted two gaussian components, the central wavelengths of which are constrained to have the correct ratio. For 67% of the spectra in which we detect an [O III] line, the χ^2 improves when including the Hβ line in our fit. Of these, 23% of Hβ lines had $S/N > 3$ and were thus included in the final catalog. In utilizing this [O III] + Hβ fitting technique, we arrive at 90 improved [O III] fluxes (compared to fitting the [O III] line alone) and 30 Hβ fluxes.

4.4. Results

In Table 1 we list the emission–line wavelengths, line IDs, fluxes, and grism redshifts for 320 lines originating from 230 star–forming knots within 203 individual galaxies found in our search for ELGs in the PEARS South Fields. Figure 2 shows a representative sample of the ELGs discovered. Of these, 26 galaxies (13%) exhibit multiple emitting knots, and 61 knots (27.0%) have two lines (thus providing secure redshifts; see Methods section). Our sample includes 136 [O III], 83 Hα, 30 [O II], 30 Hβ, 4 C IV, 3 C III], 2 MgII, 1 Hγ, and 1 NeIII lines (see Table 3). 17 of these galaxies are CDF-S X-ray sources (Giacconi et al. 2001; Grogin et al. 2008, in prep.). The most common lines (Hα, [O III], and [O II]) are available in the redshift ranges of 0–0.4, 0.1–1.1, and 0.4–1.5 respectively, given the grism band–pass. The [O III] emitters have, in general, very high equivalent widths, with the average $EW_{[OIII]} = 152\AA$ at an average redshift of z$\sim$0.514.

Figure 23 shows the i'_{AB}-band continuum magnitude distribution of the 203 ELGs in the PEARS South fields. Our distribution of continuum magnitudes peaks around i'_{AB} =24 mag. The 2D method described here is optimized to find distinct emitting knots that often are present in relatively bright galaxies (here, for example, face-on spirals with large star-forming regions)—these generally make up the bright-end of the magnitude distribution shown here. The fainter tail of the magnitude distribution, by contrast, is comprised mainly of high-redshift compact objects, of which several are several are CDF-S X-ray sources that display the typical AGN C III] and C IV lines (as also confirmed by Grogin et al. 2008, in preparation). The distribution of emission–line fluxes for all 320 emission lines, regardless of species,

is shown in Figure 24. Figure 25 shows that distribution for each of the three most common emission–lines in our sample: Hα , [O II], and [O III]. The distributions for the emission–lines peak at $\sim$2.5$\times10^{-17}$ ergs cm^{-2} s^{-1} for Hα and [O III], and $\sim$1.0$\times10^{-17}$ ergs cm^{-2} s^{-1} for [O II]. The flux limit for the sample is $\sim$3.6$\times10^{-18}$ ergs cm^{-2} s^{-1}.

Given the grism resolution, contamination of the dominant lines by other nearby, unresolved lines is almost certainly present. For example, the Hα line flux measurements will contain some contribution from the [NII] $\lambda\lambda$6548,6584 lines. The magnitude of this contamination will differ for different galaxies, as it depends on effective temperature, ionization, and metallicity. Helmholt et al. (2004) derive an [NII] correction for a sample of local late-type dwarf disks; this was used with the SINGG sample of galaxies (Meurer et al. 2006). Other grism surveys of ELGs have used global corrections by Gallego et al. (1997), which also was derived based on a local galaxy sample. Our detection method, however, serves to produce (as described in Sec. 3) individual galaxy knots in a wide array of morphological types, and thus a global adoption of any one [NII] contamination correction is not straightforward. Thus, measured Hα fluxes are likely overestimates due to this contamination but we do not adopt a global correction. The amount of contamination can range from a few percent for, e.g., Blue Dwarfs (which have unusually high ionization and low metallicity) to the factors of 0.3 and 0.5 assigned by Gallego et al. (1997) and Kennicutt (1992) respectively (however, the latter being for massive, metal–rich galaxies). The signal-to-noise (S/N) distribution of line fluxes is shown in Figure 26. The average S/N for the sample is 11.8; this average increases to 12.6 when the generally weaker,

blended Hβ line measurements are excluded. Our detection methods outlined above serve to produce a final sample of high-confidence detections.

The presence of dust affects our measurements, and thus the calculations of, e.g., the star–formation rate (Section 4.4.3) should be considered lower limits as no extinction correction was applied. The Hβ flux in principle allows an estimation of extinction for the cases in which both Hβ and Hα fall into the wavelength range of the grism. This is only possible for a small percentage of objects and thus we do not derive a global correction based on only these few sources. Both Hα and Hβ are in the spectra of five PEARS–South objects (38750, 40816, 75753, 78582, and 123859), and so we can investigate the reddening in these five individual sources. The reddening using only the Balmer decrement and the Milky Way or LMC extinction law from Seaton (1979) (e.g., Calzetti et al. 1994, who find an average E(B-V) of 0.4 for starburst galaxies) gives E(B-V) values of 0.6, 1.6, 0.3, 0.8, 0.5 respectively for these five PEARS-South sources. Visual examination of these sources reveals one particularly red/dusty object (40816—with the highest E(B-V)) which is also an X-ray source and classified as an AGN by Grogin et al. (in preparation).

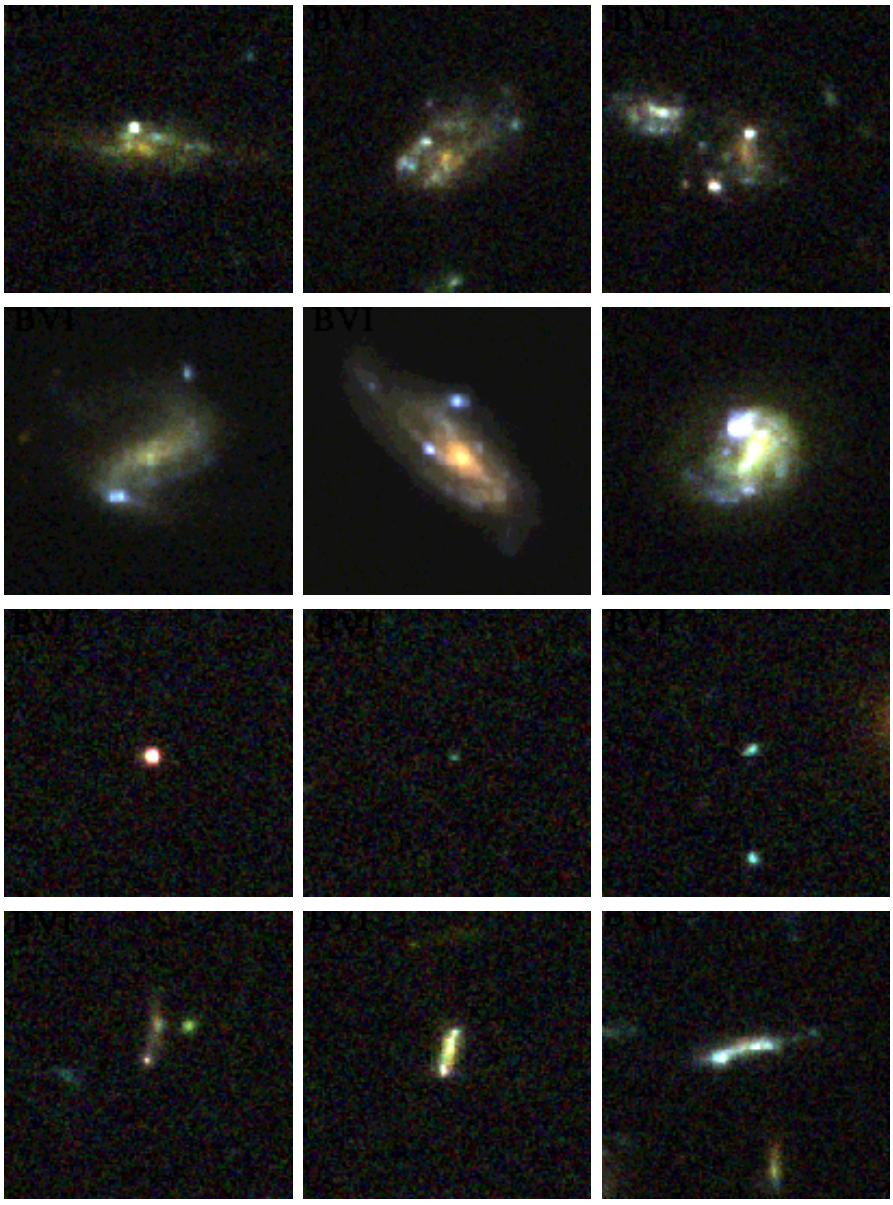

FIG. 22 Here we show examples of emission-line galaxies detected with our 2D method. Stamps are from GOODS imaging and are 5 arcsec^2.

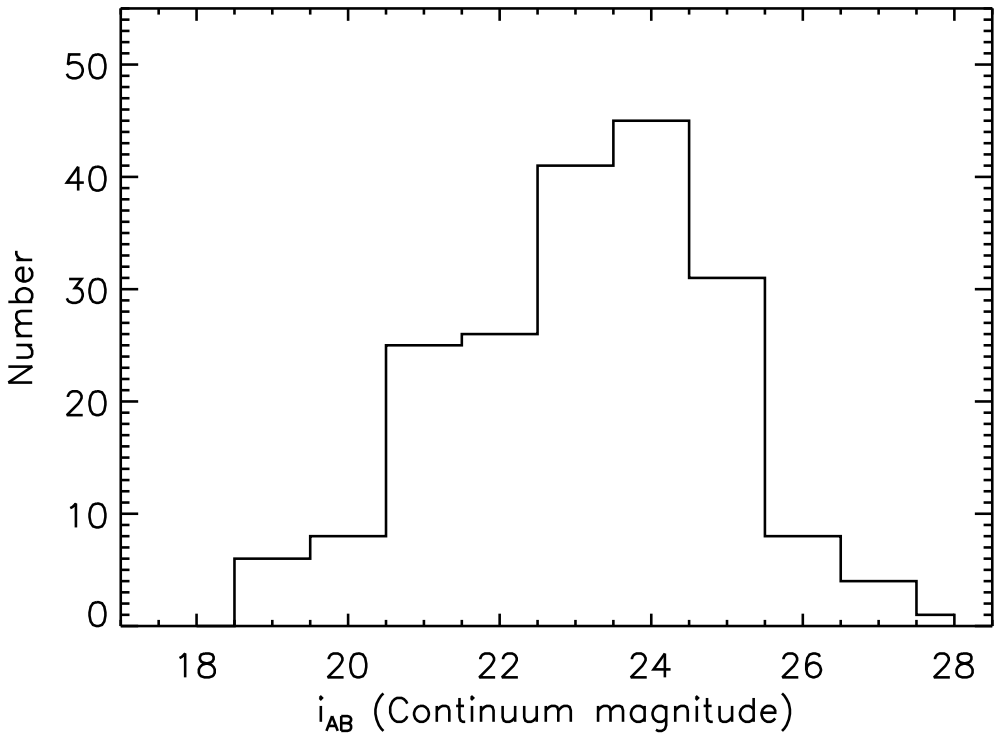

FIG. 23 The continuum magnitude distribution of ELGs peaks around $i_{AB} = 24$ mag. The clumpy face-on spirals make up the bright end of the magnitude distribution, with high-redshift sources—some being AGN—mostly comprising the faint end.

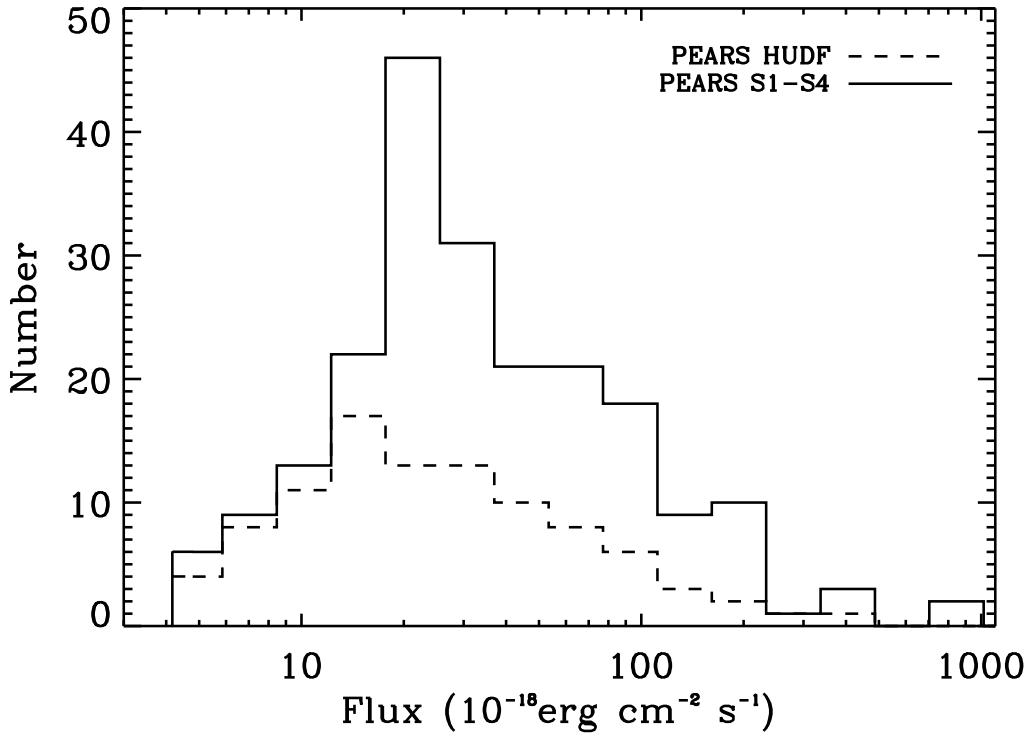

FIG. 24 The ELG line flux distribution peaks at $\sim$2.5$\times$ 10^{-17} ergs cm^{-2} s^{-1}; the flux limit is (fix)$\times$ 10^{-18} ergs cm^{-2} s^{-1}. [sep. hists. for hudf and rest of pears]

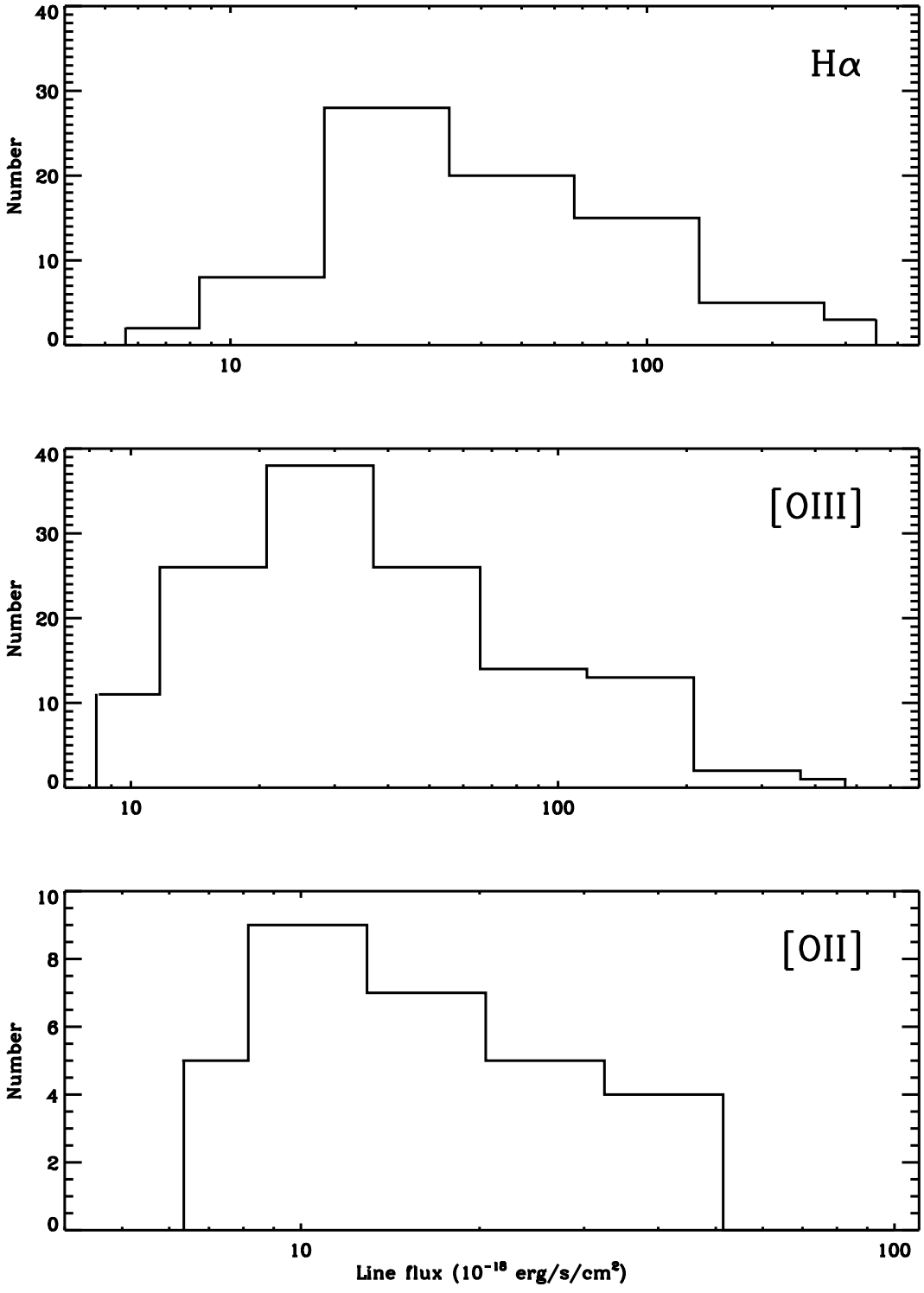

FIG. 25 Each different emission line flux distribution peaks at a different value; those being $\sim 2.5\times 10^{-17}$ ergs cm^{-2} s^{-1}, $\sim 3.0\times 10^{-17}$ ergs cm^{-2} s^{-1}, and $\sim 1.0\times 10^{-17}$ ergs cm^{-2} s^{-1}for Hα , [O III], and [O II] respectively.

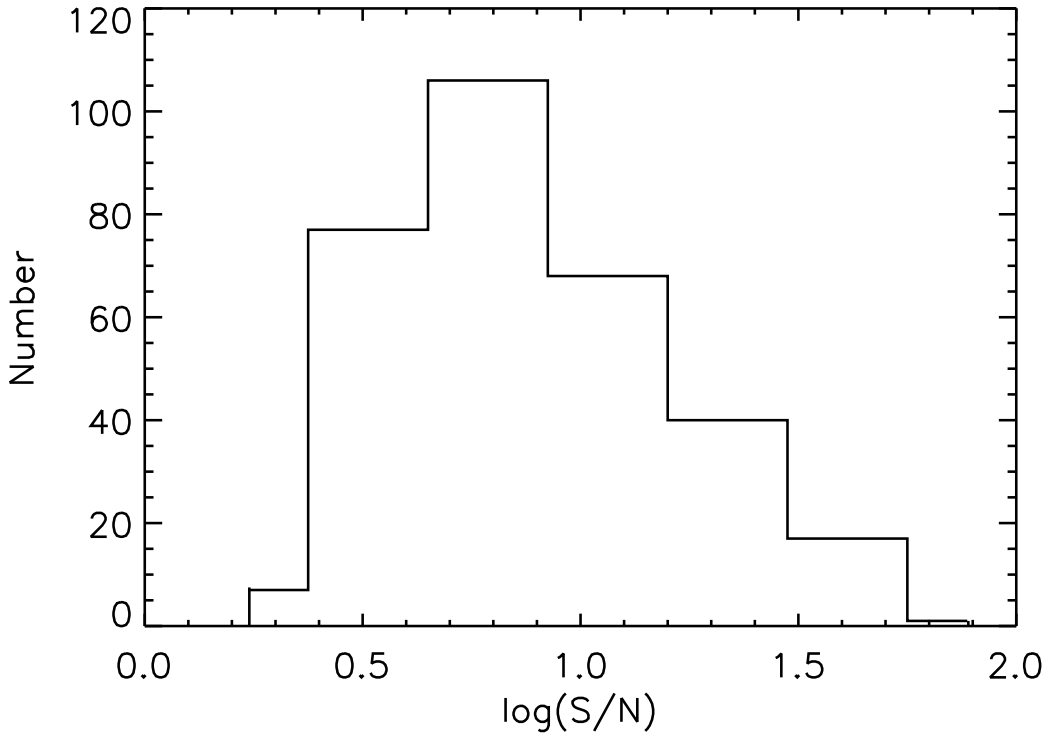

FIG. 26 Distribution of signal-to-noise for all derived line fluxes. The average S/N for the sample is 11.8; this average increases to S/N=12.3 when the weaker, blended Hβ lines are excluded. Our detection method requires a relatively high S/N because the initial grism detection images are smoothed before source extraction is performed; this is the reason we miss, e.g., lower S/N Lyα emitters (see Rhoads et al. 2008, submitted).

4.4.1. Grism Redshifts

Of the 203 emission-line galaxies, 118 have new grism spectroscopic redshifts based on our line identifications. We find 11 galaxies (Table 1) that previously had no reported redshift at all (photometric, spectroscopic, or spectro-photometric) and that have two lines, allowing determination of a grism redshift from the wavelength ratios. The redshift distribution of the sample is given in Figure 27. The redshift distribution peaks at z$\sim$0.5 and is determined by the most common emission–lines within the grism bandpass: [O III], Hα , and [O II]. This explains the lower redshift peak compared to that of the general galaxy population. The few high–redshift objects in this plot are the more rare C III], C IV, and MgII emitters. All of these high-redshift sources in the CDF-S are confirmed by the X-ray observations, and are thus likely AGN (Grogin et al. 2008, in prep.). The CDF-S X-ray sources are noted in Table 1.

In Figure 28 and Figure 29 we show comparisons of our calculated grism redshifts to the available photometric and spectroscopic redshifts for the ELGs. As mentioned, for sources with only a single line, any previously available redshift was used to initially identify the line in the cases where the line falls within the redshift (and inherent grism) errors. These comparisons are investigated to address redshift and wavelength accuracy of the PEARS grism data using sources that had a previously-measured redshift, especially those that have two emission lines (and thus a more secure line identification and grism redshift). Comparison to spectroscopic redshifts essentially serves to demonstrate the wavelength accuracy of the grism, which is

shown in Figure 28. The dispersion about the mean is 0.005 and two objects are $\gtrsim 3\sigma$ outliers (PEARS Objects 72509 and 17362, both of which are single-line detections with relatively low $S/N < 3$ and likely represent wavelength calibration issues). As expected, the dispersion in the photometric/grism redshifts is greater at 0.06, with the greatest Δz being 0.585 (PEARS Object 52502; the only 3σ outlier). This object has two emission lines with S/N>5, thus providing a secure grism redshift based on the wavelength ratio. Object 20201, which was only marginally within 3σ of the photometric redshift also has two high S/N emission lines, as well as a clear Hβ "bump" in the [O III] line profile, further confirming its identification; see Figure 30). Thus for these two outlying objects, we are confident that the grism redshift calculated here is correct.

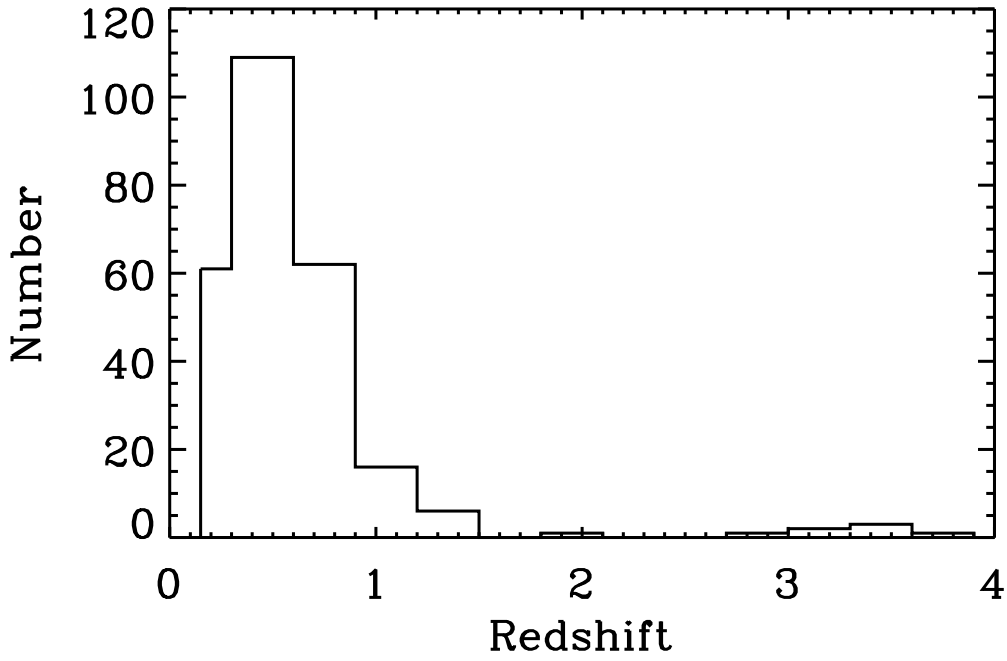

FIG. 27 The G800L grism is sensitive from 6000-9500 Å, which yields the most common emssion lines—Hα, [O III], and [O II] in the wavelength ranges of z=0–0.4, 0.1–1.1, and 0.4–1.5 respectively. The [O III] line is the most common, and thus the peak is near z$\sim$0.5. The higher redshift objects are the more rare C III], C IV, and MgII emitters.

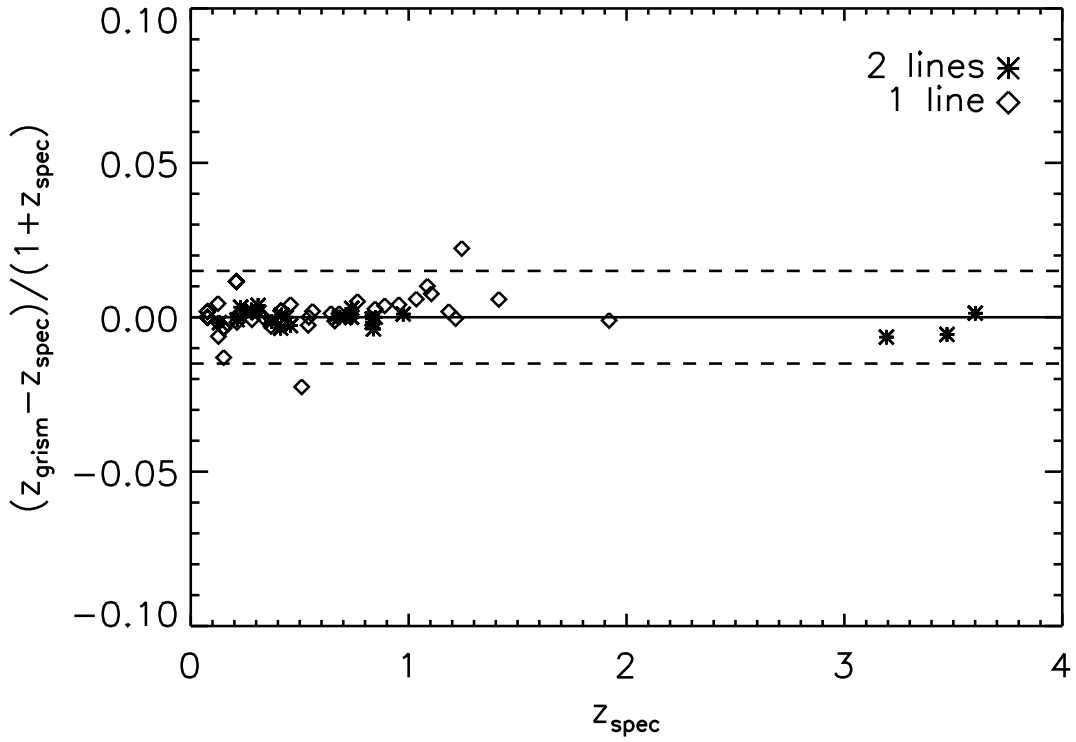

FIG. 28 Comparison of available spectroscopic redshifts to grism redshifts measured in this study, with 3σ lines shown. 30.7% of PEARS-South ELGs have previously-measured spectroscopic redshifts. Comparison of grism to spectroscopic redshifts essentially serves to demonstrate the wavelength/redshift calibration accuracy of the PEARS grism data.

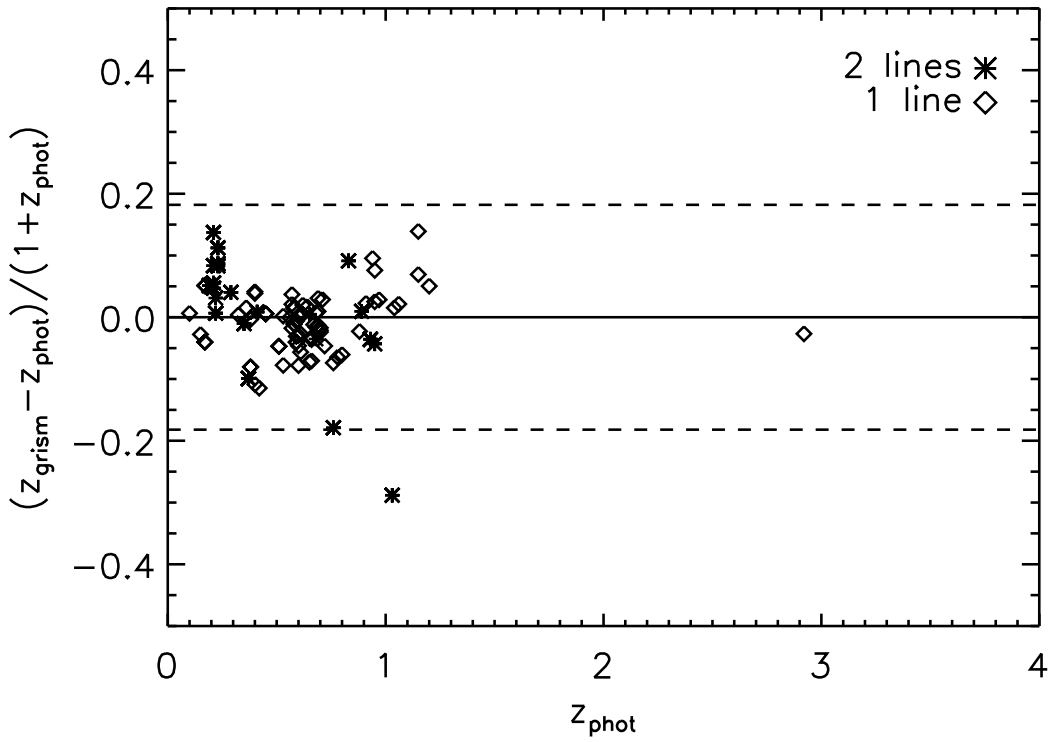

FIG. 29 Comparisons of available photometric redshifts to grism redshifts calculated in this study, with 3σ lines shown. 80.5% of PEARS-South ELGs have previously-measured photometric redshifts, and here we show the comparisons of these photometric redshifts to grism redshifts. See Section 4 for a discussion on outliers.

4.4.2. Line Luminosities of the ELGs

Table 1 lists the line luminosities for the objects in our sample. The median Hα line luminosity is 8.3×10^{39} ergs s^{-1} (whereas the faintest is 2.5×10^{38} ergs s^{-1}). As a comparison, Drozdovsky et al. (2005) find a median Hα line luminosity of 2.7×10^{40} ergs s^{-1} from the ACS Grism Parallel Survey. The typical local L^*(Hα)=7.1×10^{41} ergs s^{-1} (Gallego et al. 1995) and is L^*(Hα)=3.6×10^{42} ergs s^{-1} at z=1.3 (Yan et al. 1999). Our median [O III] line luminosity is 2.8×10^{40} ergs s^{-1} and 6.7×10^{40} ergs s^{-1} for [O II].

96% of our emitting regions have L$\gtrsim10^{39}$ ergs s^{-1}. These potential "giant" or

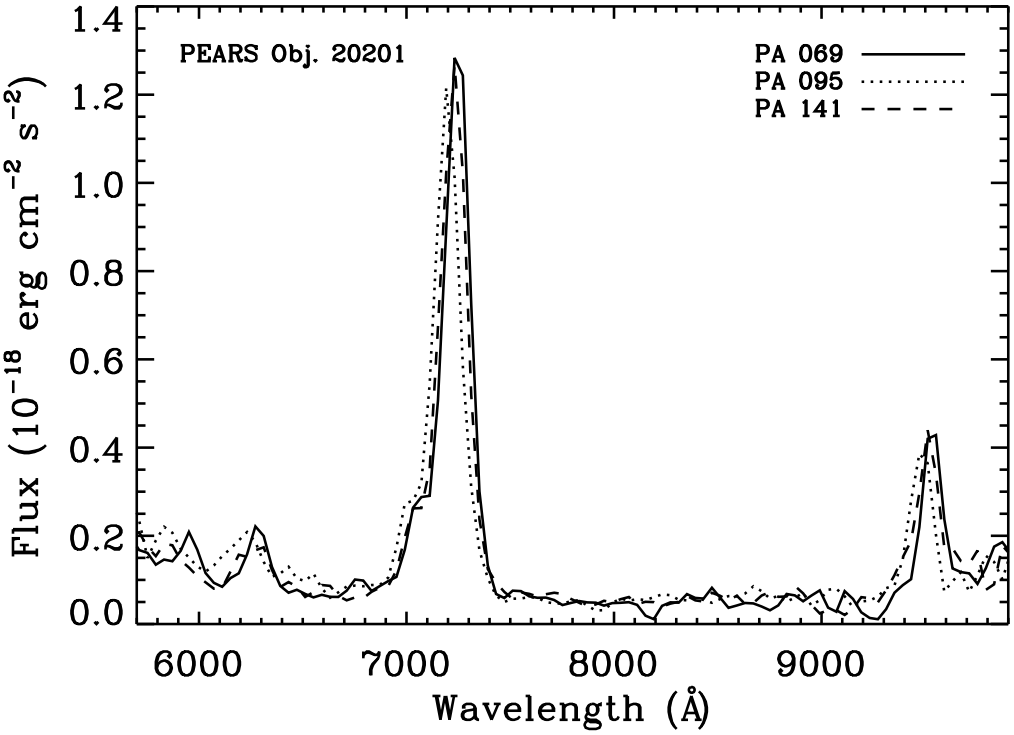

FIG. 30 Shown here is an example spectrum from PEARS Object 20201, at a redshift of z=0.445, exhibiting the blending of Hβ and [O III]˙Hα is also visible near the red end of the spectrum. An Hβ "bump" (near 7000Å) is clearly seen, though not resolved from the stronger [O III] blend. In total, 31 galaxy spectra had better χ^2 fits when the Hβ line was included. Hγ is also detected here, with marginal Hδ.

"supergiant" HII regions (Kennicutt et al. 1989) in galaxies at z$\sim$1 likely represent the majority of the galaxies' current massive star formation and thus can be treated as representative of *global* star formation in these galaxies (Kennicutt et al. 1989). fainter than L$\sim10^{39}$ ergs s^{-1} are in general spirals with distinct, but relatively smaller, star-forming knots.

4.4.3. Star-formation Rates of ELGs

We present the star-formation rate (SFR) as a function of redshift of our ELG sample in Figure 31. SFRs are calculated using the calibrations of Kennicutt (1998) for Hα and [O II], respectively:

$SFR_{\mathrm{H}\alpha}$ ($M_\odot$ yr^{-1})=7.9$\times10^{-42}$ L(Hα) (erg s^{-1})

$SFR_{[OII]}$ ($M_\odot$ yr^{-1})=1.4$\times10^{-41}$ L([OII]) (erg s^{-1})

for solar abundances and a Salpeter IMF for 0.1-100 $M_\odot$. Hα is considered to be the most direct probe of massive star formation, and thus is the most secure line in determining SFRs. The SFR based on [O II] line luminosity is less secure, as differences in metallicity and other local environmental properties play a larger role in the oxygen lines (Kewley et al. 2001; Jansen et al. 2001; Kewley et al. 2004). However, the [O II] line is still calibrated well enough to deduce SFRs for galaxies at higher redshift (Cowie et al. 1996, Kennicutt 1992, Gallagher et al. 1989). We use the Kennicutt (1998) calibrations for the Hα and [O II] emitters in the PEARS-South ELG sample presented here.

The determination of SFR from [O III] line luminosities is not as straightforward, since the [O III] flux depends quite strongly on metallicity and gas temperature

(Kennicutt et al. 2000, Kennicutt 1992). With the ACS G800L grism resolution, the [O III]$\lambda\lambda$4959,5007 doublet and Hβ are blended, and while our fitting technique does fit the blended [O III]+ Hβ feature, some cross-contamination of the lines is likely. The majority of our galaxy knots that contain [O III] emission also have Hα emission ($\sim$61%), so in these cases, it is clearly best to use the more direct Hα SFR. Here we note that for the sources that contain both Hα and [O III] lines, the flux ratio of Hα to [O III] > 1 suggests that there is little reddening and that the gas ionization is mostly due to early O-type stars, which confirms that we are detecting episodes of ongoing star formation. Although the majority of galaxy knots that contain [O III] also contain Hα, there are still emitting regions in which only an [O III] line was detected due to the Hα line falling out of the grism range, and for these we derive the [O III] SFR by using the [O III]:Hα ratio from the galaxy knots that do have both emitting lines. We thus arrive at:

$SFR_{[OIII]}$ ($M_{\odot}$ yr^{-1})=1.3$\times$10^{-41} L([OIII]) (erg s^{-1})

The possible presence of residual Hβ flux as described above adds an additional source of error to the derivation. However, in all cases, we have not applied extinction corrections and thus the SFRs presented here are in general lower limits. Additionally, we assume that most of the galaxies' active star-formation is occurring in these supergiant knots, but note that the sample is incomplete in the sense that only the brightest knots of the galaxies are detected and diffuse emission is missed in our method. Figure 31 shows the expected bias of higher SFRs at higher redshift, and in general follows calculations performed in similar studies (e.g., Drozdovsky

et al. 2005).

Figure 31 displays the expected trend of star formation with absolute magnitude (in this case for [O II] emitters): more luminous galaxies exhibit higher SFRs. In this figure, the two faintest objects (PEARS Objects 78021 and 85844 at $M_B = -16.7$ and -18.3 and redshifts z=1.311 and 1.299 respectively) with comparatively high SFR have compact morphology, but are not CDF-S X-ray sources.

4.4.4. AGN Candidates in PEARS–South

Adjusting our fitting algorithm to include Hβ fits allows us to gain a crude estimate of excitation; in Figure 32, we show the [O III]:Hβ line ratio compared to a large sample of SDSS AGN. In this study, Kauffmann et al. (2003) compare this line ratio to [NII]λ6583/Hα and thus define a region of likely Seyferts and LINERs (as compared to starburst galaxies) in a BPT diagram (Baldwin et al. 1981). In the grism data, the [NII] line is blended with Hα (and is not possible to deblend, as is the case with some objects for [O III] and Hβ) and thus a BPT diagram is not possible with the PEARS ELGs. However, regular (non–AGN) starburst galaxies with [O III]:H$\beta \gtrsim$8 (taking into account the blending of the [O III] doublet) are extremely rare, and we thus conclude that the PEARS objects that lie above this threshhold are probable AGN (while objects having [O III]:H$\beta \gtrsim$13 are likely Seyferts). We matched the sample of objects with both [O III] and Hβ lines to the PEARS AGN sample of Grogin et al. (in preparation) and found two overlapping objects (i.e., CDF-S X-ray sources displaying [O III] lines). One of these two objects, PEARS Object 40816, has F([O III])/F(Hβ)=12.6; the other, PEARS Object 78982, has F([O III])/F(Hβ)=3.2.

As Figure 32 demonstrates, the PEARS AGN candidates (based on the [O III]:Hβ ratio) reside mainly on the upper right locus in the SDSS AGN sample. The lack of objects with lower excitation is likely a result of the de–blending of the [O III] and Hβ lines: in all cases where it was possible to include Hβ in the line fits (and where such inclusion resulted in improved fits), the Hβ line was significantly weaker (by a factor of at least 3). We thus conclude that including Hβ in the line fitting procedure when possible provides a way in which to select probable AGN from the grism data.

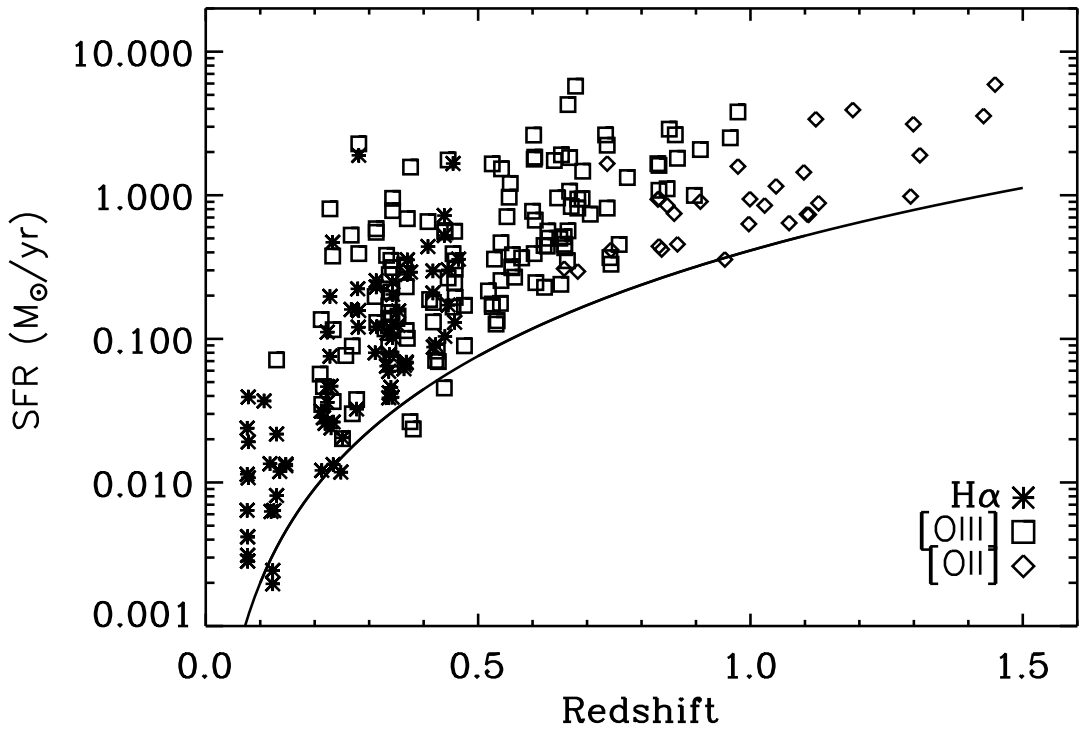

FIG. 31 Star formation rates as a function of redshift based on the line luminosities of the ELGs studied here. We see the expected bias of higher SFRs at higher redshifts, due to our detection limits. These SFRs are uncorrected for extinction and are thus lower limits. The approximate detection limit is shown.

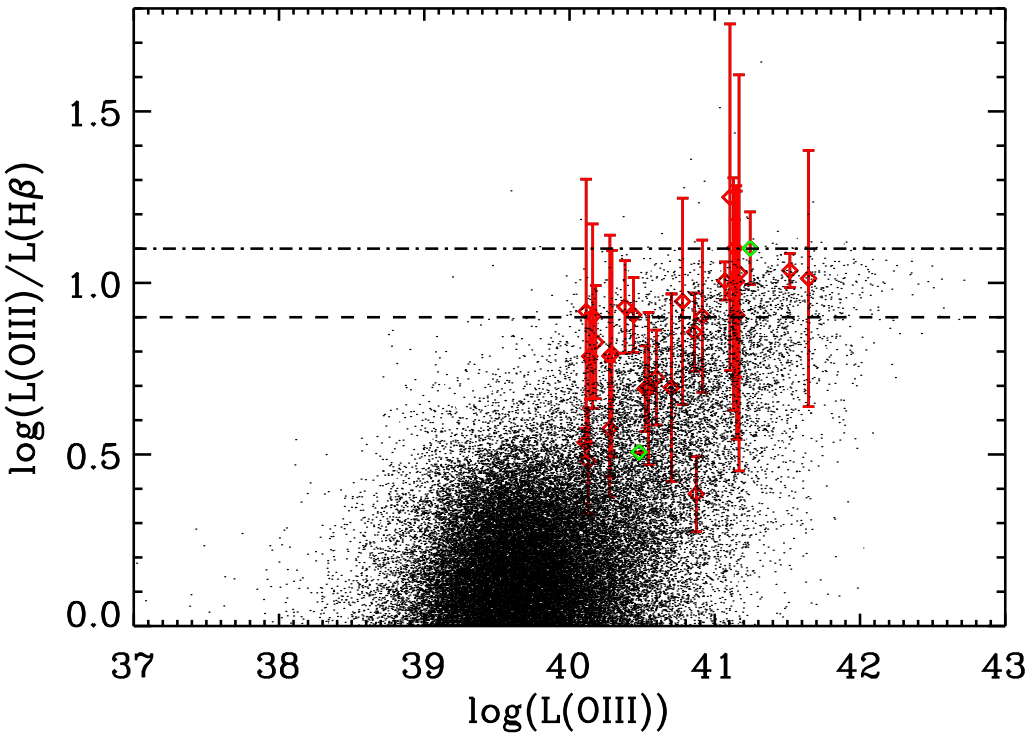

FIG. 32 [O III] to Hβ flux ratios of PEARS ELGs (red diamonds) compared to those from the SDSS AGN catalog (dots; Kauffmann et al. 2003). As discussed in Sec. 4, our objects with [O III]:Hβ $\gtrsim$8 (dashed line) are probable AGN, and ratios above 13 (dot–dashed line) are likely Seyferts. The two green diamonds are the two X–ray confirmed objects that have both [O III] and Hβ measured (PEARS Objects 40816 and 78582).

4.4.5. High-redshift Star-Forming Regions

One of the main advantages of the 2D detection method utilized for this study is the detection of emission lines in distinct star-forming regions within galaxies—regions that would not have been detected if the spectrum of the entire galaxy was extracted (Figure 20). In several cases ∼13% of galaxies we find multiple emitting knots (Figure). Many of these galaxies are clumpy, face-on spirals with distinct star-forming regions (discussed below). In total, 27 galaxies have multiple emitting knots–within these galaxies, there are 63 such knots with 80 lines (the majority of which are Hα). The median redshift of the subsample of multiple-emitting knot ELGs is z=0.336, and the highest redshift multiple-knot emitter is at z=0.653. While properties of local individual HII regions have been studied for some time (Hodge 1969; Shields 1974; Shields 1990; McCall, Rybski, & Shields 1985; Zaritsky, Kennicutt, & Huchra 1994; Gordon et al. 2004; Kennicutt 1984), grism surveys such as PEARS—combined with the 2D-detection method used here—are useful for obtaining spectra of individual intermediate–redshift star–forming regions. We find that variations in the star-formation rate in these knots are typically a factor of two or three. The most extreme SFR variations in these giant star-forming regions occur not in the face-on spirals that are the most common in the subsample of multiple-emitting knot galaxies, but in clumpy irregulars with clear merger signatures. This effect is not unexpected, as mergers are known to induce enhanced star formation activity which is revealed through the galaxies' emission lines. Regions of the galaxy that are undergoing more intense physical alterations due to the merging activity would presumably

exhibit more intense star formation. series—which will include the PEARS North fields data—we will construct the line luminosity functions of the entire sample in order arrive at better constraints for faint Hα , [O III], and [O II] emitters.

Of the galaxies with multiple emitting knots, a subset of 10 are face–on spirals containing a total of 27 knots, within a redshift range of 0.076–0.483 (seven of which are above z$\gtrsim$0.1). We examine this subset of these intermediate–redshift, multiple-knot emitters, in order to investigate the presence of "classical" (albeit giant in most cases; 9 of these 10 objects have knot luminosities that are above L$\gtrsim 10^{39}$ ergs s^{-1}) HII regions. By examining only the face-on spirals, we thus exclude star-forming regions from irregulars/mergers, in which the enhanced star formation is likely due to the merging/interacting dynamics of the object and not the more quiescent star formation that normally occurs in undisturbed disk galaxies. We use the half–light radii published in the GOODS catalogs; data is availale for all but 2 galaxies (each having 3 knots). Of these 21 knots in face-on spirals, two could be considered nuclear; the other knots are distributed across the faces of the galaxies as shown in Figure 33. The presence of knots at quite high normalized radial distances ($\gtrsim$3–4 $r_{half-light}$) could possibly be due to line–of–sight interlopers. As a comparison to the PEARS star–forming regions at an average redshift z=0.238, we also plot the radial distribution of well–studied giant extragalactic HII regions (GEHRs; Kennicutt 1984; Blitz et al. 1981; Castaneda et al. 1992; Rosa et al. 1984) in the local universe. This sample is drawn from M101, M33, and M51. From these relatively small samples, we see a peak in both the local and PEARS galaxies' giant star–forming regions around

the half–light radius. Many galaxies in the local universe are known to have resonant rings of starburst activity (e.g., NGC 1097, NGC 2841, M94) and NGC 2997 has a ring of *giant* HII regions (Meaburn & Terret 1982; Kinney et al. 1993). While the numbers of identified giant HII regions in the PEARS sample are too few to compose a ring, the peak of normalized radial distance in the sample is interesting and warrants follow–up higher–resolution observations.

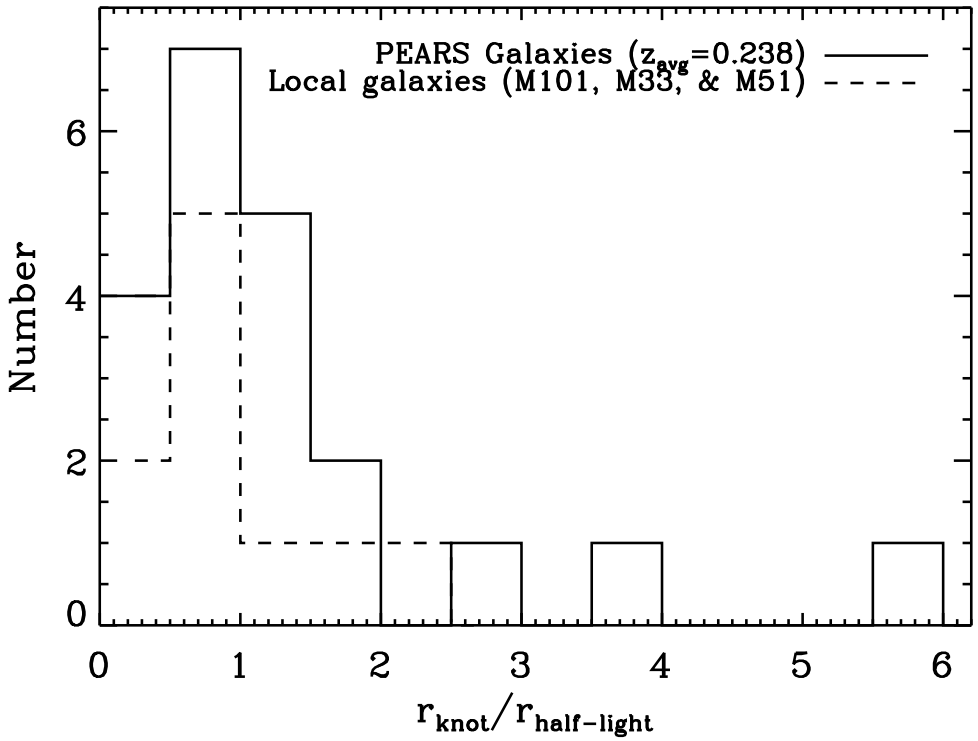

FIG. 33 Comparison of radial distributions of star–forming regions within the PEARS galaxies that have multiple (giant) SF knots to a sample of local galaxies with well–studied giant HII regions. Radial knot distances are all scaled to the half–light radii of the galaxy, as described in detail in the text. Two of the knots shown here could be considered nuclear. The PEARS sample of galaxies with multiple–emitting knots has an average redshift of z=0.238. Both sample distributions peak near the half–light radius.

TABLE 3: Global properties of Emission-Line Galaxies

PEARS ID	Knot #	RA J2000	DEC J2000	i'_{AB} mag	Wavelength (Å)	Flux 10^{-18} erg $s^{-1}cm^{-2}$	EW (Å)	Line ID	Grism Redshift
9359	1	53.1682091	-27.9300213	22.97	7349	21.2±3.5	93.5	Hα	0.120
9359	2	53.1682892	-27.9300632	22.97	7385	19.7±3.5	74.5	Hα	0.125
12250	1	53.1566811	-27.9257526	24.72	6671	57.0±2.0	312.9	[O III]	0.337
12250	1	53.1566811	-27.9257526	24.72	8774	26.1±5.3	199.0	Hα	0.337
12665	1	53.1541176	-27.9234123	22.06	7413	137.1±6.4	214.0	...	...
13541	1	53.1584473	-27.9188538	21.49	6842	112.4±2.8	Hα .2	[O III]	0.370
13541	1	53.1584473	-27.9188538	21.49	9059	75.7±8.8	83.2	Hα	0.370
13541	2	53.1584740	-27.9189358	21.49	6802	16.5±1.4	10.4	[O III]	0.370
13541	2	53.1584740	-27.9189358	21.49	9013	95.6±11.2	75.7	Hα	0.370
13553	1	53.1643639	-27.9186115	19.46	7416	23.0±6.9	19.4	Hα	0.130
14104	1	53.1616020	-27.9222107	26.60	8098	21.2±2.2	344.4	[O III]	0.621
14215†	1	53.1456490	-27.9198093	22.20	6798	9.5±2.8	11.4	[O II]	0.832
14215†	1	53.1456490	-27.9198093	22.20	9153	37.4±6.2	37.3	[O III]	0.832
15116	1	53.1471062	-27.9200668	25.61	6618	80.4±4.4	290.9	[O III]	0.332
15116	1	53.1471062	-27.9200668	25.61	8742	22.4±3.8	138.8	Hα	0.332
16788	1	53.1849480	-27.9160748	25.41	7846	3.6±0.9	28.4	Hβ	0.659
16788	1	53.1849480	-27.9160748	25.41	8065	17.7±1.2	140.3	[O III]	0.659
17024	1	53.1534920	-27.9139519	22.20	8070	3.8±0.9	12.7	Hβ	0.659
17024	1	53.1534920	-27.9139519	22.20	8288	18.7±1.5	55.3	[O III]	0.659
17362	1	53.1624565	-27.9140434	22.56	7367	8.1±1.7	12.8	[O III]	0.475
17587	1	53.1607971	-27.9138756	24.82	8240	21.3±1.9	149.8	[O III]	0.650

Continued on next page...

TABLE 3 – Continued

PEARS ID	Knot #	RA J2000	DEC J2000	i'_{AB} mag	Wavelength (Å)	Flux 10^{-18} erg $s^{-1}cm^{-2}$	EW (Å)	Line ID	Grism Redshift
18337	1	53.1779099	-27.9095287	22.25	7900	35.0±6.0	24.1	[O II]	1.120
18410	1	53.1801987	-27.9110069	22.55	7086	4.9±1.0	16.2	Hβ	0.454
18410	1	53.1801987	-27.9110069	22.55	7264	16.8±1.1	53.0	[O III]	0.454
19422	1	53.1720695	-27.9096584	24.52	7757	44.6±2.0	314.8	[O III]	0.553
19546	1	53.1468811	-27.9090500	23.61	9049	20.2±5.4	35.7	[O II]	1.428
19639	3	53.1456108	-27.9038506	19.92	8399	62.0±8.6	57.1	Hα	0.280
20201	1	53.1496544	-27.9078388	24.14	7217	186.3±5.0	528.6	[O III]	0.445
20201	1	53.1496544	-27.9078388	24.14	9514	52.7±8.0	230.5	Hα	0.445
21605	1	53.1766396	-27.9037571	23.13	8156	35.1±4.2	58.8	[O II]	1.188
21754	1	53.1799278	-27.9038067	24.07	7802	19.2±3.6	90.2	[O III]	0.562
22203	1	53.1505966	-27.9024887	22.13	6330	183.8±11.7	166.5	[O III]	0.267
22203	1	53.1505966	-27.9024887	22.13	8427	91.9±6.8	134.0	Hα	0.267
22604	1	53.1840134	-27.8996315	20.99	7975	19.9±3.5	19.1	...	...
22761	1	53.1536331	-27.9019623	24.46	6394	18.1±4.0	123.9	...	...
22829	1	53.1647568	-27.9002018	21.55	7787	74.0±3.5	46.7	[O III]	0.559
26009	1	53.1379280	-27.8946438	23.63	7163	62.0±3.5	202.7	[O III]	0.439
26107	1	53.1397209	-27.8947048	25.48	8443	36.9±3.6	318.2	...	...
26909	1	53.1390152	-27.8926620	23.02	8388	21.3±1.1	44.5	Hβ	0.679
26909	1	53.1390152	-27.8926620	23.02	8388	219.4±2.6	454.0	[O III]	0.679
26009	1	53.1379280	-27.8946438	23.02	9441	18.7±5.6	81.1	Hα	0.439
26009	1	53.1379280	-27.8946438	23.63	7163	60.6±1.6	203.6	[O III]	0.439
27293	1	53.1968880	-27.8927078	25.89	7693	18.1±4.6	304.1	...	...

Continued on next page...

TABLE 3 – Continued

PEARS ID	Knot #	RA J2000	DEC J2000	i'_{AB} mag	Wavelength (Å)	Flux 10^{-18} erg $s^{-1}cm^{-2}$	EW (Å)	Line ID	Grism Redshift
30908	1	53.1774559	-27.8812027	20.39	7234	38.2±5.1	15.0	···	···
31362	1	53.1819839	-27.8849945	24.22	8096	15.8±3.3	49.9	Hβ	0.665
31362	1	53.1819839	-27.8849945	24.22	8318	171.8±3.7	612.4	[O III]	0.665
32905	1	53.1583290	-27.8816776	23.89	7451	12.9±2.4	58.1	[O II]	0.999
33086†	1	53.1846313	-27.8809357	23.89	6891	80.2±4.5	52.7	CIII]	3.446
33086†	1	53.1846313	-27.8809357	23.89	8490	21.5±4.6	24.7	CIV	3.446
33294	1	53.1586571	-27.8801899	23.51	7630	14.1±3.1	29.2	[O II]	1.047
33355	1	53.1859474	-27.8796978	23.19	7083	47.7±3.6	176.2	···	···
35818	1	53.1835709	-27.8625374	18.86	8392	115.6±13.8	70.6	Hα	0.279
36657†	1	53.1743889	-27.8673668	22.41	7141	180.6±12.6	29.8	CIII]	3.607
36657†	1	53.1743889	-27.8673668	22.41	8759	110.8±11.1	24.5	CIV	3.607
37690	1	53.1697388	-27.8713989	23.61	6793	16.1±4.7	50.0	···	···
38750	1	53.1655579	-27.8651085	20.82	6871	17.2±1.6	16.8	Hβ	0.408
38750	1	53.1655579	-27.8651085	20.82	7032	85.2±3.0	68.7	[O III]	0.408
38750	1	53.1655579	-27.8651085	20.82	9345	93.9±12.9	87.4	Hα	0.408
39387	1	53.1705093	-27.8666763	21.31	6725	26.3±4.8	62.5	[O III]	0.353
39387	1	53.1705093	-27.8666763	21.31	8881	37.3±10.7	29.9	Hα	0.353
40117	1	53.1818123	-27.8668137	23.96	8520	25.6±4.3	143.4	[O III]	0.706
40163	1	53.1791611	-27.8665504	24.06	9474	19.2±1.4	60.7	[O III]	0.897
40816†	1	53.1844559	-27.8614178	19.48	6182	56.0±17.0	12.8	Hβ	0.281
40816†	1	53.1844559	-27.8614178	19.48	6353	706.6±21.7	147.0	[O III]	0.281
40816†	1	53.1844559	-27.8614178	19.48	8408	967.9±41.2	160.9	Hα	0.281

Continued on next page...

TABLE 3 – Continued

PEARS ID	Knot #	RA J2000	DEC J2000	i'_{AB} mag	Wavelength (Å)	Flux 10^{-18} erg $s^{-1}cm^{-2}$	EW (Å)	Line ID	Grism Redshift
41078	1	53.1807861	-27.8651638	24.30	6953	8.9±2.9	28.7	[O II]	0.866
41078	1	53.1807861	-27.8651638	24.30	9316	38.0±7.2	130.2	[O III]	0.866
43170	1	53.1561699	-27.8608074	24.06	8451	53.6±4.6	347.9	[O III]	0.692
45223	1	53.1973305	-27.8572559	24.48	8106	5.3±1.2	26.7	Hβ	0.668
45223	1	53.1973305	-27.8572559	24.48	8331	42.4±2.0	206.9	[O III]	0.668
45454	1	53.1814690	-27.8563213	22.75	7105	9.7±0.9	81.1	[O III]	0.425
46562	1	53.1642036	-27.8534393	23.03	8319	22.7±2.0	82.0	[O III]	0.665
46994	1	53.1643944	-27.8536777	24.22	8108	7.2±1.0	32.4	Hβ	0.668
46994	1	53.1643944	-27.8536777	24.22	8332	72.7±1.9	287.3	[O III]	0.668
48890	1	53.2069473	-27.8480740	23.07	7110	15.7±3.5	18.8	[O II]	0.908
48890	1	53.2069473	-27.8480740	23.07	9566	38.9±12.2	48.6	[O III]	0.908
49766	1	53.1751556	-27.8476467	23.57	6059	20.3±5.1	285.1	[O III]	0.213
49766	1	53.1751556	-27.8476467	23.57	8041	11.6±3.3	64.6	Hα	0.213
51061	1	53.2095871	-27.8468800	25.50	7890	20.5±3.2	173.3	[O III]	0.580
51356	1	53.1567993	-27.8429546	21.59	8126	20.5±2.1	78.6	[O III]	0.627
51976	1	53.2045479	-27.8425064	23.73	9280	56.0±10.2	147.4	[O III]	0.862
51976	1	53.2045479	-27.8425064	23.73	6939	14.8±4.0	43.3	[O II]	0.86
52086	1	53.1578102	-27.8444538	23.53	4954	4.1±0.7	11.4	Hβ	0.526
52086	1	53.1578102	-27.8444538	23.53	7620	12.4±1.0	127.4	[O III]	0.526
52086	2	53.1577988	-27.8443146	23.53	7419	6.6±1.0	18.6	Hβ	0.526
52086	2	53.1577988	-27.8443146	23.53	7619	117.3±3.2	316.6	[O III]	0.526
52398	1	53.1938133	-27.8442917	24.19	8323	12.7±3.3	38.4	···	0.000

Continued on next page...

TABLE 3 – Continued

PEARS ID	Knot #	RA J2000	DEC J2000	i'_{AB} mag	Wavelength (Å)	Flux 10^{-18} erg $s^{-1}cm^{-2}$	EW (Å)	Line ID	Grism Redshift
52502	1	53.2011223	-27.8412380	21.53	7216	28.1±1.7	84.1	[O III]	0.445
52502	1	53.2011223	-27.8412380	21.53	9485	29.9±9.0	55.5	Hα	0.445
53462	1	53.1896210	-27.8419609	22.81	7804	18.9±3.8	39.5	[O III]	0.562
54022	1	53.1747398	-27.8407822	22.37	6669	18.0±2.3	41.1	[O III]	0.336
54022	1	53.1747398	-27.8407822	22.37	8769	20.0±5.6	62.2	Hα	0.336
54022	2	53.1746254	-27.8408928	22.37	6499	4.2±1.4	14.7	Hβ	0.336
54022	2	53.1746254	-27.8408928	22.37	6675	34.7±3.4	94.2	[O III]	0.336
55102	1	53.1756477	-27.8385963	21.85	7224	30.2±5.3	61.8	[O III]	0.458
55102	2	53.1757545	-27.8387928	21.85	7281	34.5±1.6	133.7	[O III]	0.458
56801	1	53.1450958	-27.8373871	23.96	8040	7.5±0.9	33.1	Hβ	0.653
56801	1	53.1450958	-27.8373871	23.96	8259	80.2±3.4	297.3	[O III]	0.653
56875	1	53.1529732	-27.8376999	24.52	7695	11.7±1.2	98.8	[O III]	0.541
58985	1	53.1999168	-27.8340626	23.78	7807	23.2±3.4	101.5	[O III]	0.563
59018	1	53.1763496	-27.8306465	20.63	9606	56.5±13.2	40.0	Hα	0.464
59905	1	53.1802177	-27.8329601	25.30	8417	35.8±4.2	185.9	...	...
60143	1	53.1482964	-27.8289299	21.25	7729	30.8±3.5	37.2	[O III]	0.542
63612	1	53.1554031	-27.8261337	25.33	7820	3.3±0.7	27.2	Hβ	0.606
63612	1	53.1554031	-27.8261337	25.33	8022	12.4±1.1	127.8	[O III]	0.606
66061†	1	53.1801453	-27.8206253	22.68	8161	81.5±6.7	73.6	888	1.917
68739	1	53.1607819	-27.8163223	24.88	7624	11.9±1.0	162.0	[O III]	0.526
70314	1	53.1748161	-27.7995949	20.36	7526	28.4±13.9	68.9	Hα	0.147
70314	2	53.1750183	-27.7993336	20.36	7527	29.1±5.6	86.3	Hα	0.147

Continued on next page...

TABLE 3 – Continued

PEARS ID	Knot #	RA J2000	DEC J2000	i'_{AB} mag	Wavelength (Å)	Flux 10^{-18} erg $s^{-1}cm^{-2}$	EW (Å)	Line ID	Grism Redshift
70337	1	53.1938210	-27.8128853	23.40	6802	20.3±3.5	60.0	[O II]	0.830
70337	1	53.1938210	-27.8128853	23.40	9142	38.7±6.7	106.3	[O III]	0.830
70407†	1	53.1851540	-27.8052826	20.52	9300	60.4±26.1	28.1	Hα	0.417
70407†	7	53.1851730	-27.8052406	20.52	9452	42.4±20.0	20.2	Hα	0.417
70651	1	53.1530495	-27.8121529	23.33	6040	80.0±9.8	559.0	[O III]	0.212
70651	1	53.1530495	-27.8121529	23.33	7956	30.4±3.3	295.6	Hα	0.212
71864	1	53.1506119	-27.8095131	24.86	8786	13.2±0.7	80.0	[O III]	0.759
71924	1	53.1536827	-27.8088989	23.84	6898	3.6±1.0	13.1	[O III]	0.381
72179	1	53.1310501	-27.8084450	23.34	6281	29.1±10.5	93.7	[O III]	0.257
72509	1	53.1705208	-27.8066082	24.53	8548	7.1±3.1	28.1	[O II]	1.294
72557	1	53.1338768	-27.8068733	23.56	6673	15.7±3.2	477.2	NA	···
73619	1	53.1844063	-27.8051853	26.88	8250	10.1±1.2	69.4	[O III]	0.652
74234	1	53.1377335	-27.8042202	25.95	7492	2.7±0.7	34.7	Hβ	0.542
74234	1	53.1377335	-27.8042202	25.95	7705	16.8±1.4	206.9	[O III]	0.542
75506	1	53.1472664	-27.8008537	26.26	8419	17.1±7.3	1157.5	Hα	0.277
75506	1	53.1472664	-27.8008537	26.26	6379	12.1±0.9	162.3	[O III]	0.277
75547	1	53.1733017	-27.7993031	23.78	7372	7.8±2.4	59.9	Hα	0.123
75547	2	53.1732941	-27.7992783	23.78	7372	6.3±1.9	45.8	Hα	0.123
75753	1	53.1872597	-27.7943401	22.29	6499	7.2±1.1	20.4	Hβ	0.343
75753	1	53.1872597	-27.7943401	22.29	6709	61.3±1.5	143.1	[O III]	0.343
75753	1	53.1872597	-27.7943401	22.29	8816	32.8±4.2	179.7	Hα	0.343
75753	2	53.1873703	-27.7942238	22.29	6490	17.3±0.5	29.1	Hβ	0.343

Continued on next page...

TABLE 3 – Continued

PEARS ID	Knot #	RA J2000	DEC J2000	i'_{AB} mag	Wavelength (Å)	Flux 10^{-18} erg $s^{-1}cm^{-2}$	EW (Å)	Line ID	Grism Redshift
75753	2	53.1873703	-27.7942238	22.29	6685	152.8±1.0	228.4	[O III]	0.343
75753	2	53.1873703	-27.7942238	22.29	8819	65.5±4.9	207.8	Hα	0.343
75753	3	53.1878090	-27.7939053	22.29	8800	80.0±6.9	123.5	Hα	0.343
75753	3	53.1878090	-27.7939053	22.29	6697	186.0±3.9	234.1	[O III]	0.343
76154	1	53.1512299	-27.7987995	23.73	8016	39.9±1.3	183.3	[O III]	0.600
77558	8	53.1864052	-27.7910328	18.67	7995	23.1±5.2	···	NA	···
77558	11	53.1871910	-27.7909679	18.67	7894	84.6±15.1	···	NA	···
77902	1	53.1559830	-27.7949619	23.51	7720	7.4±2.3	53.3	[O II]	1.071
78021	1	53.1839218	-27.7954350	27.62	8615	13.3±3.6	294.2	[O II]	1.311
78077	1	53.1841545	-27.7926388	21.73	6482	48.2±17.7	32.0	[O II]	0.737
78077	1	53.1841545	-27.7926388	21.73	8675	69.7±4.8	41.7	[O III]	0.737
78237	1	53.1876869	-27.7943954	20.50	6693	14.4±0.9	25.5	[O III]	0.340
78237	1	53.1876869	-27.7943954	20.50	8800	38.7±6.8	160.4	Hα	0.340
78237	2	53.1879768	-27.7943249	20.50	6701	70.2±16.6	381.6	[O III]	0.340
78237	3	53.1877136	-27.7942200	20.50	7872	20.6±3.8	39.7	NA	···
78491	1	53.1548195	-27.7934532	22.70	7143	15.4±3.9	237.0	NA	···
78491	3	53.1544189	-27.7933788	22.70	8100	10.3±2.7	224.3	Hα	0.234
78491	3	53.1544189	-27.7933788	22.70	6120	17.2±3.8	190.1	[O III]	0.234
78491	4	53.1547127	-27.7931709	22.70	6114	54.5±5.4	275.6	[O III]	0.234
78491	4	53.1547127	-27.7931709	22.70	8080	20.4±3.0	144.1	Hα	0.234
78582†	2	53.1615829	-27.7922630	21.18	7013	12.3±2.4	5.6	Hβ	0.454
78582†	2	53.1615829	-27.7922630	21.18	7100	39.5±2.4	16.8	[O III]	0.454

Continued on next page...

TABLE 3 – Continued

PEARS ID	Knot #	RA J2000	DEC J2000	i'_{AB} mag	Wavelength (Å)	Flux 10^{-18} erg $s^{-1}cm^{-2}$	EW (Å)	Line ID	Grism Redshift
78582†	2	53.1615829	-27.7922630	21.18	9542	276.2±54.4	189.4	Hα	0.454
78762	1	53.1618958	-27.7925568	22.77	7284	19.2±1.0	82.6	[O III]	0.458
79283	2	53.1419983	-27.7867641	20.76	8070	19.3±5.9	36.2	Hα	0.230
79283	3	53.1421967	-27.7865429	20.76	8059	37.7±5.9	···	Hα	0.230
79400	1	53.1673317	-27.7918015	23.98	6867	4.2±0.9	16.1	[O III]	0.375
79483†	1	53.1879654	-27.7900734	23.98	9200	94.9±17.6	54.0	Hα	0.438
79483†	2	53.1879539	-27.7900009	23.98	9437	130.6±23.6	55.5	Hα	0.438
79483†	2	53.1879539	-27.7900009	20.85	7001	5.0±1.4	2.2	[O III]	0.438
79520	1	53.1861954	-27.7916622	26.73	8703	11.3±1.4	55.8	[O III]	0.742
80071	1	53.1866226	-27.7902203	27.06	7335	47.2±3.0	224.1	Hα	0.118
80255	1	53.1848145	-27.7899342	23.68	7278	5.5±1.6	···	[O II]	0.953
80500	1	53.1472092	-27.7884693	23.36	8064	4.0±0.8	15.0	Hβ	0.658
80500	1	53.1472092	-27.7884693	23.36	8300	21.2±1.1	82.8	[O III]	0.658
80500	1	53.1472092	-27.7884693	23.36	6178	11.8±3.5	42.9	[O II]	0.658
80666	1	53.1765137	-27.7897243	25.04	6849	3.0±0.7	25.1	Hβ	0.411
80666	1	53.1765137	-27.7897243	25.04	7047	24.0±1.3	223.0	[O III]	0.411
81032	1	53.1815071	-27.7879314	23.36	6045	34.1±9.8	119.2	[O III]	0.210
81256	1	53.1920815	-27.7872849	23.05	7841	7.9±2.4	36.4	[O II]	1.104
81609	1	53.1640930	-27.7872963	24.37	7820	15.7±2.8	60.7	[O II]	1.098
81944	1	53.1446838	-27.7855377	22.53	8138	62.1±4.5	74.8	Hα	0.228
81944	2	53.1447372	-27.7854137	22.53	6132	401.0±12.5	483.2	[O III]	0.228
81944	2	53.1447372	-27.7854137	22.53	8129	162.1±9.4	341.4	Hα	0.228

Continued on next page...

TABLE 3 – Continued

PEARS ID	Knot #	RA J2000	DEC J2000	i'_{AB} mag	Wavelength (Å)	Flux 10^{-18} erg $s^{-1}cm^{-2}$	EW (Å)	Line ID	Grism Redshift
82307	1	53.1634598	-27.7866497	25.28	7369	15.5±2.9	···	[O III]	0.475
83381	1	53.1765251	-27.7825947	24.96	6640	25.3±1.5	293.1	[O III]	0.329
83553†	1	53.1784821	-27.7840424	24.89	6462	94.9±5.2	93.2	CIV	3.166
83553†	1	53.1784821	-27.7840424	24.89	7940	13.3±3.3	26.8	CIII	3.166
83686	1	53.1518135	-27.7829018	23.50	6848	8.9±3.1	39.0	[O II]	0.837
83789	1	53.1527901	-27.7826843	24.81	8862	36.8±1.3	156.6	[O III]	0.774
83804	1	53.1845818	-27.7833576	25.04	7918	9.0±2.6	70.0	[O II]	1.125
83834	1	53.1580925	-27.7812119	21.95	8102	10.8±1.1	34.2	[O III]	0.622
85517	1	53.1763344	-27.7808685	24.85	7409	3.1±0.7	21.4	Hβ	0.530
85517	1	53.1763344	-27.7808685	24.85	7645	25.0±0.9	174.9	[O III]	0.530
85844	1	53.1624680	-27.7803612	26.19	8569	22.4±3.8	240.7	[O II]	1.299
87294	1	53.1629181	-27.7752514	21.03	8192	8.0±2.1	194.1	Hα	0.248
87464	1	53.1878166	-27.7726479	22.58	7460	61.7±9.2	170.9	Hα	0.130
87464	1	53.1878166	-27.7726479	22.58	5642	123.1±20.7	394.7	[O III]	0.130
87658	1	53.1477661	-27.7769241	24.06	7854	7.8±2.4	30.6	[O II]	1.107
88580	1	53.1620064	-27.7740345	22.65	6354	10.3±0.5	29.4	[O III]	0.269
88580	2	53.1619110	-27.7738514	22.65	6338	30.5±1.1	86.6	[O III]	0.269
89030	1	53.1604347	-27.7752380	21.74	9127	32.3±4.3	101.3	[O II]	1.449
89209	1	53.1503944	-27.7720318	21.27	6075	26.2±4.7	182.0	[O III]	0.216
89209	1	53.1503944	-27.7720318	21.27	8000	26.2±4.7	182.0	Hα	0.216
89853	1	53.1375847	-27.7691345	21.91	8952	17.3±5.4	20.1	Hα	0.364
89923	1	53.1739769	-27.7720718	21.27	8751	37.8±6.9	43.5	Hα	0.333

Continued on next page...

TABLE 3 – Continued

PEARS ID	Knot #	RA J2000	DEC J2000	i'_{AB} mag	Wavelength (Å)	Flux 10^{-18} erg $s^{-1}cm^{-2}$	EW (Å)	Line ID	Grism Redshift
90116	1	53.1948090	-27.7733440	25.48	8143	23.0±3.5	325.2	[O III]	0.630
90246	1	53.1512070	-27.7728481	24.08	8008	20.0±0.9	127.8	[O III]	0.603
91205	1	53.1505280	-27.7713089	21.27	7857	26.6±7.5	73.1	NA	···
91789	1	53.1470642	-27.7701302	23.84	7655	8.7±0.8	55.8	[O III]	0.533
92839†	1	53.1628647	-27.7671719	20.98	6201	0.0±0.0	···	MgII	1.215
94632	1	53.1795502	-27.7662010	25.05	8310	14.1±1.0	121.8	[O III]	0.664
95471	1	53.1773453	-27.7639313	22.40	8002	23.2±8.4	51.2	Hα	0.219
96123	1	53.1429062	-27.7636814	23.15	7665	9.1±2.7	22.3	[O III]	0.535
96627	1	53.1704559	-27.7614193	21.53	7453	30.7±8.7	51.8	Hα	0.136
97568	1	53.1252556	-27.7565651	22.31	9807	40.6±17.3	35.2	[O III]	0.963
97655	1	53.1140289	-27.7612534	23.72	7502	9.9±2.5	31.3	Hβ	0.543
97655	1	53.1140289	-27.7612534	23.72	7706	100.3±2.2	346.8	[O III]	0.543
100188	1	53.1012573	-27.7568226	25.07	6353	7.2±1.3	46.5	Hβ	0.311
100188	1	53.1012573	-27.7568226	25.07	6521	48.4±1.9	326.1	[O III]	0.311
100188	1	53.1012573	-27.7568226	25.07	8603	32.3±3.9	425.5	Hα	0.311
102156	1	53.1258965	-27.7512856	21.72	7551	31.2±7.1	13.5	NeIII	0.738
102156	1	53.1258965	-27.7512856	21.72	8553	182.0±15.5	67.0	Hgm	0.738
103116	1	53.1055984	-27.7507782	22.76	7369	23.0±3.9	32.0	[O II]	0.977
103116	1	53.1055984	-27.7507782	22.76	9900	59.3±4.9	66.1	[O III]	0.977
103422	1	53.1073837	-27.7498055	23.01	6826	20.4±3.9	28.2	[O II]	0.832
103422	1	53.1073837	-27.7498055	23.01	9141	25.1±1.2	35.9	[O III]	0.832
104408	1	53.1160088	-27.7471771	24.26	8677	25.4±4.8	145.5	[O III]	0.737

Continued on next page...

TABLE 3 – Continued

PEARS ID	Knot #	RA J2000	DEC J2000	i'_{AB} mag	Wavelength (Å)	Flux 10^{-18} erg $s^{-1}cm^{-2}$	EW (Å)	Line ID	Grism Redshift
104849†	9	53.1243820	-27.7399654	16.60	7042	213.3±39.5	26.8	Hα	0.076
104849†	12	53.1246300	-27.7395153	16.60	7060	57.1±12.2	18.0	Hα	0.076
104849†	13	53.1243668	-27.7394562	16.60	7069	101.8±19.7	22.4	Hα	0.076
104850†	1	53.1249161	-27.7347584	17.02	7040	333.0±105.2	17.5	Hα	0.078
104850†	6	53.1253090	-27.7345448	17.02	7092	91.1±20.5	18.2	Hα	0.078
104850†	13	53.1246567	-27.7350121	17.02	7035	162.2±27.7	34.0	Hα	0.078
104992	1	53.1182327	-27.7405071	19.65	7078	36.2±7.8	37.4	Hα	0.077
104992	2	53.1179123	-27.7407436	19.65	7081	24.6±4.7	32.7	Hα	0.077
104992	3	53.1180611	-27.7403069	19.65	7067	36.4±5.0	53.5	Hα	0.077
104992	4	53.1180649	-27.7406502	19.65	7109	24.6±5.6	23.1	Hα	0.077
104992	5	53.1178970	-27.7405090	19.65	7055	27.0±5.3	34.1	Hα	0.077
105723	1	53.1138153	-27.7412968	20.08	8034	96.1±8.9	82.9	Hα	0.223
105723	2	53.1135063	-27.7413902	20.08	8028	31.2±5.5	43.9	Hα	0.223
105723	3	53.1136093	-27.7413673	20.08	8078	40.1±7.0	43.3	Hα	0.223
106136	1	53.1138039	-27.7442055	24.40	6668	28.5±3.5	271.9	[O III]	0.336
106136	1	53.1138039	-27.7442055	24.40	8766	13.1±4.4	211.1	Hα	0.336
106491	1	53.1136703	-27.7437534	25.04	6673	39.0±1.8	251.4	[O III]	0.337
106491	1	53.1136703	-27.7437534	25.04	8777	14.1±3.6	140.8	Hα	0.337
106761	1	53.1213455	-27.7440891	25.81	8341	32.5±3.9	310.5	...	...
108642	1	53.0944366	-27.7341156	21.48	8673	91.4±9.2	86.3	Hα	0.313
108642	1	53.0944366	-27.7341156	21.48	6569	133.5±10.9	90.5	[O III]	0.313
108642	2	53.0944328	-27.7341805	21.48	6524	141.4±11.2	79.8	[O III]	0.313

Continued on next page...

TABLE 3 – Continued

PEARS ID	Knot #	RA J2000	DEC J2000	i'_{AB} mag	Wavelength (Å)	Flux 10^{-18} erg $s^{-1}cm^{-2}$	EW (Å)	Line ID	Grism Redshift
108642	2	53.0944328	-27.7341805	21.48	8617	101.1±9.9	80.7	Hα	0.313
109332	1	53.0898247	-27.7366867	23.12	8958	18.2±4.3	35.1	Hα	0.365
109332	1	53.0898247	-27.7366867	23.12	6803	55.3±4.0	56.4	[O III]	0.365
109547	1	53.0892677	-27.7360077	24.96	6809	38.2±1.7	321.5	[O III]	0.368
109547	1	53.0892677	-27.7360077	24.96	8978	18.8±4.3	219.3	Hα	0.368
109652	1	53.0903625	-27.7367249	21.64	6800	18.9±1.1	88.9	[O III]	0.368
109652	1	53.0903625	-27.7367249	21.64	8975	18.5±4.9	186.2	Hα	0.368
109900	1	53.1128082	-27.7346249	22.42	6499	11.8±3.9	27.2	[O II]	0.744
109900	1	53.1128082	-27.7346249	22.42	8731	10.1±1.4	29.2	[O III]	0.744
109953	1	53.0901070	-27.7361164	21.64	6811	19.3±2.8	143.9	...	...
110085	1	53.1391296	-27.7303295	20.00	7265	159.7±13.6	79.6	Hα	0.107
110494	1	53.1079712	-27.7337646	21.99	6358	121.6±10.6	77.9	[O III]	0.281
110494	1	53.1079712	-27.7337646	21.99	8406	80.3±7.5	75.6	Hα	0.281
111285	1	53.0815697	-27.7334805	26.18	8897	50.1±7.0	284.5	...	...
111549	1	53.1024857	-27.7296772	22.12	6461	31.2±8.2	48.6	[O III]	0.314
111549	1	53.1024857	-27.7296772	22.12	8625	48.0±5.9	72.7	Hα	0.314
112157	1	53.0659561	-27.7309017	24.45	6853	247.5±1.0	508.2	[O III]	0.376
112157	1	53.0659561	-27.7309017	24.45	9030	75.6±5.5	390.2	Hα	0.376
113173	1	53.1425781	-27.7288322	24.65	7284	26.2±2.7	125.0	...	...
114392	1	53.0956268	-27.7258739	23.69	7829	15.9±0.9	51.6	[O III]	0.567
116191	1	53.1104584	-27.7176895	20.86	8008	63.9±5.7	99.9	...	...
117070	1	53.0580940	-27.7200108	23.26	8404	35.4±3.0	268.5	[O III]	0.683

Continued on next page...

TABLE 3 – Continued

PEARS ID	Knot #	RA J2000	DEC J2000	i'_{AB} mag	Wavelength (Å)	Flux 10^{-18} erg $s^{-1}cm^{-2}$	EW (Å)	Line ID	Grism Redshift
117138	1	53.0722466	-27.7189407	21.24	8213	31.0±4.8	79.4	···	···
117429	1	53.0714111	-27.7176018	20.85	7589	24.7±3.5	7.5	Hβ	0.557
117429	1	53.0714111	-27.7176018	20.85	7778	59.9±4.5	19.4	[O III]	0.557
117929	1	53.1232452	-27.7181969	22.12	6668	13.4±2.8	24.1	[O III]	0.340
117929	2	53.1227493	-27.7181206	22.12	6675	42.3±3.5	65.8	[O III]	0.340
117929	2	53.1227493	-27.7181206	22.12	8794	15.1±3.5	41.6	Hα	0.340
118087	1	53.0384369	-27.7142029	20.80	8887	46.7±10.9	29.9	Hα	0.354
118091	1	53.1171913	-27.7188969	23.51	6685	30.0±3.7	158.0	[O III]	0.342
118091	1	53.1171913	-27.7188969	23.51	8807	12.7±3.8	109.8	Hα	0.342
118100	1	53.0703316	-27.7179108	23.27	8224	41.3±1.8	119.4	[O III]	0.646
118138	1	53.1340027	-27.7167816	21.13	7970	17.7±3.2	19.1	···	···
118526	1	53.0735359	-27.7174034	22.67	8130	26.0±1.5	57.8	[O III]	0.628
118673	1	53.0913582	-27.7176514	24.62	8670	26.4±4.3	164.6	···	···
119193†	1	53.0577431	-27.7136040	21.23	8661	83.0±6.9	80.6	[O III]	0.734
119341	1	53.0700302	-27.7166138	25.23	8222	4.8±1.0	54.1	Hβ	0.691
119341	1	53.0700302	-27.7166138	25.23	8449	34.5±1.3	314.8	[O III]	0.691
119489†	1	53.0551300	-27.7113838	19.83	7933	396.6±24.7	115.0	···	···
119996	1	53.0351372	-27.7130699	22.72	7007	44.3±3.5	121.9	···	···
120803	1	53.0748215	-27.7127495	22.73	8017	33.9±2.3	140.2	[O III]	0.605
121127	1	53.0573578	-27.7133713	21.23	7588	15.8±1.4	141.0	[O III]	0.519
121733	1	53.0399170	-27.7116451	23.49	6270	10.3±3.7	21.9	[O II]	0.683
121733	1	53.0399170	-27.7116451	23.49	8404	30.6±3.9	88.3	[O III]	0.683

Continued on next page...

TABLE 3 – Continued

PEARS ID	Knot #	RA J2000	DEC J2000	i'_{AB} mag	Wavelength (Å)	Flux 10^{-18} erg $s^{-1}cm^{-2}$	EW (Å)	Line ID	Grism Redshift
121817	1	53.0965118	-27.7111111	24.60	8345	32.8±3.9	254.2	[O III]	0.671
121821	1	53.0656967	-27.7118549	23.80	8017	20.6±3.7	112.1	···	···
122206	1	53.0856705	-27.7113590	24.76	7443	8.7±2.4	79.8	[O II]	0.997
122206	1	53.0856705	-27.7113590	24.76	9975	0.0±0.0	0.0	[O III]	0.997
122668	1	53.0660706	-27.7097225	23.07	6242	8.1±1.3	28.1	[O III]	0.251
122668	1	53.0660706	-27.7097225	23.07	8211	13.5±4.4	60.8	Hα	0.251
123008	1	53.0693550	-27.7090988	23.22	7975	8.3±1.1	24.4	Hβ	0.640
123008	1	53.0693550	-27.7090988	23.22	8191	77.0±2.4	217.1	[O III]	0.640
123301	1	53.0775757	-27.7081566	22.56	7800	11.6±1.0	42.3	Hβ	0.604
123301	1	53.0775757	-27.7081566	22.56	8013	93.4±2.3	285.0	[O III]	0.604
123301	2	53.0772972	-27.7082272	22.56	8001	134.3±2.4	241.9	[O III]	0.602
123448†	1	53.0586624	-27.7084484	24.71	8520	12.8±3.8	32.3	···	···
123859	1	53.0642700	-27.7057590	22.62	6888	3.6±0.9	14.2	Hβ	0.418
123859	1	53.0642700	-27.7057590	22.62	7077	22.0±1.2	81.8	[O III]	0.418
123859	1	53.0642700	-27.7057590	22.62	9338	17.7±6.9	106.6	Hα	0.418
123859	2	53.0643845	-27.7058506	22.62	7083	16.1±1.1	73.0	[O III]	0.418
124708	1	53.0647736	-27.7055855	24.71	7075	22.6±4.1	294.8	···	···
124761	1	53.0544395	-27.7015305	21.29	7127	8.1±0.7	23.5	[O III]	0.427
124761	1	53.0544395	-27.7015305	21.29	9400	0.0±0.0	0.0	Hα	0.427
125541	1	53.0909691	-27.7038784	23.88	7551	10.9±3.0	31.0	[O II]	1.026
125725	1	53.0384941	-27.6966705	19.88	8171	70.8±10.3	27.8	···	···
126769	1	53.0761490	-27.7011623	23.04	6882	17.5±3.4	28.2	[O II]	0.847

Continued on next page...

TABLE 3 – Continued

PEARS ID	Knot #	RA J2000	DEC J2000	i'_{AB} mag	Wavelength (Å)	Flux 10^{-18} erg $s^{-1}cm^{-2}$	EW (Å)	Line ID	Grism Redshift
126769	1	53.0761490	-27.7011623	23.04	9249	24.6±8.2	40.2	[O III]	0.847
127697	1	53.0613823	-27.6981525	22.61	7040	8.5±1.3	15.1	[O III]	0.422
127697	1	53.0613823	-27.6981525	22.61	9333	18.0±5.4	28.5	Hα	0.422
128312†	1	53.0825119	-27.6896687	18.99	6118	179.0±23.9	35.9	[O III]	0.233
128312†	1	53.0825119	-27.6896687	18.99	8094	367.4±35.1	59.4	Hα	0.233
128538	1	53.0531883	-27.6954632	22.68	6900	4.0±0.8	20.7	Hβ	0.457
128538	1	53.0531883	-27.6954632	22.68	7083	24.5±1.8	140.0	[O III]	0.457
128538	2	53.0531197	-27.6958714	22.68	7092	55.7±3.5	193.0	[O III]	0.457
128538	2	53.0531197	-27.6958714	22.68	9348	21.3±5.8	101.4	Hα	0.457
129968	1	53.0494003	-27.6943188	23.54	7795	7.2±2.3	25.4	Hβ	0.603
129968	1	53.0494003	-27.6943188	23.54	8007	90.9±1.9	256.9	[O III]	0.603
130264	1	53.0469208	-27.6908588	22.64	7681	17.0±3.2	17.5	...	...
133441	1	53.0813599	-27.6865711	24.98	9245	63.3±6.7	269.9	[O III]	0.851

TABLE 4: Summary of ELG Detections in South Fields

Field	# of Lines	# of Knots	# of Galaxies	# of Galaxies with multiple knots	# of Knots with multiple lines
HUDF	103	78	63	12	15
South 1	52	34	33	2	8
South 2	52	34	33	3	9
South 3	68	48	37	6	15
South 4	46	33	34	3	10
TOTAL	320	230	203	26	61

TABLE 5: Summary of Lines Detected in South Fields

Field	# [O III]	# Hα	# [O II]	# Hβ	# C IV	# C III]	# MgII	# NeIII	# Hγ	# No ID
HUDF	43	31	13	8	1	1	1	0	0	4
South 1	20	11	6	7	1	1	0	0	0	7
South 2	26	10	4	8	1	1	1	0	0	3
South 3	22	24	4	2	1	0	0	1	1	8
South 4	26	8	4	4	0	0	0	0	0	8
TOTAL	136	83	30	30	4	3	2	1	1	30

4.5 Summary

We present results from a search for emission-line galaxies in the five PEARS South Fields, including the HUDF. We outline briefly the method used to arrive at our catalog, which relies on spectral extractions from individual emitting knots within galaxies, detected first in the 2D grism image. In this way, we detect emission-line sources that would likely otherwise be missed in the standard extraction of entire galaxies, where continuum flux can often dominate the spectrum and wash out the line. Here we summarize our findings:

(*a.*) We detect 320 emission lines from 230 galaxy knots within 203 individual galaxies. The most common line is [O III]; Hα is also common, with several [O II] as well. We detect 26 galaxies with multiple emitting knots.

(*b.*) We present in Table 1 118 new spectroscopic grism redshifts in the GOODS-South Field. Line identifications are obtained by either line ratios (where two lines are present) or by utilizing previously measured (mostly photometric) redshifts for these objects as a first-guess.

(*c.*) We calculate SFRs of the ELG sample using Hα and [O II] where available, and derive an [O III] SFR based on the the more dependable lines when two lines are available in the spectra. The SFR as a function of redshift is given in Figure 31.

(*d.*) Including (blended) Hβ in our line fits results in identification of probable AGN based on approximate excitation levels. In comparison to AGN from SDSS, we find that the PEARS AGN candidates are situated in the high–excitation, high–luminosity region of the distribution.

(*e.*) The 2D detection method utilized for the PEARS South grism data allows us to detect individual star-forming regions in galaxies up to z$\sim$0.5. We find that the normalized radial distance giant star–forming knots peaks near the half–light radii of the galaxies—as does a comparison sample of nearby giant HII regions in M101, M31, and M51.

Future work with this data will begin with analysis of the PEARS North Fields, which are currently being reduced, and will result in the second in this series of papers. Detailed studies using sources from both the PEARS South and North Fields will include an in–depth study of line luminosity functions and star-formation rate densities, which will be possible once simulations of the data are completed in order to obtain accurate estimates of incompleteness. Future slitless spectroscopy studies with the Wide Field Camera 3, to be installed on HST in the next Servicing Mission, will provide a wealth of information and confirmation for the objects already identified here, as well as detection of new ELGs at higher redshifts.

We thank Mark Dickinson for useful discussions. This research was supported in part by the NASA/UNCFSP Harriett G. Jenkins Predoctoral Fellowship program (ANS), as well as by grants HST-GO-10530 & HST-GO-9793 from STScI, which is operated by AURA for NASA under contract NAS 5-26555.

5. CONCLUSIONS

We have used data from the Hubble Space Telescope to study two important and inter–related types of galaxies: early–stage mergers and emission–line galaxies. Both the tadpole galaxies and the ELGs serve to probe the evolutionary history of the universe in different but complementary ways. The tadpoles allow us to investigate a very precise stage in the process of galaxy merging, and the ELGs—many of which appear to be undergoing interactions themselves—are objects in which to study active star formation. Taken together, these two subsets of objects form a sample that allows us to gain a glimpse inside the process of galaxy assembly.

5.1. Tadpole Galaxies as Tracers of Galaxy Assembly

In Chapter 2 of this dissertation we present a sample of "tadpole" galaxies detected from the Hubble Ultra Deep Field. This study was motivated by the fact that the HUDF—the deepest imaging to date—has a strikingly large number of asymmetric, elongated objects with a knot–plus–tail morphology. Due to the generally low surface brightness of the tadpoles' tails, a field of the extraordinary depth of the HUDF was required to see these objects in abundance. We developed an algorithm to systematically select these galaxies from the HUDF F775W (i') band image to i'_AB=28.0 mag. The detection involved selection of sources by SExtractor (Bertin & Arnouts 1996) with two different deblending levels. Thus, two catalogs were created: one with highly-deblended tadpole knots, and one with low-deblended tadpole tails. Elongation cuts were made to ensure the desired morphology was selected. The two source lists were then spatially matched, with a offset angle imposed such that the knots were within 20° of the semi-major axis of the tails. The knots were also required to be at least $0.1a$ from the tail center to prevent inclusion of normal edge-on spirals

with a nuclear bulge. The list was visually checked and slightly refined as described in Chapter 1.

The percentage of galaxies that are tadpoles is shown to be roughly constant at around ∼6% at redshifts probed in the study (i.e. 0.1 to 4.5). If the tadpoles are indeed tracers of an early phase of galaxy merging events, this result suggests that the process of galaxy assembly in general keeps in step with existing field galaxies as a function of comic epoch. A partner study investigated variable objects in the HUDF (Cohen et al. 2006). Since merging activity is known to be associated with black hole growth, we expected to see some overlap in the two samples. However, we find that none of the HUDF tadpole galaxies show detectable signs of AGN activity. During the course of this study, new numerical simulations emerged (Springel et al. 2005, DiMatteo et al. 2005) that predicted that AGN activity (detectable by variations in brightness) would only be seen well *after* the merger appeared in a morphologically disturbed state. The fact that we do not see variations in brightness in our sample, combined with the tadpole morphology, supports the idea that these tadpole galaxies are early–stage major merger events, i.e., at a stage that likely precedes the "turn-on" of any AGN component and the onset of point–source variability. Thus, there is evidence that we are seeing two distinct phases—the early-stage merger or tadpole phase, and the AGN phase—in the overall process of galaxy evolution.

5.2. Detection of HUDF Emission-Line Galaxies and First Results

We detail several methods aimed specifically at detecting ELGs in HST ACS grism data in Chapter 3, and present a catalog of ELG properties. The data utilized

in this study was from the PEARS survey, and this particular investigation focused on data from the HUDF. In particular, we compare three different methods for detecting ELGs: two which rely on a two-dimensional detection technique in the original grism image and one that detects lines in one-dimensional extracted spectra. We find that the 2D method that utilizes traces in the grism image to determine the direct–image emitting source results in the most detections of real lines while reducing the amount of spurious detections significantly. This method is unique in that it allows detection of individual emitting regions within galaxies, allowing an investigation of star-forming regions in galaxies up to z$\sim$1.5.

A catalog of emission-line sources is presented, including coordinates, i'_{AB} magnitudes, line fluxes and identification, equivalent widths, and grism redshifts. The catalog contains information for 81 galaxy knots in 63 HUDF PEARS galaxies (a total of 96 emission lines). The most common lines—[O III] Hα and [O II]–account for 44%, 34MgII, C III], and C IVemitters comprising the remainder). 39 of these galaxies have new grism–spectroscopic redshifts as a result of our study.

We find in our PEARS HUDF grism data a potential upward trend of [O II] equivalent width with redshift. Particularly striking are the $EW_{[OII]} > 100$: these values are extremely rare in the local universe. Since [O II] EW is a tracer of galaxies' star–formation properties, trends such as this suggest strong evolution in these galaxies' star–forming properties over cosmic time. Many of the HUDF ELGs appear to be knotty spirals as well as clumpy interacting systems. These types—especially spirals with strong continuum emission—are often missed with the more traditional 1D se-

lection techniques because emission lines tend to be washed out by the continuum. In total, ∼20% of the PEARS HUDF galaxies have emphmultiple emitting knots, and display differences in flux values of up to ∼3.5 times. While variations in SFRs across galaxies has been known to exist for many years (Kennicutt et al. 1989; Zaritsky et al. 1994), this particular detection method allows us to study these star–forming knots in galaxies up to redshifts z∼1.5. We find very high emission–line luminosities in the PEARS HUDF Hα annd [O II]emitters (at average redshifts of 0.26 & 1.05 respectively) as compared to samples of local star–forming HII regions. Although the grism properties do prevent us from detecting the lower–luminosity emitters, sources with such high line luminosities and EWs are much less common in the local universe. These results are supportive of strong evolution in galaxies' star forming properties over cosmic time.

5.3. Emission-Line Galaxies in the PEARS South Fields

Chapter 4 extends the PEARS HUDF study to four additional fields in the PEARS dataset. We utilize the most efficient and robust detection method arrived at in Chapter 3, and present results based on ELGs detected in the five total PEARS South Fields (including the HUDF). Our catalog for PEARS South contains 230 emitting knots from 203 individual galaxies; 61 knots have more than one line (for a total of 320 emission lines). 26 galaxies (13%) have multiple emitting knots. 17 of the galaxies are CDF–S X–ray sources. As was the case for the HUDF–only sample, the [O III] emitters have very high equivalent widths (average $EW_{[OIII]} = 152\mathring{A}$).

We present a table of 118 new grism–spectroscopic redshifts for the CDF-S

field. 11 of these previously had no recorded redshift; these galaxies all had two lines such that direct line identification was accomplished via the wavelength ratio, yielding an accurate redshift. The large majority of our emitting knots (96%) have luminosities L$\gtrsim 10^{39}$ ergs s^{-1}, which have been classified as "giant" or "supergiant" by Kennicutt et al. (1989). From these luminosities we calculate lower limits to the star–formation rates (SFRs) of the galaxy knots, and find that the SFR as a function of redshift in general agrees with previous similar studies.

In this work we adjusted our line–fitting procedure to inlcude fits to Hβ which is blended with the [O III] doublet at the grism resolution. This resulted in 90 improved [O III] fluxes and 30 Hβ fluxes with $S/N > 3$. We detect the signature of downsizing in the ELGs, as fainter galaxies are forming more stars per unit luminosity/mass. As discussed in detail in Chapter 3, our 2D detection method allows detection of individual galaxy knots, and we find that the greatest variation in SFR across a single galaxy with multiple emitting knots occurs in galaxies with merger signatures such as pronounced asymmetries or tidal tails. The radial distribution of galaxy knots (for sources with multiple emitting knots) peaks near the normalized half–light radii.

5.4. Future Pursuits

The HUDF tadpole galaxies provide a unique set of merging galaxies in a distinct evolutionary phase, and further study has the potential to provide exciting new results. In particular, data in the $BVi'z'(JHK)$ filters is available for the HUDF, and we plan to compute star formation rates, stellar masses, and ages of the tadpole galax-

ies using the stellar population synthesis models of Bruzual & Charlot (2003). The fact that many of the tadpole galaxies have distinct color variations (i.e. blue knots with redder tails) suggests that composite stellar populations may be discernible—another result expected from merging activity (Corbin et al. 2006). Along these lines, we will deduce the star formation rates of the brightest tadpoles' separate populations using the integrated flux and assuming both an old underlying population and recent star formation, using the methods of Cid Fernandes et al. (2004). If these galaxies are indeed comprised of composite old and young stellar populations, using this method will allow a more thorough investigation of these galaxies' complex star formation properties. In addition to star formation rates, ages and stellar masses of the tadpoles will also be calculated, similar to Papovich, Dickinson, & Ferguson (2001). Existing ground-based VLT JHK data in the CDF-S will be utilized as well as PEARS data for these objects.

Many studies have indicated that an evolutionary sequence between mergers, ULIRGs, and AGNs exist (Sanders et al. 1988; Veilleux 2006) and that there is an observable relation between the evolution of galaxies and their black holes (Heckman & Kauffman 2006). As discussed in Chapter 2, our results suggest that the early–stage merger and AGN phases are morphologically distinct; this was also predicted by numerical simulations. Although the details are difficult to interpret, it is widely accepted that merging activity appears to be a key process in building up "red and dead" ellipticals. Studies of nearby ULIRGs have even indicated that multiple simultaneous mergers occur and their remnants can be seen clearly (Borne et al. 2000). We

will conduct a study of each of these separate classifications of objects in the HUDF (and larger deep fields where necessary), using the stellar population synthesis models to derive SFRs, masses, and ages of a large sample of objects in order to investigate their relationship in a statistical manner. This will be carried out using existing HST $BVi'z'$ data as well as VLT JHK data in the CDF-S. Additionally, galaxy sizes scale with redshift in a systematic way (Ferguson et al. 2004, Bouwens et al. 2004). A study of the size evolution of each class of objects mentioned here will yield insight into the overall scheme of the evolutionary sequence.

Much of this dissertation is focused on optimizing detection techniques for objects of interest in HST ACS grism data—here, specifically, emission–line galaxies. We have obtained a sample of ELGs in one of the most widely–studied areas of the sky—the CDF–S field. With our sample, several future science endeavors are planned. First, we will use the detection techniques described in Chapter 3 to select and characterize ELGs in terms of wavelength, flux, equivalent width, line identificaiton, and redshift in the remaining four PEARS North fields. This will effectively double our sample, allowing better statistics that are needed for detailed projects outlined here. With this larger dataset, our sample should be large enough to begin drawing more firm conclusions concerning the changes in [O II] EW with redshift and downsizing hinted at here. Once the entire sample is available (as well as results from simulations, which are being performed presently and will help to sort out various selection effects), we will extend this study to luminosity functions, pushing to higher redshifts and fainter continuum magnitudes than in previous studies. This will allow

comparison to the line luminosity functions seen locally, and we will draw conclusions concerning evolution of HII regions if prominent trends exist. The full set of extremely bright [O II] emitters will be an interesting population to probe in itself. In addition to [O II] the Hα and [O III] line luminosity functions will also be derived and compared to local samples.

As line emission is a probe to star formation properties in galaxies, a study of the SFRs in these galaxies is a natural course to pursue. Star formation rates measured over cosmic time provide a wealth of insight into understanding the overall picture of galaxy assembly. We will use the complete sample of ELGs obtained from all the PEARS fields and further investigate the occurrence of extremely high equivalent width [O II] emitters at high redshift detected in the HUDF data. Madau et al. (1998) have shown that an increase in SFR occurs over the same redshift range probed by the [O II] emitters in this study. We will investigate this EW trend as it relates to the SFR increase and the rise in merger activity over the same redshift. In addition to using the [O II] EWs as a proxy for SFR, we will compute specific–SFRs of the galaxies by obtaining masses for our sample using SED fits as described for the tadpole galaxies. Higher fractions of high-equivalent width objects at redshifts z>1 have been noted previously (Teplitz et al. 2003, Meurer et al. 2007, Cowie et al. 1999), and this sample should serve to extend the study to star formation trends in intrinsically fainter galaxies.

One lesson learned from our 2D detection method was that individual HII regions can be distinguished and spectra of these regions can be obtained in galaxies

out to z$\sim$0.2–0.4. Of the galaxies with multiple emitting knots, there are several cases where the line fluxes and equivalent widths vary by factors of 4 or more in separate knots within one galaxy. This is a strong indication that the star formation properties of these objects differ across the galaxy itself, and that this phenomenon in general can be probed at redshifts z>0.2–0.4. Given the complete sample, we will perform a detailed analysis of these galaxies with multiple emitting knots, thus extending studies of line–emitting HII regions into the intermediate redshift universe.

REFERENCES

Alexander, D.M. et al. 2003, AJ 126, 539

Baade, W. & Minkowski, R. 1954, ApJ, 119, 206

Baldwin, J., Phillips, M., & Terlevich, R. 1981, PASP, 93, 5

Bolzonella, M., Miralles, J., Pello, R. 2000, A&A, 363, 476

Barger, A.J. et al. 2003 ApJL, 584, L61

Beckwith, S., et al. 2005, AJ, in preparation

Bender, R. 1996, New Light on Galaxy Evolution (Dordreccht, Kluwer)

Blitz, L. et al. 1981, ApJ, 249, 76

Blumenthal, G., Faber, S., Flores, R., Primack, J. 1986, ApJ 301, 27

Borne, K.D. et al. 2000, ApJL, 529, L77

Bournaud, F., Jog, C.J., & Combes, F. 2007, A&A, 476, 1179

Bouwens, R. et al. 2004, ApJ, 611, L1

Brinchmann, J. et al. 2004, MNRAS, 351, 1151

Calzetti, D., Kinney, A., & Storchi-Bergmann, T. 1994, ApJ 429, 582

Capak, P. et al. 2007, astro-ph/07042430v1

Cardelli, J.A., Clayton, G.C., & Mathis, J.S. 1989, ApJ, 345, 245

Castaneda, H.O, Vilchez, J.M., & Copetti, M.V.F. 1992, A&A, 260, 370

Cid Fernandes, R. et al. 2004, MNRAS, 355, 273

Cohen, S. et al. 2006, ApJ, 639, 731

—— 2008, in preparation

Coe, D., Benitez, N., Sanchez, S.F., Jee, M., Bouwens, R., Holland, F. 2006, AJ 132, 926

Conselice, Bershady & Jangren 2000, ApJ 529, 886

Conselice, C. et al. 2003, AJ 126, 1183

Conselice, C. et al 2004, ApJL 600, L139

Cowie, L, Songaila, A., & Barger, A. 1999, AJ 118, 603

Cowie, L., Songaila, A., Hu, E., & Cohen, J.G. 1996, AJ 112, 839

Cowie, L., Hu, E., & Songaila, A. 1995, AJ 110, 1576

Davis, M. et al. 2003, Proceedings of the SPIE, 4834, 161

Davoodi, P., et al. 2006, MNRAS, 731, 1113

di Matteo, P., combes, F., Melchior, A.-L., & Semelin, B. 2007, A&A, 468, 61

Di Matteo, T., Springel, V., & Hernquist, L. 2005, Nature, 433, 604

Driver, S., Windhorst, R., Griffiths, R. 1998 ApJ 453, 48

Drozdovsky, I. et al. 2005, AJ 130, 1324

Elmegreen, D., Elmegreen, B., & Hirst, A. 2004, ApJL 604, L21

Elmegreen, D., Elmegreen, B., & Sheets, C. 2004, ApJ 603, 74

Elmegreen, D., Elmegreen, B., Rubin, D., Schaffer, M. 2005, ApJ 631, 85

Elmegreen, D.M., et al. 2006, ApJ, 642, 158

Ferguson, H. et al. 2004, ApJL, 600, L107

Fryer, C.L., Woosely, S.E., & Heger, A. 2001, ApJ, 550, 382

Gallego, J., Zamorano, J., Aragon-Salamanca, A., & Rego,M. 1995, ApJ 455, L1

Gallego, J., Garcia-Dabo, C.E., Zamorano, J., Aragon-Salamanca, A., & Rego, M. 2002, ApJ, 570, L1

Gardner, J.P. et al. 1998, ApJ, 492, L99

Giacconi, R. et al. 2002, ApJS, 139, 369

Giavalisco, M., Ferguson, H. C., Koekemoer, A. M., *et al.* 2004, ApJ, 600, L93

Glazebrook, K. et al. 2004, Nature, 430, 181

Gordon, K.D., et al. 2004, ApJS, 154, 215

Grazian, A. et al. 2004, AJ 127, 592

Grogin, N. et al. 2005, ApJL 627, 97

Hathi, N.P. et al. 2008, in press

Hammer, F. et al. 1997, ApJ 481, 49

Heckman, T. & Kauffmann, G. 2006, NewAR, 50, 677

Helmboldt, J.F. et al. 2004, ApJ, 613, 914

Hernquist, L. & Mihos, J.C. 1995, ApJ, 448, 41

Hibbard, J.E. et al. 2005, ApJL, 619L

Hodge, P.W. 1969, ApJ, 155, 417

Holmberg, E. 1941, ApJ, 94, 385

Hopkins, P., Hernquist, L., Cox, T., & Dusan, K. 2008, ApJS, 175, 365

Hopkins, P., Hernquist, L., Cox, T., Di Matteo, T., Robertson, B., & Springel, V. 2006, ApJS, 163, 1

Hopkins, P., Hernquist, L., Martini, P., Cox, T., Robertson, B., Di Matteo, T., Springel, V. 2005, ApJL, 625, L71

Jansen, R.A., Fabricant, D., Franx, M., & Caldwell, N. 2000, ApJS 126, 331

Jansen, R.A., Franx, M., & Fabricant, D. 2001, ApJ, 551, 825

Jordan, A., Cote, P., West, M., Marzke, R., Minniti, D., & Rejkuba, M. 2004, AJ, 127, 24

Kauffmann, G. et al. 2003, MNRAS 346, 1055

Keel, W.C. 1991, "Dynamics of Galaxies and their Molecular Cloud Distributions", eds. F. Combes and F. Casoli (Dordrecht: Kluwer), p. 243

Kennicutt, R.C.,Jr. 1983, ApJ 272, 54

—— 1992, ApJ, 388, 310

—— 1998, ARA&A 36, 189

Kennicutt, R.C.,Jr., Bresolin, F., French, H., & Martin, P. 2000, ApJ, 537, 589

Kennicutt, R.C.,Jr., Edgar, B.K., & Hodge, P.W. 1989, ApJ 337, 761

Kennicutt, R.C.,Jr., Keel, W. C., van der Hulst, J. M., Hummel, E., Roettiger, K. A., 1987, AJ, 93, 1011

Kewley, L.J., Geller, M.J., & Jansen, R.A. 2004, AJ, 127, 2002

Kewley, L.J., Dopita,M., Sutherland, R., Heisler, C., Trevena, J. 2001, ApJ, 556, 121

Kinney, A.L. et al. 1993, ApJS, 86, 5

Kirby, E.N., Guharthakurta, P., Faber, S.M., Koo, D.C., Weiner, B.J., & Cooper, M.C. 2007, ApJ 660, 62

Koekemoer, A. 2004, "The Hubble Ultra Deep Field ACS/WFC Combined Images–V1.0" http://cadcwww.dao.nrc.ca/udf/acs-wfc/h_udf_wfc_Readme.txt

Knierman, K. et al. 2003, AJ, 126, 1227

Koo, D.C., "Highlights of Astronomy", 1998, Proceedings of IAU Joint Discussion II, Vol. 11A

Koo, D.C., 2003, proceedings of "Galaxy Evolution: Theory and Observations",Cozumel, Quintana Ruo, Mexico, Vol. 17, 245

Lanzetta, K.M. et al. 1997, Proceedings of the STScI 1997 May Symposium (astro-ph/9709166)

Kurk et al. 2004, A&A, 442, L13

Larson, R.B. & Tinsley, B.M. 1978, ApJ 219, 46

Leir, A. & van den Bergh, S. 1982, ApJS, 34, 381

Li, C. et al. 2008, MNRAS, 385,1903

Lilly, S.J., Hammer, F., le Fevre, O., Crampton, D. 1995, ApJ 455, 75

Lilly, S.J., et al. 2007, astro-ph/0612291

Madau,P., Pozzetti, L., & Dickinson, M. 1998, ApJ 498, 106

Malhotra, S. et al. 2005, ApJ 626, 666

Malhotra, S. et al. 2008, in preparation

Martini, P. 2004, Carnegie Obs. Astrophys. Ser. 1, Coevolution of Black Holes and Galaxies (Cambridge: Cambridge University Press), 170

Matthews, T., Morgan, W., & Schmidt, M. 1964, ApJ, 140, 35

Meaburn, J., Terrett, D.L. 1982, MNRAS, 200, 1

McCall, M.L, Rybski, P.M., & Shields, G.A. 1985, ApJS, 57, 1

McCarthy, P.J., et al. 1999, ApJ, 520, 548

Mihos, J.C. & Hernquist, L. 1994, ApJL, 425, L13

—— 1996, ApJ, 464, 641

Mihos, J.C., Richstone, D., & Bothun, G. 1992, ApJ 400, 153

Meurer, G.R., et al. 2007, AJ 134, 77

—— 2006, ApJS, 165, 307

Mobasher, B. et al. 2004, ApJL 600, 167

Navarro, J., Frenk, C., White, S. 1997, ApJ 490, 493

Odewahn, S. et al. 1996, ApJL 472, L13

Odewahn, S. et al. 2002, ApJ 568, 539

Okamoto, T. & Nagashima, M. 2004, Proceedings of IAU Colloquium, 195

Papovich, C., Dickinson, M, & Ferguson, H. 2001, ApJ 559, 620

Pirzkal, N. et al. 2004, ApJS 154, 501

—— 2006, ApJ 636, 582

Rhoads et al. 2005, ApJ 621, 582

Robertson, B. et al. 2005, ApJL, submitted (astro-ph/0503369)

Rosa, M., Joubert, M., Benvenuti, P. 1984, A&AS, 57, 361

Ryan, R.E. et al. 2007 ApJ 668, 839

Salzer, J.J. et al. 2000, AJ 120, 80

—— 2001, AJ 121, 66

—— 2002, AJ 123, 1292

Sanders, D.B. et al. 1988, ApJ, 325, 74

Scoville, N., Abraham, R. G., Aussel, H., *et al.* 2007, ApJS, 172, 150

Seaton, M.J. 1979, MNRAS, 187, 73P

Shields, G.A. 1974, ApJ, 193, 335

Shields, G.A. 1990, ARA&A, 28, 525

Shim, H. et al. 2007, BAAS, 211, 5209

Smith, B.J., Struck, C., & Pogge, R.W. 1997, ApJ, 483

Springel, V., di Matteo, T., & Hernquist, L. 2005a, ApJ, 620, 79

Springel, V., di Matteo, T., Hernquist, L. 2005b, MNRAS 361, 776

Straughn, A.N., Cohen, S.H., Ryan, R.E., Hathi, N.P., Windhorst, R.A., & Jansen, R.A. 2006, ApJ 639, 724

Straughn, A.N. et al. 2006, BAAS 20917104

—— 2008, AJ, 135, 1624

Struck, C. 1999, Physics Reports, 321, 1

Takahaski, M.I. et al. 2007, ApJS 172, 456

Teplitz, H.I., Collins, N.R., Gardner, J.P., Hill, R.S., Rhodes, J. 2003, ApJ 589, 704

Thompson, R.I., Eisenstein, D., Fan, X., Dickinson, M., Illingworth, G., Kennicutt, R. C., Jr. 2006, ApJ, 647, 787

Tonry, J.L. 1987, Proceedings of the IAU Symposium, 89, 1987

Toomre, A. & Toomre, J. 1972, ApJ, 178, 623

Treu, T., Ellis, R.S., Liao, T.X., van Dokkum, P.G., 2005, ApJL 622L, 5

van den Bergh, S., 2002, PASP 114, 797

White, S.D.M. & Rees, M.J. 1978, MNRAS 183, 341

Veilleux, S. 2006, NewAR, 50, 701

Williams, R. et al. 1996, AJ 112, 1335

Willmer, C.N.A. et al. 2006, ApJ 647, 853

Windhorst, R.A. et al. 1994, AJ 107, 930

—— 2002, ApJS 143, 113

Xu, C. et al. 2007, AJ 134, 169

Yan, H., & Windhorst, R. 2004, ApJL 600, L01

Yan, H., & Windhorst, R. 2004, ApJL 612, L93

Zaritsky, D., Kennicutt, R.C., Huchra, J.P. 1994, ApJ 420, 87